

# **New Semi-active Vibration Control with Serial-Stiffness-Switch-System based on Vibration Energy Harvesting**

Dissertation

zur Erlangung des akademischen Grades

**Doktoringenieur  
(Dr.-Ing.)**

vorgelegt der

Fakultät für Maschinenbau der  
Technischen Universität Ilmenau

von Herrn

**M. Sc. Chaoqing Min**

geboren am 15.08.1986 in Shandong, China

1. Gutachter: Prof. Dr.-Ing. Thomas Sattel
2. Gutachter: Prof. Dr. Dr. h.c. Peter Hagedorn
3. Gutachter: Prof. Dr.-Ing. habil. Alexander Fidlin

Tag der Einreichung: 19.06.2018

Tag des öffentlichen Teils der wissenschaftlichen Aussprache: 28.08.2018



---

# Abstract

---

This dissertation investigates a novel semi-active vibration control with Serial-Stiffness-Switch-System (4S) based on vibration energy harvesting.

On the basis of the vibration reduction performance analysis for a passive and a semi-active switching system, the problem in the present vibration control systems is stated and 4S concept is consequently put forward. In order to examine its performance, 4S in open loop control is analyzed firstly and the equivalent stiffness and natural frequency of the switching system are derived. Following is the analysis for 4S in closed loop control. A velocity zero-crossing switching law based on vibration energy harvesting is used for vibration reduction. This is numerically validated under a harmonic disturbance. Afterwards, vibration energy harvesting limit is analyzed.

An experimental validation on this novel vibration control strategy is then presented and a rotational test rig is developed. The test rig uses two ring-arranged electromagnet-plates together with an armature-shaft as two mechanical switches to achieve the connection or disconnection of two spiral springs to or from a primary plate. The vibration energy harvesting and vibration reduction performance of 4S are tested on this experimental system.

Apart from a harmonic disturbance, a nonzero initial velocity vibration is also considered. To improve vibration reduction performance in this case, a new switching law is proposed. By means of phase plane, the transient and steady chattering response of 4S are analyzed. The switching law enables a fast transformation of initial vibration energy into potential energy equally stored in two springs. This is numerically and experimentally validated. Additionally, a harmonic disturbance is also exerted on the new switching law. The results show that 4S has a better positioning performance than that for the velocity zero-crossing switching law.

Finally, 4S is further applied for shock isolation. The maximum displacement response reduction during shock and the residual vibration suppression after shock are numerically validated. Moreover, the effect of several design parameters of 4S on the shock isolation performance is investigated as well.



---

# Kurzfassung

---

Diese Dissertation untersucht eine neuartige semi-aktive Schwingungsteuerung mit einem seriellen-Steifigkeit-Schalter-System (4S) basierend auf der Speicherung von Schwingungsenergie.

Auf Basis der Schwingungsreduktionsanalyse für ein passives und ein semi-aktives Schaltsystem werden Probleme vorhandener Schwingungsteuerungssystemen aufgezeigt und durch das 4S Konzept gelöst. Um seine Leistungsfähigkeit zu untersuchen, wird zunächst 4S im offenen Regelkreis analysiert und die äquivalente Steifigkeit und Eigenfrequenz des Schaltsystems abgeleitet. Es folgt die Analyse für 4S im geschlossenen Regelkreis. Zur Schwingungsreduzierung wird ein Geschwindigkeits-Nulldurchgangs Schaltgesetz verwendet, das auf der Gewinnung von Schwingungsenergie basiert. Dies wird unter einer harmonischen Störung numerisch validiert. Anschließend werden Grenzen der Energiespeicherung analysiert.

Es folgt eine experimentelle Validierung dieser neuartigen Strategie zur Schwingungsteuerung vorgestellt und ein drehender Prüfstand entwickelt. Der Prüfstand verwendet zwei ringförmig angeordnete Elektromagnetplatten zusammen mit einer Ankerwelle als zwei mechanische Schalter, um die Verbindung oder Trennung von zwei Spiralfedern mit einem Lastträgheitsmoment zu erreichen. Die Speicherung von Schwingungsenergie und die Schwingungsreduktion werden auf diesem Versuchssystem getestet.

Neben einer harmonischen Störung wird auch eine Anfangsgeschwindigkeit ungleich Null berücksichtigt. Um in diesem Fall die Schwingungsreduktion zu verbessern, wird ein neues Schaltgesetz vorgeschlagen. Mit Hilfe der Phasenebene wird das transiente und stationär Ratterverhalten von 4S analysiert. Das Schaltgesetz ermöglicht eine schnelle Umwandlung der anfänglichen kinetischen Energie, die in beiden Federn zu gleichen Teilen gespeichert wird. Dies ist numerisch und experimentell validiert. Zusätzlich wird einer harmonischen Störung an dem neuen Schaltgesetz getestet, das ein besseres Positionierverhalten als das Geschwindigkeits-Nulldurchgangs Schaltgesetz aufweist.

Schließlich wird 4S zur Schockisolierung eingesetzt. Die maximale Reduzierung des Überschwingens des Wegs beim Schock und die Reduktion der Restschwingungen nach dem Schock werden numerisch validiert. Darüber hinaus wird auch der Einfluss verschiedener Designparameter von 4S auf das Isolationsverhalten untersucht.

---

## Acknowledgment

---

I would like to acknowledge with a deep appreciation for the academic guidance and the continuous encouragement provided by my supervisor, Professor Thomas Sattel. His patience and inspirational guidance were extremely valuable in the successful completion of this work. His help is far beyond what a normal supervisor could provide, not only limited to academic aspects but also cherish experience in life.

I would also like to sincerely thank Dr.-Ing. Martin Dahlman. He also gives me a lot of advice on this project. It is kind of him to provide this guidance. My thanks also go to Dr.-Ing. Ralf Keilig, who has excellent experience in practice and gives me a lot of help with the manufacture of the test rig.

I want to give my thanks to assistant Professor Tom Ströla, who is very kind and also gives me some suggestions for my thesis. Meanwhile, he also encourages me to work frequently. I am also grateful to my colleagues Dr.-Ing. Oliver Radler, M. Sc. Martin Silge, M. Sc. Aditya Suryadi Tan, M. Sc. Christoph Greiner-Petter, B. E.(Hons) Kanu Ross, Dipl.-Ing. Dennis Roeser, Dipl.-Ing. Maria Gadyuchko, Dipl.-Ing. Olga Roeser, Dipl.-Ing. Anton Kochnev. They help me a lot when I worked in the institute at beginning, not only on academic but also in everyday life. I would also like to thank our technician Mrs Cornelia Hecht, Mr Heiko Rödiger, and our secretary Mrs Annette Volk. They have provided a lot of help with my German language and everyday life.

Finally, I would like to sincerely thank my wife, Yulei Zhao. She has taken care of our child during my PhD studies and supported me a lot. I also show my thanks to our parents for their understanding and support of my pursuit of a PhD degree in a foreign country. I am grateful to my old brother for his encouragement and guidance in my PhD studies as well.





---

# Contents

---

<b>Acknowledgment</b>	<b>vii</b>
<b>1. Introduction</b>	<b>1</b>
1.1. State of the Art . . . . .	1
1.1.1. Vibration Control . . . . .	1
1.1.2. Variable Stiffness Systems for Vibration Control . . . . .	6
1.2. Summary of Literature Review . . . . .	17
1.3. Objective . . . . .	17
1.4. Contribution . . . . .	18
1.5. Thesis Organization . . . . .	19
<b>2. Novel Semi-active Vibration Control with 4S</b>	<b>21</b>
2.1. Introduction . . . . .	21
2.2. 4S Concept . . . . .	22
2.2.1. Problem Statement . . . . .	22
2.2.2. Vibration Energy Harvesting Concept . . . . .	24
2.2.3. 4S Model . . . . .	25
2.3. Open Loop Control for 4S . . . . .	27
2.3.1. Numerical Analysis . . . . .	27
2.3.2. Analytical Formulation . . . . .	30
2.4. Closed Loop Control for 4S . . . . .	32
2.4.1. Switching Law based on Vibration Energy Harvesting . . . . .	32
2.4.2. System Dynamics . . . . .	34
2.4.3. Numerical Analysis . . . . .	35
<b>3. Vibration Energy Harvesting Limit Analysis</b>	<b>41</b>
3.1. Introduction . . . . .	41
3.2. Spectrum Analysis for System Response . . . . .	41
3.3. Steady State System Response . . . . .	44
3.4. Necessary Conditions for Vibration Energy Harvesting Limit . . . . .	48

3.5.	Numerical Analysis for Vibration Energy Harvesting Limit . . . . .	50
3.5.1.	Nonzero Initial Conditions . . . . .	50
3.5.2.	Zero Initial Conditions . . . . .	51
3.5.3.	Extended Time Numerical Simulation . . . . .	52
<b>4.</b>	<b>Experimental Validation</b>	<b>55</b>
4.1.	Introduction . . . . .	55
4.2.	Operation Principle and Modeling of Setup . . . . .	56
4.2.1.	Operation Principle . . . . .	56
4.2.2.	Modeling . . . . .	57
4.3.	Setup Construction . . . . .	60
4.3.1.	Mechanical Structure . . . . .	60
4.3.2.	Power Electronics . . . . .	65
4.3.3.	Lumped System . . . . .	68
4.4.	Experiment . . . . .	68
4.4.1.	System Parameter Identification . . . . .	69
4.4.2.	Step Response . . . . .	73
4.4.3.	Harmonic Response . . . . .	75
<b>5.</b>	<b>Improved Switching Law for 4S</b>	<b>81</b>
5.1.	Introduction . . . . .	81
5.2.	Nonzero Initial Velocity Problem for 4S . . . . .	81
5.3.	Variable Structure System Control for 4S . . . . .	83
5.3.1.	State Trajectory Analysis . . . . .	83
5.3.2.	New Switching Surface . . . . .	86
5.4.	Experimental Verification . . . . .	90
5.4.1.	Nonzero Initial Velocity Condition . . . . .	90
5.4.2.	Harmonic Excitation . . . . .	93
5.4.3.	PID Feedback Controlled Switching Law . . . . .	93
<b>6.</b>	<b>Shock Isolation with 4S</b>	<b>97</b>
6.1.	Introduction . . . . .	97
6.2.	Harmonic disturbance isolation using 4S . . . . .	97
6.2.1.	Modeling . . . . .	97
6.2.2.	Numerical Analysis . . . . .	98
6.3.	Shock isolation for 4S . . . . .	99
6.3.1.	Shock isolation systems . . . . .	100
6.3.2.	Shock isolation using 4S without potential energy pre-storage . . . . .	101
6.3.3.	Shock isolation using 4S with potential energy pre-storage . . . . .	104
6.4.	Shock isolation performance analysis of 4S . . . . .	106
6.4.1.	Time domain analysis . . . . .	106
6.4.2.	Multi-dimension parameters performance analysis of 4S . . . . .	108
<b>7.</b>	<b>Summary and Future Work</b>	<b>111</b>
7.1.	Summary . . . . .	111
7.2.	Future Work . . . . .	112
	<b>Bibliography</b>	<b>113</b>

---

<b>A. Vibration Energy Limit Analysis</b>	<b>123</b>
A.1. Solution for Integration Coefficients . . . . .	123
<b>B. Setup Construction</b>	<b>125</b>
B.1. Diameter and Thickness of Armature . . . . .	125
B.2. Switching Current Measurement of Mechanical Switch . . . . .	127
<b>C. Sliding Mode Control</b>	<b>129</b>
C.1. Theory Basis . . . . .	129



## Introduction

---

### 1.1. State of the Art

#### 1.1.1. Vibration Control

Vibration, which generally performs oscillation around a balance position, is a common motion phenomenon occurring in nature and human lives. Sometimes high levels of vibration can be beneficial and desirable, from small equipment such as a loudspeaker to large machines such as tamping machines, vibrating conveyors, and sieves. But mostly, vibration is unwanted due to creating uncomfortable noise, wasting energy, causing mechanical wear, structural fatigue, and resulting in an increased danger. Therefore, vibration control has been extensively studied by researchers. Vibration control is understood here as vibration reduction to decrease unwanted oscillations in a protected structure. Generally, this is achieved by a compact connection element consisting of a spring, a damper or together with a mass. A fundamental introduction to vibration control is documented in [1], p. 479.

#### Vibration Control Object

Different mechanical structure configurations among a vibration source, a protected payload, a vibration control element, and vibration transmission path, result in three types of vibration control, namely, vibration isolation, vibration suppression, and vibration absorption see [2] p. 5.

Vibration isolation happens when a vibration control element, namely an isolator, is designed for the connection between a vibration source and a protected structure in order to isolate the vibration source from the system of interest. This is further

categorized as source isolation and receiver isolation. The former refers to a vibration source and surrounding environment such as ground and force transmissibility is taken into consideration as depicted in Fig. 1.1(a). The external force  $F$  acting on mass  $m$  denotes a vibration source. The spring  $k$ , and damping  $d$  make up a vibration isolator. The force transmissibility  $F_c/F$  is to assess the source isolation performance. The latter is related to a base excitation denoted by  $x_0$ ,  $\dot{x}_0$ , and a sensitive structure  $m$  as shown in Fig. 1.1(b). Vibration isolation performance is characterized by the motion transmissibility  $x/x_0$  or  $\dot{x}/\dot{x}_0$ . The transmissibility property is strongly decided by the frequency ratio of the external disturbance frequency  $\Omega$  to system natural frequency  $\omega_0$ ,  $\omega_0 = \sqrt{k/m}$ , and system damping ratio  $D = d/(2\sqrt{km})$ .

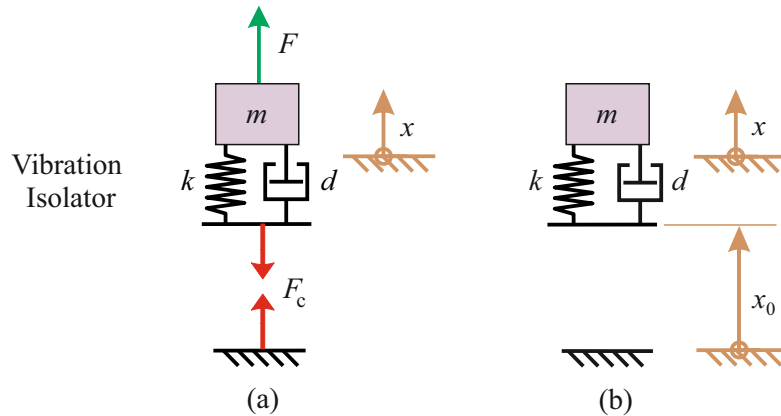


Figure 1.1.: The models for vibration isolation systems. (a) Source isolation; (b) Receiver isolation.

Vibration absorption is realized by a vibration absorber or a tuned vibration absorber, consisting of a reaction mass  $m_a$ , a spring  $k_a$  together with an appropriate damping  $d_a$ , graphically depicted in Fig. 1.2. A vibration absorber, framed by a dotted line, is hung on a protected payload  $m$ , whose operation frequency meets the resonant frequency of the vibration absorber. The corresponding theory, various design configurations and applications have been documented in [3, 4].

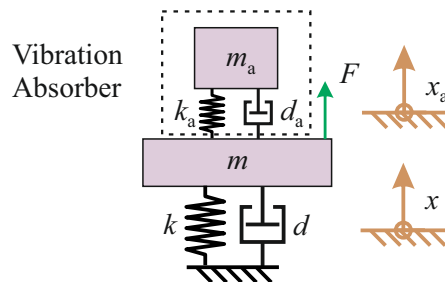


Figure 1.2.: The model for a vibration absorption system.

Vibration suppression is to remove an external disturbance directly acting on a protected payload. This usually occurs through state feedback control as graphically illustrated by 1.3. An actuator  $u$  acts on the protected payload  $m$  responding to

Feedback Control Unit. This results in that the protected payload  $m$  does not suffer from an external disturbance  $F$  and is able to stay around a demand position [2].

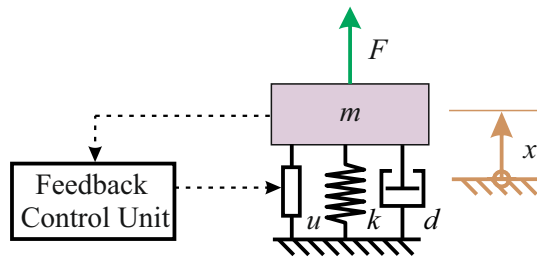


Figure 1.3.: The model for an active vibration suppression system.

## Vibration Control Method

Apart from the above classification of vibration reduction principles, following is another classification of vibration control, depending on whether or not external power or information is needed. Vibration control is mainly referred to four vibration control systems, i.e. passive, semi-active, active and hybrid systems, which have been studied in the past decades [5].

Passive control is the oldest vibration control method, receiving no external energy or information, the corresponding theory is well documented, see [6]. A passive system shows the advantages of simple structure, low cost, being stable and high reliability, but also proves to be disappointed due to not being able to adjust the structural parameters with the vibration change over time and optimize the design for varying excitation frequencies [7]. Generally, there exist linear and nonlinear passive systems. A linear passive system has a fixed system parameter such as fixed stiffness. A nonlinear passive systems has a variable stiffness, which can compensate disadvantage of a linear passive system to some way, see [8].

Active control uses a device, in other words, an actuator driven by external energy and control information to provide an additional vibration path to flexibly and quickly adapt the time-variation of an external disturbance for vibration reduction. This device is able to directly add or dissipate mechanical energy in an active control system. In particular, an input of equal amplitude and opposite phase is generated and combined with the primary vibration, thus resulting in the cancellation of both vibrations [9, 10]. According to Preumont [11], p. 6, semi-active devices cannot input energy directly in the system being controlled. This important prerequisite ensures that variations of the system parameter do not lead to parametric excitation. This is usually not considered properly in literature, when using the term semi-active. It has demonstrated greater performance than that of a passive control system and is used as one effective approach to suppress unwanted vibrations in different applications [12]. However, relatively high power, cost, complexity and instability of the system cast active vibration control into shade.

Since passive and active vibration control have their own advantages and disadvantages, both of them are combined into what is called hybrid vibration control. The hybrid

vibration control system can be used over a wide frequency range, reduces the needed external energy compared to a purely active system and still achieves some vibration reduction if the active control element fails. However, the risk of instability created by the active element and the degradation over time owing to detuning of the passive element still exist in system [13]. Apart from the hybrid control related to passive and active control, there also exist the ones consisting of passive and semi-active or active and semi-active control. For example, the hybrid control based on passive plus semi-active control is proposed in [14] in order to enlarge the working frequency range. Khan et al. [15] developed a hybrid combination of active and semi-active control for vibration suppression in order to enable a semi-active magneto-rheological damper to work as close to a fully active device as possible.

Semi-active vibration control uses a device with controllable properties to achieve variable system parameters such as stiffness and damping with a low external power supply. This kind of device does not provide an additional vibration path to directly react against an external disturbance for vibration reduction. So a semi-active vibration control device, differing from active control, will not directly increase or decrease the mechanical energy of the system and can be seen as a passive device with controllable properties [9, 10]. According to Preumont [11], p. 6, semi-active devices cannot input energy directly in the system being controlled. This important prerequisite ensures that variations of the system parameter do not lead to parametric excitation. This is usually not considered properly in literature, when using the term semi-active. Adjusting system parameters based on the measured state feedback signals enables a larger work frequency range and more flexibility obviously. What's more, if a control system fails, a semi-active control mode can still work in a passive case to some extent [16]. Different vibration control systems can be grouped as shown in Fig. 1.4.

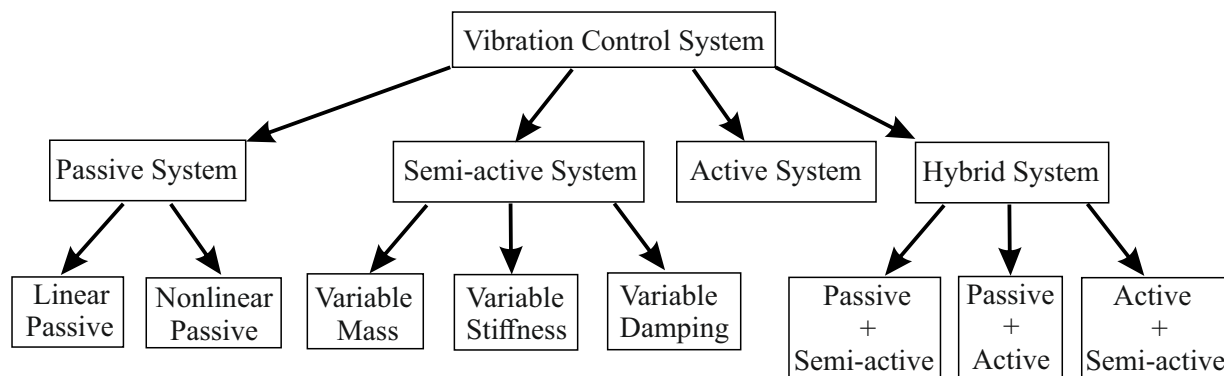


Figure 1.4.: Different vibration control systems.

## Variable Stiffness Systems

Through the literature reviewing, it is not difficult to find that the system stiffness plays an important role on vibration control. For instance, if the disturbance frequency is larger than the natural frequency of a vibration control system, vibration isolation works well. If not, an amplified vibration response is produced on a primary structure,



see [17]. In the case of shock isolation, a damping device can transmit large force to the primary structure because in traditional dampers high velocity corresponds with high reaction forces, but this will not occur in a stiffness device. Bobrow et al. [18] utilized a variable stiffness device in an automotive suspension system, where the force transmitted through a conventional damper is more than an order of magnitude higher than the force transmitted through the variable stiffness device. In overcoming the compromise between minimizing the shock transmission through an isolator and minimizing the static deflection, a variable stiffness system also performs well, see [19]. A tuned vibration absorber with variable stiffness allows vibration reduction against external disturbances with different frequencies and resting in a better primary structure response than a passive stiffness counterpart, see [20]. Compared with passive stiffness systems, variable stiffness systems, showing more flexibility in shifting the system frequency for vibration control, have attracted a lot of researchers.

In fact, variable stiffness systems exist in many engineering areas. For instance, in a microelectromechanical system (MEMS) they are used in a variety of applications such as radio-frequency mechanical filters, energy harvesters, atomic force microscopy, vibration detection sensors, and so on, see [21]. When designing micro-scale tactile probes, a design trade-off must be made between their stiffness and flexibility, which needs variable stiffness probing systems, see [22]. In robotics field, a variable stiffness actuator, consisting of motor, sensor and spring, is useful for the compliant, robust and dexterous control of different robots [23]. However, variable stiffness systems are limited to vibration reduction applications in this thesis. These systems have been widely studied in mechanical engineering [24], seismic and civil engineering [25, 26], aerospace and aviation [27, 28], vehicle systems [29–31], and so on. More information about variable stiffness design and application is documented by Winthrop [32].

Variable stiffness exists not only in a semi-active system as shown in Fig. 1.4, but also in a nonlinear passive and an active system. A semi-active variable stiffness system uses a device with controllable properties to achieve variable stiffness. Reversely, a nonlinear passive system is not controllable and uses a high static and low dynamic property of a nonlinear elastic element to achieve stiffness variation. In these systems, nonlinearity is not easy to model and analyze. Generally, an active system uses an actuator to directly drive a protected payload to react against an external disturbance, but in some cases the used actuator drives several elastic elements in a geometrical configuration, which support the protected payload, and their configuration geometry deformation results in a variable stiffness. This should be seen as an active variable stiffness, because the actuator adds mechanical energy to the system to some extent. However, this kind of stiffness variation has been also wrongly defined as semi-active variation stiffness [33]. To the authors knowledge through the literature reviewing, there does not exist an obvious classification for a semi-active and an active variable stiffness. Therefore, this thesis will not clearly distinguish whether a variable stiffness belongs to a semi-active or an active variable stiffness.

## 1.1.2. Variable Stiffness Systems for Vibration Control

### Modeling for Variable Stiffness Mechanism

System stiffness can be varied continuously or discretely. A variable stiffness vibration control system can be graphically simplified as in Fig. 1.5.  $F$  is taken as an external disturbance and  $m_1$  stands for a protected payload.  $x_1$  is the displacement of the payload in Fig. 1.5(a), (b) and (c) and  $x_2$  is the displacement of connection point. The arrow through the spring in Fig. 1.5(a) implies a spring with selectable stiffnesses. Continuous variable stiffness means that system stiffness is able to achieve an arbitrary

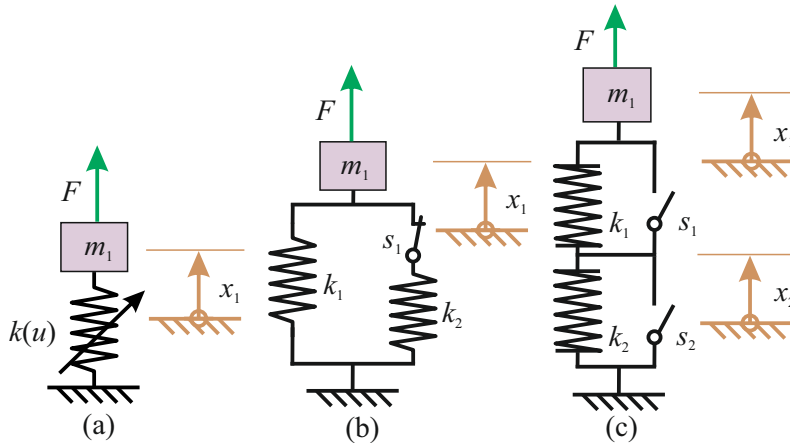


Figure 1.5.: Simplified representation for a variable stiffness system. (a) Continuous variable stiffness; (b) Parallel stiffness switching system; (c) Serial stiffness switching system.

variation within a range based on the state feedback signals. The system behavior can be given by Eq. 1.1, according to Fig. 1.5(a).

$$F = k(u)x, \quad k(u) \in [k_{\min}, k_{\max}] \quad (1.1)$$

where  $k_{\min}$  and  $k_{\max}$  are the minimum and maximum system stiffness, respectively and  $u$  is the control input. For a switched stiffness, namely, discrete stiffness, variable stiffness systems use two or more stiffness states to achieve vibration control. In between stiffness switching events, the system can be taken as a passive system. As an example, the two-stiffness systems are taken into consideration. They can be categorized into two cases and simply depicted as in Fig. 1.5(a), (b) and (c). The first case is that only two stiffness states are chosen in a continuous variable stiffness system for example,  $k_1$  and  $k_2$ . The other is a variable stiffness system with only two springs as depicted in Fig. 1.5(b), a parallel spring pair and (c), a serial spring pair. If two stiffness states are realized by a variable stiffness system as shown in Fig. 1.5(b) or (c), a mechanical switch, namely, a clamping device is applied to realize the connection or disconnection of a spring to or away from the payload  $m_1$ .

It is not difficult to see that switched stiffness is an alternative to a continuous variable stiffness. So in the following documented devices, there does not exist an obvious

boundary between switched stiffness and continuous variable stiffness. From the development in the last decades, variable stiffness devices are mainly realized by two methods. One is smart material-based devices and the other is related to common mechanical elements including mechanical spring, beam, hydraulic/pneumatic spring, and so on.

### Smart Material-based Variable Stiffness Devices

A smart material-based device is achieved by changing smart material physical properties such as elastic modulus  $E$ . In this method, these materials are generally excited by an external energy field such as electric field, magnetic field and thermal field and so on, as shown in Fig. 1.6. The energy field intensity is decided by a system state feedback signal. Examples of such materials include piezo material, Magnetorheological Elastomer (MRE), Shape Memory Alloy (SMA), and Magnetostrictive material. In some cases, smart materials can be combined with another material to make up a composite structure.

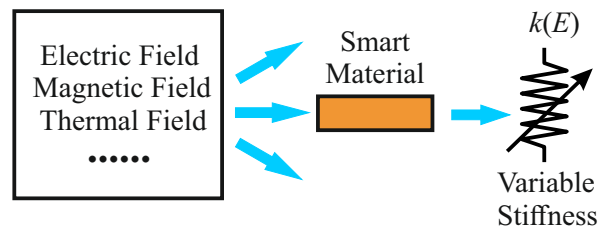


Figure 1.6.: Smart material-based stiffness variation.

#### *Piezoelectric material-based variable stiffness devices*

Piezoelectric material shows not only the direct piezoelectric effect (electric voltage produced under external mechanical strain), but also the reverse piezoelectric effect (mechanical deformation produced under external electric voltage). As such, piezoelectric materials can build up an actuator or a power source, which result in two different stiffness variation methods for vibration control, namely, a piezoelectric shunt-based variable stiffness devices and an active piezoelectric actuator-based device.

*A: Piezo shunt-based variable stiffness devices* A piezo shunt circuit acts as a medium to extract structural vibration energy from a primary structure. When the structure deforms under an external disturbance, a piezo element, or in other words, a piezo transducer, bonded to the primary structure, also strains and will convert a portion of structural vibration energy into electrical energy. By shunting the piezo transducer to an electrical shunt circuit, the induced electrical energy can be partly dissipated. This method was originally proposed by Hagood et al. [34]. During the shunting process, a desired mechanical strain of the piezo transducer results in an electrical impedance dependent stiffness variation. Different types of shunt circuits consisting of resistor, inductance and capacity can result in different stiffness variation principles, see [35]. However, it is pointed out that a switching capacity shunt circuit can realize a variable stiffness device but a switching resistor/inductor shunt circuit is not strictly

a pure variable stiffness device and can be only considered as a frequency-dependent variable stiffness one, because an electrical element, resistor or inductor, corresponds to a mechanical element, damping or mass.

In theory, one can continuously vary electrical elements such as resistors, capacity in the circuit and then obtain a continuous variable stiffness system, which has been already under a lot of investigations, see [34, 36, 37]. An alternative is to simply switch between two stiffness states. Such a configuration for switching stiffness is to operate between an open and a short circuit, which leads to the maximum and minimum system stiffness, see [38]. Clark et al. [39] put forward that a piezo shunt works better if the on-off stiffness variation can be achieved by a resistive shunt instead of a pure short circuit. In that research, a cantilevered beam with an attached piezo layer was developed. It is experimentally verified that a layered beam can reach a stiffness variation by a factor of 2, if the piezo material is operated in  $d_{33}$  mode.

*B: Active piezo actuator-based variable stiffness devices* Apart from piezo shunt-based variable stiffness devices, an active piezo actuator is also utilized for stiffness variation. In this method, for example, a piezo patch is attached onto a primary structure. Different mechanical deformations of the piezo patch, produced by a required voltage resulting from a feedback controller, lead to a stiffness variation, see [40]. Considering the sensing principle of piezo materials, an integrated smart variable stiffness device, a viscoelastic shear layer sandwiched between two layers of a piezo sensor and actuator is widely investigated. A beam structure in [41, 42] and a flat plate structure in [43] are documented, respectively. The piezo patch is stretched or contracted to change the shear deformation of viscoelastic layer and results in the system stiffness variation.

#### *SMA-based Variable Stiffness Devices*

SMA is capable of remembering its original shape and working during two transformation phases, a low temperature martensitic phase and a high temperature austenitic phase. During this process, its mechanical properties such as elastic modulus and yield stress change significantly, which can be applied to a variable stiffness design [44]. Different vibration control applications with variable stiffness built up from SMA are documented, see [45, 46]. For instance, a stiffness variation ratio greater than 2.5 was achieved over a narrow temperature range in [44] and the ratio reaches 4.5 in [46]. Williams et al. [47] pointed out that continuous control of the SMA elastic modulus is difficult when temperature is the only control input. Therefore, an on-off actuation mode of SMA elements is applied and four discrete frequencies for a tuned vibration absorber, namely, four stiffness, are produced in that research.

The variable stiffness devices based on SMA, although simple in design and inexpensive, still encounter the problem of thermal transformation hysteresis. In contrast to SMA counterparts, the change of SMP (Shape Memory Polymer) physical properties due to glass transition does not show hysteresis upon heating and cooling. Moreover, the change can reach an order of magnitude higher than SMA. Therefore, several variable stiffness devices built up from both SMA and SMP are designed for vibration absorption, where SMA serves as a heating source and structural support, and SMP plays a stiffness variation role, see [48, 49]. In [48], a cantilevered beam fabricated from SMA core and SMP sleeves was employed as a variable stiffness spring of a tuned vibration absorber. A frequency variation of 45% is experimentally obtained. Lee et

al. [49] proposed a helical spring structure with SMA wires enclosed in SMP sleeves and documented that a 61.6% change in a systems natural frequency is achieved with a control current of 1.6 A.

#### *MRE-based variable stiffness devices*

MRE belongs to the MR material family and is a solid counterpart to magnetorheological fluids (MRF). Exposed to a magnetic field, MRE exhibits a magnetorheological effect, showing a field-dependent physical property, e.g. a tunable elastic modulus and damping [50, 51]. Therefore, MRE can be applied to a variable stiffness device, see [52–54]. A tuned vibration absorber build up of two-layered MRE is developed in [53] and it is experimentally proved that the natural frequency of the absorber is able to change from 55 Hz to 82 Hz. Meanwhile, Deng et al. [53] proposed a more compact vibration absorber, whose natural frequency varies from 27.5 Hz to 40 Hz. Liao et al. [54] developed a vibration absorber based on a multi-layered MRE, where a low natural frequency less than 10 Hz is achievable.

Apart from a tunable vibration absorber, MRE is also applied to a vibration isolator with a variable stiffness property. Liao et al. [55] developed a tunable stiffness and damping vibration isolator built up from MRE, where four MRE elements are used. Experimental results indicate that this isolator outperforms its passive counterparts by a significant reduction of the payload response around the resonant frequency. Li et al. [56] demonstrated a MRE-based vibration isolator with highly adjustable stiffness. It allows a remarkable change of the isolators stiffness up to 16.3 %, which is very helpful for the implementation of an adaptive seismic isolation system. A MRE isolator for a seat suspension system is documented in [57]. It is experimentally validated that the stiffness of the isolator at a control current of 3 A is about three times as large as without an electrical field.

#### *Magnetostrictive material-based variable stiffness devices*

The elastic modulus of magnetostrictive material can be also controlled by an external magnetic field. Therefore, a variable stiffness spring is also available by means of magnetostrictive materials. In [58], tuning magnetic field realizes a stiffness variation of 10.86%. Scheidler et al. [59] proposed a variable stiffness spring with magnetostrictive material, owning a continuous modulus variation range. The change of the modulus amplitude and frequency, produced by a harmonic current, can reach 21.9 GPa and 500 Hz, respectively. Note, that the force exerted on the ends of the spring, also enables a stiffness variation to some extent.

#### *Composite beam-based variable stiffness devices*

A composite beam described here is a multilayer-material sandwiched structure. Generally, it consists of a constant stiffness material layer and a variable elastic modulus material layer, whose elastic modulus is able to change in response to an applied energy field, see [60]. Therefore, this type of composite beam supplies a possibility for a variable stiffness configuration. In [61], a composite beam with ERF is proposed. It is experimentally proven that the modulus of the composite beam increases with the electric field strength. Rajamohan et al. [62] developed a MRF layer sandwiched device. It enables the natural frequency variation by a factor of 15% and is applied for vibration suppression. In [63, 64], a composite beam filled with SMP is presented.

In an experiment, using two different polymer layer thicknesses and beam lengths, the stiffness of the beam at a low temperature is from two to four times greater than that at a high temperature.

## Mechanical Structure-based Variable Stiffness Devices

Variable stiffness devices using an adaptive mechanical structure consisting of common elements have some advantages of good stability, long life and easily available materials. So smart mechanical structure-based variable stiffness devices have also been under a lot of investigation.

Mechanical geometry change is a common technique for the production of variable stiffness devices. Each geometry side represents an elastic element. The deformation of the mechanical geometry driven by an electromechanical actuator leads to a variable stiffness with respect to a deformation angle  $\theta$ , as shown in Fig. 1.7. There exist different configurations based on the number of geometry sides. As an example, a four-spring and two-spring configuration are depicted in Fig. 1.7.

### *Mechanical Geometry Change-based Variable Stiffness Devices*

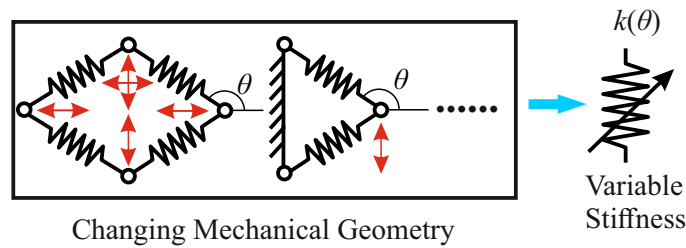


Figure 1.7.: Mechanical geometry change-based stiffness variation.

*A: Two-spring configuration* Utilizing an actuator, e.g. a stepper motor, to change the separation distance between two leaf springs allows stiffness variation in a tunable vibration absorber, see [65]. This device can be applied for the minimization of the transient vibration in start-up and shut-down conditions of engines and pumps. Similarly the devices, consisting of two beams supporting two absorber masses and connected to a primary structure, are also proposed in [66–68]. Through the curvature change of each beam, the system stiffness variation is realized. In these devices, the absorber mass is fixed to the leaf springs or curved beams and can not move through them. Hill et al. [69] proposed a double-mass absorber, which allows two masses being supported by two rods on the opposite ends. One of rods is threaded and can rotate, the other is smooth, which enables two masses to move in or out. As a result, variable stiffness is achievable through tuning the distance between two masses. Similar structures are also documented in [70, 71]. In [70], a stepper motor is incorporated into a mass, which creates the mass motion control. Mirsanei et al. [71] used a slider crank controlled by a servo motor to connect two masses. Through the deformation motion of the slider crank, the distance between two masses is changed, which results in a variable stiffness. In [72], two lateral springs are fixed to each side of a shaft, respectively and the distance between two fixed points determines the stiffness variation of

the device. This device is applied to vibration absorption and experimentally proven to have a large tuned frequency range.

*B: Four-spring configuration* Varadarajan and Nagarajaiah et.al [33, 73–76] demonstrated a variable stiffness device consisting of four springs in a planar rhombus configuration. By means of a linear electromechanical actuator together with a special instantaneous frequency control algorithm, a varying stiffness is effectively achievable. A nonlinear stiffness variation can be realized by the deformation angle  $\theta$  as shown in Fig. 1.7 and a softening or even negative stiffness would be produced at a larger relative displacement vibration. Fateh et al. [77] presented a variable stiffness bracing system comprising four nonlinear steel leaf springs and owning a large stiffness range. This system can alter its stiffness based on the input displacement and protects buildings against severe vibration and ground movement in seismic vibration control. It is numerically evaluated and proven to be effective.

*C: Other springs configuration* Apart from the above configurations, Nagaya [78] proposed a single beam together with a mass structure, which is connected to a ball screw with a movable support. The motion of ball screw creates a variable effective beam length acting on payload, which results in the system stiffness variation. Based on the single-rhombus spring configuration, Rafieipour et al. [79] demonstrated a folding variable stiffness device related to multi-rhombus mechanism made of beams and pinned connections. The effective stiffness of the device in the vertical direction is related to the geometry of the device and the mechanical properties of each element. This device is applied to a tunable mass damper and characterized remarkably by its stiffness change capability through an infinite low change of the distance between its supports. It is experimentally shown that an effective vibration suppression can be achieved using this device compared with a passive counterpart.

Apart from the mechanical geometry, changing the number of active spring coils directly to realize variable stiffness is also documented. In [80], a variable stiffness device is achieved by a helical spring and a series of plates, whose tapered edges protrude are arranged among the coils of the spring. Moving the plates towards or away from the spring leads to a change in the number of active spring coils. As a result, the spring will be stiffened or softened. This device works as a vibration absorber for a vehicle suspension system. In [81], a bi-helical spring with a mechanical arm that engages or disengages the spring coils was proposed.

#### *Mechanical Switch-based Variable Stiffness Device*

Mechanical switch-based variable stiffness devices use high and low stiffness states, which are generally realized by elastic elements together with mechanical switches as shown in Fig. 1.8. A mechanical switch is in fact a kind of friction-based clamping device. Here, as an example, a piezo actuator is arranged between two cantilevers to work as a mechanical switch. Elastic elements represent common mechanical springs  $k$  here. Two stiffness states  $k(s)$  can be produced through the releasing and clamping action of the mechanical switch denoted by  $s$ .

*Mechanical friction-based switched variable stiffness device* Onoda et al. [27] developed a variable stiffness member structure, consisting of a piezo actuator, a variable-length member and an outer element. The actuator is installed inside the member. The clamping or releasing of the member and the outer element is realized by the

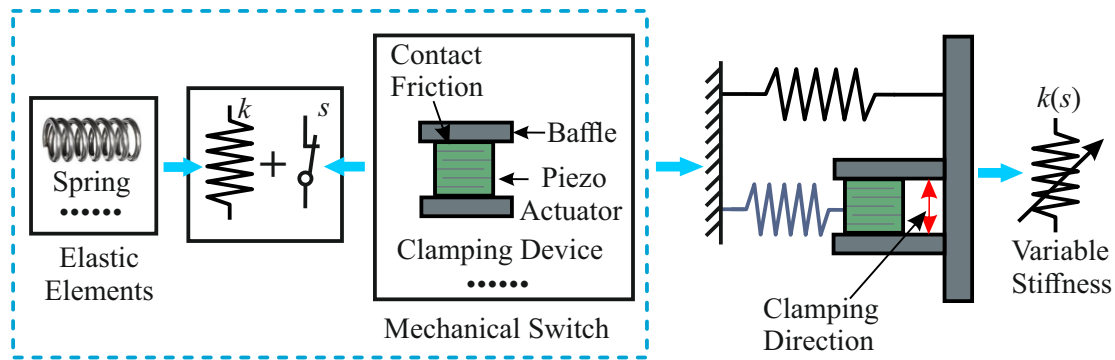


Figure 1.8.: Mechanical switch-based stiffness variation.

power on-off state of the actuator. As a result, the axial stiffness of the member can be varied. This device together with a control logic is applied to the vibration suppression of a truss structure. Yong et al. [28] documented a smart spring device, mainly consisting of two parallel springs and a piezo actuator-based clamping device like Fig. 1.8, applied for vibration reduction in helicopter blade. It is experimentally verified that the variable stiffness device is capable of suppressing multiple harmonic components in rotor vibration. Irie et al. [82, 83] proposed a switched stiffness device using an electromagnetic clutch to connect or disconnect an additional mechanical spring to or away from a primary structure for vibration isolation in a seismic environment.

*Valve-control-cylinder-based switched variable stiffness device* In [84], two controllable MRF dampers are placed in series with two springs and in parallel to two springs, respectively. The switched stiffness can be achieved through the dampers on-off states. Similar switched variable stiffness devices are also developed in [85, 86]. Greiner-Petter et al. [87] and Silge et al. [88] built a switched fluid mechanism, which uses two serial MRF dampers and two serial springs with different stiffness. This system can provide four different stiffness through the on-off state configuration of two fluids dampers. In [89], a variable stiffness and variable damping device, consisting of a MRF fluid damper with two springs, is proposed for shock absorption. Adjusting the dampers intensity in four discrete levels achieves the stiffness variation.

Apart from the use of MRF dampers together with mechanical springs, a valve-controlled hydraulic cylinder device is developed to manipulate system stiffness in [25, 90], where a cylinder piston is connected to a protected primary structure. Due to fluids flowing in a sealed cylinder, it will be stretched easily under an external disturbance acting on the primary structure. So as to avoid the fluids stretching, a resetting rule for the fluids for a short time is used to take to release the stored potential energy. As a result, the system stiffness can be taken to be variable during the short potential energy releasing time phase, see [91]. Bobrow et al. [92–94] used this device for shock isolation. Meanwhile, a variable stiffness feedback control and resetting control are analyzed and compared in [94]. It is concluded that a resetting control to manipulate the system stiffness is more effective than the variable stiffness feedback control. Youn et al. [29] changed the effective volume by opening and closing the air passages between main cylinder and two subchambers to obtain three stiffness states.

*Force Control-based Variable Stiffness Device*



Apart from a mechanical geometry change or mechanical switch action leading to stiffness variation, force control is also used to vary system stiffness as shown in Fig. 1.9. Here a pre-stressed string used as a variable stiffness element is listed as an example. Preload  $F$  changes the tension of the string and further affects the system stiffness. Since the force change responds to an infinitesimal motion, the system response of these devices is notably fast.

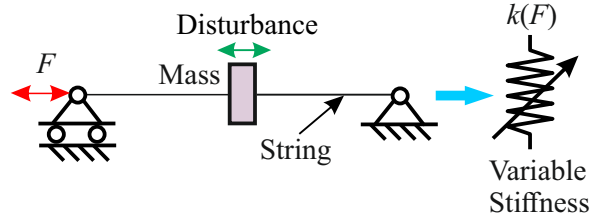


Figure 1.9.: Force control-based stiffness variation.

Chen et al. [95, 96] put forward a motion control of a large space structure by means of its in-plane tension variation. The tension of a string-type structure is kept time-variable, resulting in a time-variable stiffness. Changing the stiffness with a feedback control law, which is proportional to the string velocity, causes vibration reduction in the structure. A compressed mesh washer vibration isolator using an SMA actuator as a preload structure to change the stiffness of the mesh washer isolation material, is presented in [97, 98]. This device is able to achieve shock attenuation performance in high frequency range, and avoid vibration amplification in a low frequency range, and is applied on a launch vehicle.

Antagonistic forces, requiring a string-driven mechanism to be either kinematically singular or redundantly actuated, are the internal forces in the links of the mechanism. Antagonistic prestressed structures together with force control enables a system stiffness variation, which has a faster response, see [99, 100]. A tensegrity prism structure is presented in [101]. This device achieves both translational stiffness and rotational stiffness variation, which is experimentally validated and suggested to be applied to vibration isolation. Suzuki et al. [102] used two conic springs, arranged on each side of a mass, to achieve variable stiffness by means of exerting a different prestress on the two springs. This device has a good vibration absorption performance. The effective stiffness of the system linearly depends on the deformation of each conic spring.

### Variable Stiffness Switching Laws

The objective of vibration control is to rest a primary structure against undesired vibration effectively. Using two stiffness states not only in a continuous variable stiffness system but also in a switched stiffness system, allows for ease of vibration control. How the stiffness switching is operated in a variable stiffness system plays an important role on vibration control. This section will mainly list the variable stiffness switching laws developed in the last decades.

#### *Maximization of Vibration Energy Dissipation Switching Law*

The control strategy based on the maximum vibration energy dissipation per vibration cycle is very famous and originally proposed by Onoda et al. [27] and further improved in [103]. It can be expressed by

$$k = \begin{cases} k_{\max}, & \text{if } x\dot{x} \geq 0 \\ k_{\min}, & \text{if } x\dot{x} < 0 \end{cases}, \quad (1.2)$$

where  $k$  is the real-time stiffness,  $k_{\max}$  and  $k_{\min}$  are the maximum and minimum system stiffness,  $x$  and  $\dot{x}$  are the displacement and velocity of a protected payload. The principle will be explained in Subsection 2.2.1 in detail and a switching stiffness device can be simply modeled as shown in Figure 1.5(b). Generally, the switching between the maximum and the minimum stiffness is physically realized through a clamping device in [27, 28, 84, 104] or smart materials, see [55]. Ledezma-Ramirez et al. [19] documented that the control logic is applied to shock isolation and can outperform a linear passive system, if system damping in an vibration isolator is light.

Leitmann et al. [105, 106] proposed a control logic based on Lyapunov stability theory for vibration attenuation for a continuous variable stiffness. This control strategy aims to not only accomplish the task of maximizing the vibration energy dissipation, but also prove the stability of the controlled system. A variable stiffness system is a kind of variable structure system, so variable structure system control or sliding mode control, featuring robustness and effectiveness, is ideal for variable stiffness control. Yang et.al [107] applied a variable stiffness device together with sliding mode control for vibration isolation on a seismic-excited building. Therein, a full state feedback controller as well as a special output feedback controller are presented, respectively. In fact, the latter is proved to be the same as the switching law in Eq. (1.2). Sun et al. [86] applied a sliding mode controlled switching law to a vehicle suspension system.

#### *Resetting Actuator-based Switching Law*

Resetting actuator-based switching law mainly refers to a valve-controlled cylinder filled with compressible fluids. Earlier, Bobrow et al. [108, 109] derived the resetting control law based on Lyapunov stability theory, which resets the unstretched length of the fluids in the cylinder at each moment when the relative velocity across the damper reaches zero. The resetting action will release the vibration energy stored in the cylinder, and allow the damper to dissipate a lot of vibration energy in each motion cycle. More details related to this control logic can be also found in [110]. The system dynamics can be expressed by

$$m\ddot{x} + kx + k_1(x - x_s) = 0, \quad (1.3)$$

where  $k_1$  is the hydraulic spring stiffness due to the net effect of compressible fluids,  $x_s$  is the unstretched length of the fluids resulting from the vibration of a payload  $m$  and  $k$  is a constant stiffness. By opening the bypass valve for a short time and then closing it, the potential energy stored in the fluids can be transformed into heat. The resetting control law can be given by

$$x_s = x, \quad \text{if } \dot{x} = 0. \quad (1.4)$$

This means that the maximum potential energy stored in cylinder during one vibration

cycle is released and after a short time, the bypass valve is closed and the system stiffness will reach  $k + k_1$  again. This device has been validated for seismic response control in a six-storey building, see Yang et al. [111] and a three-storey building in [112].

#### *Acceleration-based Switching Law*

A simple on-off variable stiffness switching law based on the acceleration of a primary structure is applied to base isolation in [83], where a desired acceleration threshold  $\ddot{x}_{\text{threshold}}$  is set initially. If the acceleration of the primary structure is larger than the threshold value, an electromagnetic clutch connects an additional device to the primary structure, and potential energy is stored in the additional device. When the acceleration amplitude decreases below the threshold, the clutch disconnects the additional device from the primary structure and the stored potential energy will be released at once. This control logic can be expressed as

$$k = \begin{cases} k_{\max} , & \text{if } \ddot{x} \geq \ddot{x}_{\text{threshold}} \\ k_{\min} , & \text{if } \ddot{x} < \ddot{x}_{\text{threshold}} \end{cases} . \quad (1.5)$$

where  $\ddot{x}$  is the real-time acceleration of the primary structure and  $\ddot{x}_{\text{threshold}}$  is the desired acceleration. In that research, it was experimentally proven that vibration isolation is realized effectively.

#### *Skyhook Control-based Switching Law*

Skyhook control is early proposed for system damping control in [113]. This control logic based on damping adjustment allows the maximum vibration isolation in a primary structure and has been well documented in [7]. Cunefare et al. [114] uses this control logic in stiffness variation for vibration absorption, as expressed in Eq. (1.6). This can be physically interpreted that when a force, produced by a vibration absorber, acts on the primary structure in the opposite direction of base motion, a stiffer spring removes more energy from the base. Conversely, a softer spring is used when the force acts in the same motion direction of the primary structure. This leads to less energy being brought into the primary structure.

$$k = \begin{cases} k_{\min} , & \text{if } \dot{x}(\dot{x}_{\text{absorber}} - \dot{x}) \geq 0 \\ k_{\max} , & \text{if } \dot{x}(\dot{x}_{\text{absorber}} - \dot{x}) < 0 \end{cases} , \quad (1.6)$$

where  $\dot{x}$  stands for the velocity of the primary structure and  $\dot{x}_{\text{absorber}}$  is the velocity of the absorbers mass. This switching law does not guarantee a minimized primary structure motion, see [115]. The operation of an absorber together with this switching law for vibration absorption of a continuous system such as a beam and a plate, was considered in that research.

In addition, a switched damping together with Skyhook control can also achieve the stiffness variation in a combined device including both a spring and a damping. For instance, Liu et al. [84, 85, 116] proposed a stiffness on-off control based on on-off controllable damping for vibration isolation in a two-degree-of-freedom system. This system is experimentally proven to have a better isolation performance than a conventional variable damping system. In this method, two variable dampers are controlled by the maximum vibration energy dissipation as stated in switching logic (1.2) and Skyhook control logic, respectively.

Due to MRE showing that its stiffness and damping increase monotonically with the increase of magnetic flux density, Opie et al. [30, 117] developed a vibration isolation device, built up from MRE, together with the Skyhook control-based switching law in order to minimize the absolute velocity of a primary structure. The switching law can be given by

$$k = \begin{cases} k_{\min}, & \text{if } \dot{x} [P(x - x_0) + (\dot{x} - \dot{x}_0)] \leq 0 \\ k_{\max}, & \text{if } \dot{x} [P(x - x_0) + (\dot{x} - \dot{x}_0)] > 0 \end{cases}, \quad (1.7)$$

where  $x, \dot{x}$  stand for the displacement and velocity of the primary structure and  $x_0, \dot{x}_0$  are the displacement and velocity of base excitation, respectively.  $P$  is a non-negative coefficient dependent on an accurate model of the vibration isolation device. Experimental results show that the MRE isolation system reduces the absolute velocity of the primary structure by 30% compared to a passive counterpart.

#### *Switching Law for Variable Stiffness Control with a Piezo Shunt*

Differing from vibration energy dissipation realized by mechanical structure, piezo shunt-based variable stiffness systems utilize an electrical impedance to dissipate vibration energy. How to control the mechanical strain of piezo element and transform a portion of vibration energy into electrical energy and then discharge through a shunt circuit will be focused on in this subsection.

*A: Maximum Strain-based Switching Law* The maximum strain of a piezo transducer corresponds to the maximum vibration energy transformation. As a result, when the piezo transducer reaches the maximum mechanical deformation, it will be switched into a shunt circuit, short- or resistive-circuit (low stiffness) for a short duration and then discharged completely. Afterwards, the piezo transducer is switched into open circuit (high stiffness) configuration again. This allows the voltage to be produced further across the electrodes, until the next displacement extreme occurs [37, 118]. It is obvious to see that the piezo transducer stays in the high-stiffness state for most of the vibration cycle, but it is momentarily pulsed to the low-stiffness state to dissipate the stored energy. In [119–121], the switch is again synchronized with the displacement extreme. Instead of discharging the piezo transducer, its voltage is quickly inverted via a resonant network. Compared with the above control logic, this one is the most efficient semi-passive technique, but its drawback is the need for an external power supply. In order to solve the needed external power problem, self-powered piezo structural vibration control systems are documented in [122, 123].

*B: State-switched Switching Law* Similar to [37], Clark et.al [39] proposed a state-switched control logic to apply to a shunted piezo transducer to realize vibration energy dissipation, but the difference from the above stated control logic is that this method keeps the piezo transducer in each of the high- and low-stiffness states for one quarter-cycle increment, not most of a vibration cycle. When system is moving away from equilibrium and kinetic energy is decreasing, the actuator is in an open-circuit configuration, i.e. high stiffness state, and energy is stored in piezo transducer. When the system is moving toward equilibrium and needs to receive energy from the piezo transducer, the transducer will be set to the short-circuit, namely, low stiffness state, this leads to energy dissipation and therefore, vibration control is achievable. In fact, this control logic is the same as *Maximum vibration energy dissipation-based control logic*.

## 1.2. Summary of Literature Review

From the above literature review, it is concluded that

1. Variable stiffness-based vibration control systems have been widely studied for vibration suppression, vibration isolation, and vibration absorption. Stiffness variation can be realized by smart material-based devices and special mechanical structures;
2. Continuous variable stiffness can be controlled by a continuous variable energy field such as magnetic field, temperature field, or force field, acting on a smart material-based or a special mechanical structure. Switched stiffness, on one hand, can be a simple alternative of continuous variable stiffness, where the maximum or minimum stiffness are chosen from a continuous variation range. On the other hand, it can also be realized by special stiffness state switching devices such as a mechanical switch or a piezo shunt;
3. Many of the variable stiffness systems proposed are active systems, power can flow in both directions, into or out of the vibrational system, although many authors define their system as semi-active.
4. The presented concepts of switched stiffness devices for vibration reduction use energy dissipation to extract the stored potential energy in a different vibration mode within each vibration cycle of the payload.
5. In current mechanical structures and control concepts for vibration reduction there are always time spans where part of the repeatedly stored potential energy in the spring is released as kinetic energy of the load mass, extending the settling time.

## 1.3. Objective

The outcome of the literature review, condensed in the summary Sec. 1.2, indicates that the current semi-active concepts or devices for vibration reduction use energy dissipation, i.e. transformation of kinetic energy into heat, see No. 4 in Section 1.2. Furthermore, in all cases part of the kinetic energy stored as potential energy in springs is released back into the kinetic energy of the mechanical structure, see No. 5 in Section 1.2. In the Mechatronics Group at TU Ilmenau a semi-active system combining variable stiffness with damping mechanism, which is controlled by magnetorheological valves, was proposed in [87] and is shown in Fig. 1.10. The concept is chosen and slightly modified by removing the damping elements and using two equal stiffness. Further, feedback control is introduced. These modifications result in a new concept and system being the starting point of the thesis.

The thesis objective is to investigate the new system for vibration reduction tasks, which means performing vibration reduction without damping and without releasing energy back into the mechanical structure. Instead of releasing the potential energy, the vibrational energy is stored or harvested in the springs. The idea of vibration energy harvesting instead of energy dissipation will be used to counteract disturbance

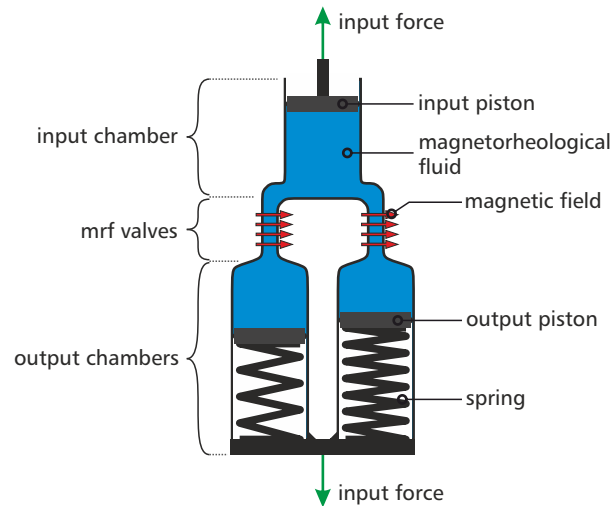


Figure 1.10.: Variable stiffness and damping mechanism together two magnetorheological valves [87].

forces like an actuator in vibration compensation. The new system is called 4S as the abbreviation for Serial-Stiffness-Switch-System. In this thesis the principle vibrational behavior needs to be investigated in detail and control concepts have to be found which perform in the planned manner. For the analysis and system design, analytical, numerical and experimental approaches are applied.

## 1.4. Contribution

The authors contribution to extend state of the art in semi-active vibration reduction concepts and devices is

- Suggestion of a new semi-active vibration reduction concept as outlined in Objectives. The proposed system is able to harvest the vibrational energy into the springs and use the stored potential energy to work as an actuator against perturbation forces.
- Analytical, numerical and experimental proof-of-concept for the proposed system is shown under harmonic force disturbance at supercritical excitation of a payload mass. It is shown that the system approaches a steady-state response by an appropriate switching law.
- Initial velocity disturbance compensation, namely, shock compensation is proven by the introduction of a new switching law or control law. The numerical and experimental investigations showed that the settling time to the position at rest can be reduced by the factor of 20 compared to the original velocity-base switching law.
- Shock isolation capability is shown under pre-tensioned springs by numerical simulation analysis. One outcome is that shock isolation of the system works in the complete shock response spectrum both in the high as well as the low

frequency region. Especially the isolation in the low frequency region, below the first eigenfrequency of the mechanical structure, is a novel result and extends current concepts, which work only above the first eigenfrequency. Thus, the proposed system can outperform existing semi-active device concepts.

## 1.5. Thesis Organization

To conduct a theoretical and experimental study on the proposed novel semi-active vibration control strategy, a simplified model, consisting of a mass and two serial-stiffness-switch elements, is considered throughout this work. The thesis is organized as follows,

In Chapter 1 the background of this thesis is initially introduced. An overview of different contributions in the area of variable stiffness devices together with switching laws for vibration control is presented. Following is the objective and contributions in this work.

Chapter 2 contains the information on the modeling, operation principle and system dynamics of novel semi-active vibration control system. 4S in open loop and closed loop control are numerically analyzed, respectively. The equivalent stiffness and natural frequency of the switching system are mathematically formulated and verified through Fast Fourier Transformation. A switching law based on vibration energy harvesting is also numerically analyzed.

In Chapter 3 vibration energy harvesting limitation is theoretically and numerically analyzed. In order to further show the energy harvesting limitation, a long time simulation is carried out.

A rotational setup is designed in Chapter 4. Two ring-arranged electromagnet-plates together with one armature-shaft work as two mechanical switches. The operation principle, modeling, construction and the corresponding experiment are carried out.

To improve the system response, a new switching law based on variable structure system control theory is further proposed in Chapter 5. Non-zero initial velocity and harmonic excitation processes are numerically and experimentally verified.

In Chapter 6 shock isolation performance is numerically tested on 4S with the comparison of a passive and a semi-active system. Considering 4S can harvest vibration energy, a potential energy pre-storage is applied before shock.

Finally, the main conclusions from this thesis are summarized in Chapter 7 and recommendations for future work are also made.





---

# Novel Semi-active Vibration Control with 4S

---

## 2.1. Introduction

In most of the mentioned vibration control systems in Introduction, there still exist unavoidable time instants during a vibration reduction process, where an elastic element releases the stored potential energy, and drives a protected payload to move again. This is an intrinsic property of the elastic element and results in an oscillation in the systems to some extent.

In order to solve the problem, a novel semi-active vibration control strategy based on vibration energy harvesting is proposed in this chapter. The basic idea introduced in this chapter is a modification of the idea presented by Greiner-Petter, Tan and Sattel [87], where a MRF valve controlled variable stiffness and damping mechanism was proposed. The modifications include the removal of the damping elements and using two equal stiffness as was already outlined in Section 1.3 (Objective).

Before introducing the new system or concept, vibration reduction issues about a passive and a semi-active vibration control system are formulated and then a new semi-active vibration control concept related to Serial-Stiffness-Switch-System (4S) is put forward and analyzed. In a preliminary study, 4S in open loop control is analytically and numerically interpreted, where the equivalent stiffness and natural frequency of the switching system are given. Finally, a velocity zero-crossing switching law based on vibration energy harvesting is introduced. It is numerically proven that 4S shows vibration energy harvesting and vibration reduction performance. A harmonic disturbance will be always exerted on 4S in this chapter. The corresponding theoretical analysis is also demonstrated in Min et al. [124].

## 2.2. 4S Concept

Potential energy releasing of an elastic element leads to an acceleration of the protected payload once again during a vibration reduction process. This phenomenon will be explained in the following subsection in detail.

### 2.2.1. Problem Statement

For the sake of a simple explanation, all elastic elements through the work are denoted as springs. At first, a passive single-degree-of-freedom (SDOF) model is considered, as sketched in Fig. 2.1(a). The equation of motion is given by

$$m_1\ddot{x}_1 = F - d\dot{x}_1 - kx_1, \quad (2.1)$$

where  $x_1$  is the payload displacement and  $m_1$ ,  $k$  and  $d$  are mass, stiffness and damping parameters of the system, respectively. The force  $F$  represents the external disturbance and is considered to be a pulse in this case. The objective of vibration control as

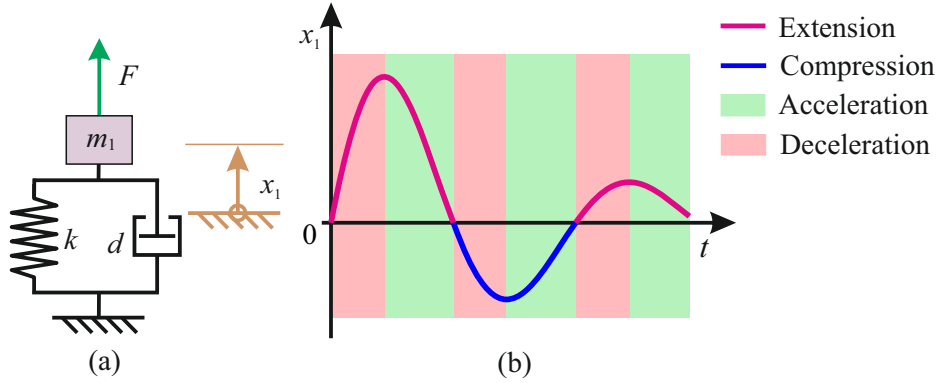


Figure 2.1.: Schematics for  $m_1$ - $k$ - $d$ -system. (a) Simplified model; (b) Displacement response for an external pulse disturbance.

understood here is to achieve vibration reduction, which moves a payload  $m_1$  back to its equilibrium position  $x_1 = 0$ . Multiplying Eq. (2.1) with the velocity  $\dot{x}_1$  results in the mechanical power balance

$$m_1\ddot{x}_1\dot{x}_1 = F\dot{x}_1 - d\dot{x}_1^2 - kx_1\dot{x}_1, \quad (2.2)$$

and can be rewritten as

$$\frac{dT}{dt} = F\dot{x}_1 - d\dot{x}_1^2 - \frac{dU}{dt}, \quad (2.3)$$

where  $T$  is defined as kinetic energy,  $T = \frac{1}{2}m_1\dot{x}_1^2$  and  $U$  is potential energy,  $U = \frac{1}{2}kx_1^2$ . In order to achieve vibration reduction, the kinetic energy should not increase, namely,  $dT/dt < 0$ . The damping  $d$  leads to a permanent reduction of kinetic energy, since  $d\dot{x}_1^2 > 0, \forall \dot{x}_1 \neq 0$  always holds. To further reduce the kinetic energy  $T$ , the potential energy  $U$  has to increase:  $dU/dt > 0, \forall t \geq 0$ . However, this is not possible to realize for all time instants in a passive system as depicted in Fig. 2.1(a), because in all

vibration systems with  $D = d/(2\sqrt{km}) < 1$ , there exist not only the time phases with  $dU/dt = kx_1\dot{x}_1 > 0$ , denoted by pink area in Fig. 2.1(b), but also the time phases with  $dU/dt = kx_1\dot{x}_1 < 0$ , denoted by green area. The potential energy stored during the deceleration phases of the payload  $m_1$ ,  $kx_1\dot{x}_1 > 0$ , will be completely released in the acceleration phase,  $kx_1\dot{x}_1 < 0$ .

Using a semi-active vibration control system with two springs,  $k - \Delta k$  and  $\Delta k$  to store potential energy  $U_1 = (k - \Delta k)x_1^2/2$  and  $U_2 = \Delta kx_1^2/2$ , together with a specified switching law between these two springs offers possibilities for vibration reduction as depicted in Fig. 2.2. One possibility is to use a larger changing rate of potential energy in time phases where the spring decelerates the payload, i.e. for  $dU/dt > 0$  and a smaller changing rate of potential energy is chosen in time phases where the spring accelerates the payload, i.e. at  $dU/dt < 0$ , see Onoda et al. [27] and Ledezma-Ramirez et al. [19]. This is similar to the damped passive system in Fig. 2.1(b) by the pink and green areas. To do so, in the deceleration phase, when the kinetic energy of payload  $m_1$  decreases, both springs are active, depicted by pink area and in the acceleration phase, when the kinetic energy of payload  $m_1$  increases, only one spring is taken, as shown by green area. That is to say, during a deceleration phase,  $\frac{d(U_1+U_2)}{dt} > 0$  and for an acceleration phase  $\frac{dU_1}{dt} \leq 0$ . The potential energy  $U_2$  will be dissipated in the form of thermal energy by a damping element  $\Delta d$ , when the spring  $\Delta k$  is disconnected from the payload  $m_1$ . Finally, the kinetic energy of the payload is removed from the system by repeatedly switching the springs and vibration reduction performance is achieved. The

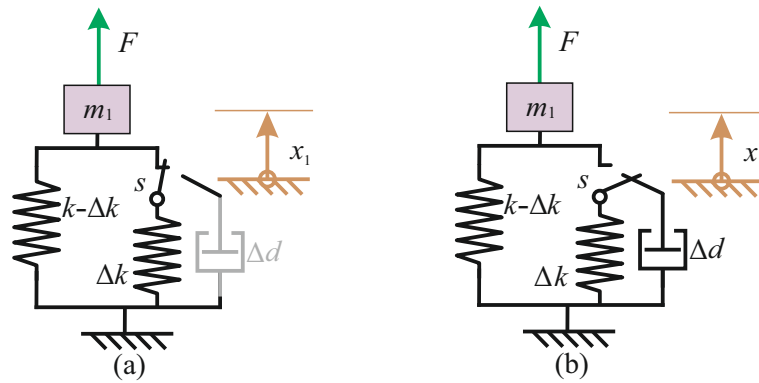


Figure 2.2.: Schematic of a parallel-stiffness-switch system: (a)  $k - \Delta k$  and  $\Delta k$  are connected to payload  $m_1$ ; (b) Only  $k - \Delta k$  is connected to payload  $m_1$ .

system behavior has already been investigated under different disturbances, e.g. shock excitation, see [19] or harmonic excitation, see [32]. The switching law is given by the changing rate of potential energy,  $dU/dt = k_{\text{eff}}x_1\dot{x}_1$  and describes the resulting switching stiffness  $k_{\text{eff}}$

$$k_{\text{eff}} = \begin{cases} k & \text{if } x_1\dot{x}_1 > 0 \\ k - \Delta k & \text{if } x_1\dot{x}_1 \leq 0 \end{cases} . \quad (2.4)$$

The resultant stiffness  $k_{\text{eff}} = k$  corresponds to the pink areas in Fig. 2.1(b) and  $k_{\text{eff}} = k - \Delta k$  to the green ones. In such an arrangement spring  $\Delta k$  always decelerates the payload, but spring  $k - \Delta k$  still both decelerates and accelerates the payload  $m_1$ .

### 2.2.2. Vibration Energy Harvesting Concept

To avoid this, i.e. to ensure that springs permanently decelerate the payload, another way to remove kinetic energy from the system is proposed. Instead of switching between acceleration and deceleration time phases, corresponding to the pink and green areas in Fig. 2.1(b), the idea is to use only decelerating phases. Therefore, the two directions of the payload motion should be split up between two springs  $k_1$  and  $k_2$ . This means that the first spring  $k_1$  is only active in its increasing extension phase and  $k_2$  only active in its increasing compression phase. Thus, for both springs the terms of the changing rate of potential energy should be larger than zero, which is illustrated in Fig. 2.3(b) by the red and blue lines of the time history  $x_1(t)$  for a passive system  $m_1-k$ . A way

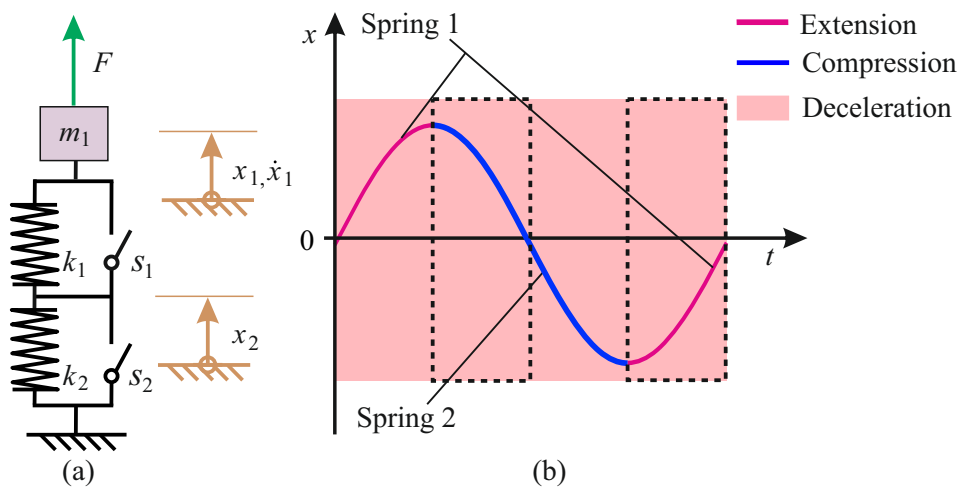


Figure 2.3.: Schematic for 4S. (a) 4S model; (b) Connection of two springs over time.

for the concept realization would be to have two springs in series together with two switches, according to Fig. 2.3(a), which is called “4S” (Serial-Stiffness-Switch-System). This leads to the necessary conditions,  $k_1 x_1 \geq 0 \wedge \dot{x}_1 \geq 0$  for an increasing extension and  $k_2 x_1 < 0 \wedge \dot{x}_1 < 0$  for an increasing compression. In fact, a similar serial stiffness structure has already been proposed by [84], but the operation principle is different. In the work presented here, a separation of extension and compression phases takes place, which means that one spring is always under compression and the other always under extension. Consequently, the springs are not active in the system at the same time. The switching law is given by the zero-crossing of velocity,  $\dot{x}_1$ , separating time phases with  $\dot{x}_1 \geq 0$  and  $\dot{x}_1 < 0$ . Instead of dissipating the stored potential energy in each vibration cycle and realizing vibration reduction, the kinetic energy of the payload will be harvested. When the disturbance  $F$  vanishes, the stored potential energy can be either used by the system, working as an actuator, or dissipated similarly to the system with the parallel springs in Fig. 2.2(b), by means of opening two switches  $s_1$ ,  $s_2$  at the same time.

### 2.2.3. 4S Model

As shown in Fig. 2.3(a), the model comprises of two serial springs  $k_1$ ,  $k_2$ , payload  $m_1$  and two switches  $s_1$ ,  $s_2$ , which in fact are two clamping devices. These devices might be realized by smart material such as piezoelectric, electromagnetic or magneto-rheological fluids material and govern the operation order of two springs. To begin, the clamping devices are not considered in detail and only simplified as switch  $s_1$  and  $s_2$  for the analysis.  $F$  stands for external excitation,  $x_1$  is the displacement of payload and the displacement of connection point of two springs is symbolized as  $x_2$ . Both switches own two working states, namely, open or close, which result in the connection or disconnection of each spring to or away from the payload  $m_1$ . So there exist four switching groups between  $s_1$  and  $s_2$ , which produces four different types of system stiffness  $k(\mathbf{S})$  as expressed in Eq. (2.5)

$$k(\mathbf{S}) = \begin{cases} k_1 & \text{if } \mathbf{S}(t) = [1, 0] \\ k_2 & \text{if } \mathbf{S}(t) = [0, 1] \\ \frac{k_1 k_2}{k_1 + k_2} & \text{if } \mathbf{S}(t) = [1, 1] \\ - & \text{if } \mathbf{S}(t) = [0, 0] \end{cases}, \quad (2.5)$$

where  $k(\mathbf{S})$  is the stiffness of the switched system and  $\mathbf{S}(t)$  is defined as a switching control vector for  $s_1$ ,  $s_2$

$$\mathbf{S}(t) = [s_1(t), s_2(t)], \quad s_i(t) \in \{0, 1\}, \quad i = (1, 2). \quad (2.6)$$

Here  $s_i(t) = 0$  means that the  $i$ th spring is disconnected away from the payload; Conversely,  $s_i(t) = 1$  represents the  $i$ th spring being connected. The operation order for the two switches is also listed in Table 2.1 for ease of interpretation.

Table 2.1.: Operation order of two springs

Control vector ( $\mathbf{S}$ )	Switching condition	Spring connection
[1, 1]	$s_1, s_2$ open	$k_1, k_2$
[0, 1]	$s_1$ closed and $s_2$ open	$k_2$
[1, 0]	$s_2$ closed and $s_1$ open	$k_1$
[0, 0]	$s_1, s_2$ closed	not allowable

Based on Newtons law of motion the dynamics of 4S, sketched in Fig. 2.3(a), can be given as follows. If  $\mathbf{S}(t) = [1, 0]$ , the system dynamics can be given by

$$m\ddot{x}_1 + k_1(x_1 - x_2) = F, \quad \wedge \quad x_2 = x_2(t_{\text{sw},i}), \quad (2.7)$$

and in case of  $\mathbf{S}(t) = [0, 1]$  by

$$m\ddot{x}_1 + k_2 x_2 = F, \quad \wedge \quad x_2 = x_1 - [x_1(t_{\text{sw},i}) - x_2(t_{\text{sw},i})]. \quad (2.8)$$

where  $t_{\text{sw},i}$  is the  $i$ -th switching time instant with the subscript “sw”. When  $\mathbf{S}(t) = [1, 1]$ , two springs are active and the motion equations can be given as follows,

$$m\ddot{x}_1 = F - k_1(x_1 - x_2) , \quad \wedge \quad k_2x_2 = k_1(x_1 - x_2) . \quad (2.9)$$

Each subsystem Eqs. (2.7)-(2.9) behaves as a SDOF system. However, the system has three state variables,  $(x_1, \dot{x}_1, x_2)$ . The case  $\mathbf{S}(t) = [0, 0]$ , where both of two springs are not active, is not allowable in practice. In order to have a more compact description, Eqs. (2.7)-(2.9) will be combined as

$$m_1\ddot{x}_1 + k(\mathbf{S})x_1 = F + F_p(\mathbf{S}) \quad (2.10)$$

and

$$x_2(\mathbf{S}) = \begin{cases} x_2(t_{\text{sw},i}) & \text{if } \mathbf{S}(t) = [1, 0] \\ x_1 - [x_1(t_{\text{sw},i}) - x_2(t_{\text{sw},i})] & \text{if } \mathbf{S}(t) = [0, 1] \\ \frac{k_1}{k_1 + k_2}x_1 & \text{if } \mathbf{S}(t) = [1, 1] \\ - & \text{if } \mathbf{S}(t) = [0, 0] \end{cases} , \quad (2.11)$$

where  $x_2(\mathbf{S})$  is the displacement of the connection point between two springs and the process force is defined as  $F_p(\mathbf{S})$ ,

$$F_p(\mathbf{S}) = \begin{cases} k_1u_2(t_{\text{sw},i}) & \text{if } \mathbf{S}(t) = [1, 0] \\ k_2u_1(t_{\text{sw},i}) & \text{if } \mathbf{S}(t) = [0, 1] \\ 0 & \text{if } \mathbf{S}(t) = [1, 1] \\ - & \text{if } \mathbf{S}(t) = [0, 0] \end{cases} , \quad (2.12)$$

with the deformation of the two springs  $u_1$  and  $u_2$  defined as

$$u_1 := x_1 - x_2 , \quad u_2 := x_2 . \quad (2.13)$$

In order to realize the compression and extension spring configuration, the switching cases  $\mathbf{S}(t) = [1, 0]$  and  $\mathbf{S}(t) = [0, 1]$  are chosen. At first, the stiffnesses  $k_1 = k_2 = k$  are used in this work considering that a switching behavior is symmetric for  $\mathbf{S}(t) = [1, 0]$  and  $\mathbf{S}(t) = [0, 1]$ . Finally, the system dynamics would be further simplified as

$$m_1\ddot{x}_1 + kx_1 = F + F_p(\mathbf{S}) \quad (2.14)$$

and

$$x_2(\mathbf{S}) = \begin{cases} x_2(t_{\text{sw},i}) & \text{if } \mathbf{S}(t) = [1, 0] \\ x_1 - [x_1(t_{\text{sw},i}) - x_2(t_{\text{sw},i})] & \text{if } \mathbf{S}(t) = [0, 1] \end{cases} , \quad (2.15)$$

and the process force  $F_p(\mathbf{S})$  is given by

$$F_p(\mathbf{S}) = \begin{cases} ku_2(t_{\text{sw},i}) & \text{if } \mathbf{S}(t) = [1, 0] \\ ku_1(t_{\text{sw},i}) & \text{if } \mathbf{S}(t) = [0, 1] \end{cases} , \quad (2.16)$$

where it is a piecewise constant force. Note that in Eq. (2.10) the actual spring forces  $F_k$  are split into two components, the process force  $F_p(\mathbf{S})$ , which is constant within a

switching state and the time varying part  $kx_1$ ,

$$F_k(\mathbf{S}) = kx_1 - F_p(\mathbf{S}) . \quad (2.17)$$

Yet, no switching law has been proposed. The system can be driven in open loop or closed loop control.

## 2.3. Open Loop Control for 4S

In order to preliminarily study the performance of 4S, it will be analyzed under supercritical disturbance force excitation in open loop control, in which 4S is operated under a specified switching sequence and independent of the system state variables,  $(x_1, \dot{x}_1, x_2)$ . Investigations of critical and subcritical excitation are left for further studies. Exemplary, the theoretical analysis is done for a supercritical excitation,  $\eta_d = 10$ , in the following chapters.

### 2.3.1. Numerical Analysis

The numerical analysis is executed under a harmonic disturbance

$$F(t) = \hat{F} \sin \Omega t . \quad (2.18)$$

When a regular switching between two springs happens in 4S, a switching time period  $T_{sw}$ , in which two springs are active only one time, and the corresponding switching frequency  $\Omega_{sw}$  are defined as

$$\Omega_{sw} = \frac{2\pi}{T_{sw}} . \quad (2.19)$$

During a switching period  $T_{sw}$ , the time phases where these two springs  $k_1$  or  $k_2$  are active are called  $T_1$  or  $T_2$ , respectively, and then the switching period  $T_{sw} = T_1 + T_2$ . The two switches  $s_1, s_2$  are considered to open and close instantaneously. A duty cycle  $D_{k1}$  is defined for  $k_1$  as

$$D_{k1} = \frac{T_1}{T_{sw}} = \frac{T_1}{T_1 + T_2} , \quad (2.20)$$

and  $(1 - D_{k1})$  is the duty cycle of  $k_2$ . The time behaviors of the open loop controlled 4S under four different duty cycles are investigated, here  $D_{k1} \in [0, 0.1, 0.3, 0.5]$ . Due to the complementary choice of the switching states for the two switches, one stiffness state sufficiently represents the switching sequence signals. Consequently, only the operation state of switch  $s_1$  is illustrated in Fig. (2.4). For example, if  $s_1 = 0$ ,  $\mathbf{S}(t) = [0, 1]$  and if  $s_1 = 1$ ,  $\mathbf{S}(t) = [1, 0]$ .

Three different system response frequencies occur in 4S, the natural frequency  $\omega_0$  of each subsystem,  $m_1-k_1$  or  $m_1-k_2$ , according to Eq. (2.21), here  $k_1 = k_2 = k$ ,

$$\omega_0 = \sqrt{\frac{k}{m_1}} , \quad T_0 = \frac{2\pi}{\omega_0} . \quad (2.21)$$

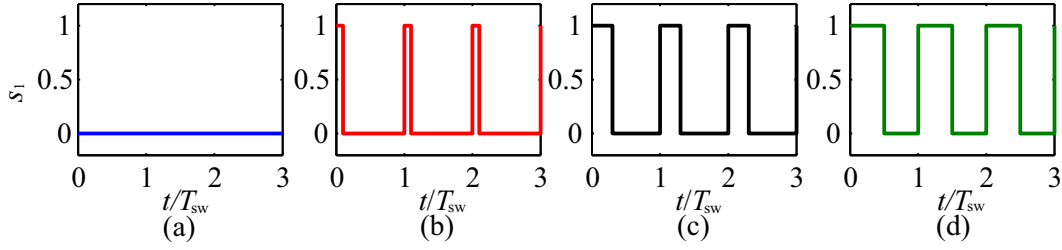


Figure 2.4.: Switching sequences for different duty cycles  $D_{k1}$ . (a) Blue:  $D_{k1} = 0$ ; (b) Red:  $D_{k1} = 0.1$ ; (c) Black:  $D_{k1} = 0.3$ ; (d) Green:  $D_{k1} = 0.5$

Table 2.2.: Simulation parameters for open loop controlled 4S.

Name	Value	Unit	Name	Value	Unit	Name	Value	Unit
$\hat{F}$	1	N	$\eta_d$	10	-	$x_1(0)$	0	m
$m_1$	1	kg	$\eta_{sw}$	500	-	$\dot{x}_1(0)$	0	m/s
$k$	1	N/m	$D_{k1}$	variable	-	$x_2(0)$	0	m

the external disturbance frequency  $\Omega$  and the switching frequency,  $\Omega_{sw}$ , which will be related by two quantities, the dimensionless disturbance frequency  $\eta_d$  and the dimensionless switching frequency  $\eta_{sw}$ , according to

$$\eta_d = \frac{\Omega}{\omega_0}, \quad \eta_{sw} = \frac{\Omega_{sw}}{\omega_0}. \quad (2.22)$$

The system parameters for the numerical analysis are listed in Table 2.2, here the dimensionless switching frequency  $\eta_{sw}$  is very high compared to the dimensionless disturbance frequency  $\eta_d$ . The Eqs. (2.14)-(2.15) can be piecewise integrated analytically and solved on an algebraic level by formulating transition conditions between switching time instants  $t_{sw,i}$ . For the sake of simplicity, the numerical simulation are carried out in MATLAB/Simulink here.

The colors in Fig. 2.4(a)-(d) stand for the different duty cycle  $D_{k1}$  cases. The system response in terms of the displacement  $x_1$  and velocity  $\dot{x}_1$  of the payload and the spring deformations  $u_1$  and  $u_2$  are shown in Fig. 2.5. There are two columns of subfigures, marketed by a-h, respectively. The cyan lines in Fig. 2.5(a)-(d) represent the zoom-in windows of the plots given in the right side Fig. 2.5(e)-(h). However, only the curves for the duty cycle  $D_{k1} = 0.3$  in Fig. 2.5(e)-(h) are plotted because all response curves for different  $D_{k1}$  are similar. In the enlarged Fig. 2.5(e)-(h) a light blue area represents  $s_1 = 1$ , which denotes  $k_1$  being active, and a light green area represents  $s_1 = 0$  and  $k_2$  is active.

Fig. 2.5(a)-(d) show when  $D_{k1} = 0$ , only  $u_2$  varies because only  $k_2$  is active. 4S can be seen as a passive undamped  $m_1$ - $k$  system, whose system response is the superposition of the free response in terms of system properties and the forced response with respect to an external disturbance. When  $D_{k1} \neq 0$ , 4S is forced to switch based on the switching sequences shown in Fig. 2.4. The system response of 4S(Red, Black and Green) are similar to that of the passive undamped system(Blue), but the fundamental



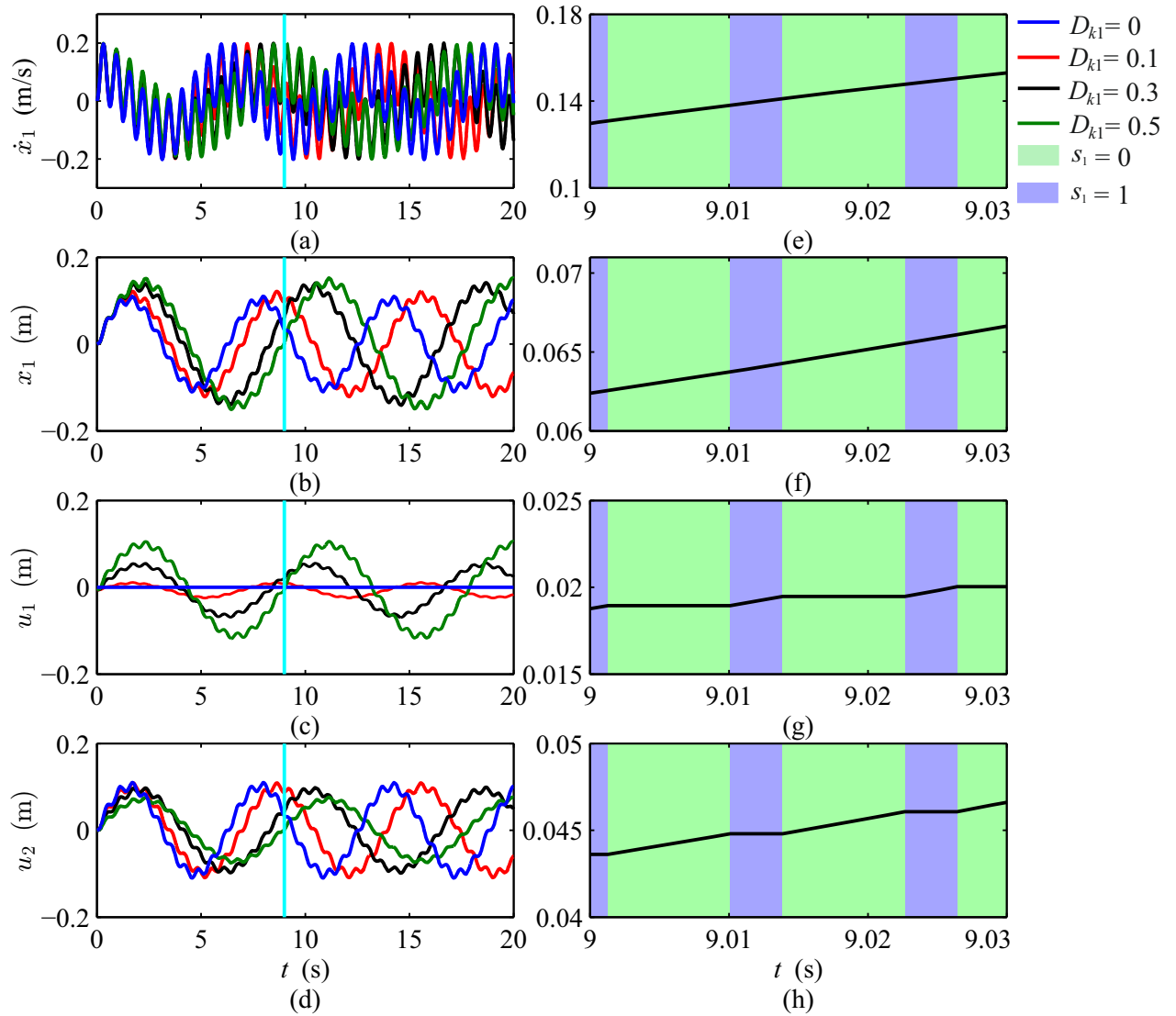


Figure 2.5.: System response of 4S at open-loop control for four different duty cycles. (a)-(d) and (e)-(h) are payload velocity,  $\dot{x}_1$ , payload displacement,  $x_1$ , the deformations of two springs,  $u_1$  and  $u_2$ , respectively. Right side is a zoomed-in at the cyan line on the left. The colors in (a)-(d) correspond to the duty cycle colors in Fig. 2.4.

amplitude and period of the system response show differences. With the increase of  $D_{k1}$  from 0 to 0.5, the fundamental period of 4S also increases, which means that the equivalent frequency and stiffness of the switched system decreases. Generally, stiffness and natural frequency are defined for linear systems, so equivalent stiffness and natural frequency are defined for the switched system here. Fig. 2.5(c)-(d) show the deformations of the two springs  $u_1$ ,  $u_2$ . Their response time behaviors seem similar for different duty cycles, but their amplitudes and periods are different.

In Fig. 2.5(e)-(h) the ratio of light blue area to light green area is equal to 3 : 7, because  $D_{k1}$  is equal to 0.3. Due to the switching between two springs, the deformations of the two springs show an intermittent variation, but the displacement and velocity of the payload  $m$  change continuously because of a rapid switching and the inertia of the payload. In order to further find out the effects of the duty cycle on the deformations of the two springs, the equivalent stiffness and natural frequency of the switched system, an analytical investigation is carried out in the following subsection.

### 2.3.2. Analytical Formulation

In this subsection, the equivalent stiffness  $k_{eq}$  and equivalent natural frequency  $\omega_{eq}$  of the switched system in open loop control are derived under a simplified assumption. As listed in Table 2.2, for the dimensionless switching frequency  $\eta_{sw}$  in Eq. (2.22),

$$\eta_{sw} \gg \eta_d \quad \Rightarrow \quad T_{sw} \ll \frac{2\pi}{\Omega} < \frac{2\pi}{\omega_0} \quad (2.23)$$

holds. The constant switching period  $T_{sw} = T_1 + T_2$  and the constant time periods  $T_1, T_2$  are described by three arbitrary switching time instants  $t_{sw,2j}$ ,  $t_{sw,2j+1}$  and  $t_{sw,2j+2}$  ( $j = 0, 1, 2, \dots$ ), so  $T_{sw} = t_{sw,2j+2} - t_{sw,2j}$ ,  $T_1 = t_{sw,2j+1} - t_{sw,2j}$  and  $T_2 = t_{sw,2j+2} - t_{sw,2j+1}$ , here  $j$  represents the  $j$ -th switching period. Due to  $T_{sw}$  and also  $T_1$  and  $T_2$  being short enough compared to systems dynamic and the velocity varying continuously as well, shown in Fig. 2.5(e), the relationships for the average velocity  $\bar{x}_1$  of the payload over the time phases  $[t_{sw,2j}, t_{sw,2j+1}]$  and  $[t_{sw,2j+1}, t_{sw,2j+2}]$ , and the deformation rates of two springs can be approximately given by

$$\bar{x}_1(t, T_1) \approx \bar{x}_1(t, T_2), \quad \Rightarrow \quad \bar{u}_1(t, T_1) \approx \bar{u}_2(t, T_2) \quad (2.24)$$

together with Eq. (2.13) and Eq. (2.15). The incremental deformation of spring 1,  $\Delta u_1$  and that of spring 2,  $\Delta u_2$  over the above corresponding time phases are given by

$$\Delta u_1(t, T_1) = \bar{u}_1(t, T_1)T_1 = \bar{u}_1(t, T_1)D_{k1}T_{sw}, \quad (2.25)$$

and

$$\Delta u_2(t, T_2) = \bar{u}_2(t, T_2)T_2 = \bar{u}_2(t, T_2)(1 - D_{k1})T_{sw}, \quad (2.26)$$

with  $T_2 = T_{sw} - T_1$  and Eq. (2.20). Because spring 1 is only active over  $t \in [t_{sw,2j}, t_{sw,2j+1}]$  and spring 2 over  $t \in [t_{sw,2j+1}, t_{sw,2j+2}]$ ,  $\Delta u_1$  and  $\Delta u_2$  over  $t \in [t_{sw,2j}, t_{sw,2j+2}]$ , namely, one complete switching period  $T_{sw}$ , can be expressed by

$$\Delta u_1(t, T_{sw}) = \Delta u_1(t, T_1), \quad \Delta u_2(t, T_{sw}) = \Delta u_2(t, T_2). \quad (2.27)$$

If  $T_{\text{sw}}$  is infinitely low,  $\Delta u_1$  and  $\Delta u_2$  at an arbitrary time moment  $t$  can be given by

$$\lim_{T_{\text{sw}} \rightarrow 0} \Delta u_1(t, T_{\text{sw}}) = \Delta u_1(t), \quad \lim_{T_{\text{sw}} \rightarrow 0} \Delta u_2(t, T_{\text{sw}}) = \Delta u_2(t). \quad (2.28)$$

With the combination of Eq. (2.27), subsequently inserting Eq. (2.24)-Eq. (2.25), rearranging the variables and applying Eq. (2.27) and Eq. (2.28) derives the relationship between the deformation differences of the two springs at an arbitrary moment

$$\Delta u_1(t) = \frac{D_{k1}}{1 - D_{k1}} \Delta u_2(t). \quad (2.29)$$

If the initial deformations  $u_1(0) = u_2(0) = 0$  are taken into consideration, the relationship between the deformations  $u_1(t)$  and  $u_2(t)$  of the two springs can be given by

$$u_1(t) = \frac{D_{k1}}{1 - D_{k1}} u_2(t). \quad (2.30)$$

The coefficient of Eq. (2.30) agrees with the amplitude behavior of the springs deformations as shown in Fig. 2.5(c)-(d) quite well. In order to formulate the equivalent stiffness  $k_{\text{eq}}$  and natural frequency  $\omega_{\text{eq}}$  of the switched system, the energy method is applied now. The difference of potential energy  $\Delta E_p$  over  $T_{\text{sw}}$  is given by

$$\Delta E_p = \frac{1}{2} k [u_1^2(t_{\text{sw}, 2j+2}) - u_1^2(t_{\text{sw}, 2j}) + u_2^2(t_{\text{sw}, 2j+2}) - u_2^2(t_{\text{sw}, 2j})]. \quad (2.31)$$

A SDOF system  $m\ddot{x} + k_{\text{eq}}x = 0$ , having equivalent stiffness  $k_{\text{eq}}$  with potential energy difference  $\Delta E_{\text{peq}}$  and equivalent to the switched system, is looked for

$$\Delta E_{\text{peq}} = \frac{1}{2} k_{\text{eq}} [x^2(t_{\text{sw}, 2j+2}) - x^2(t_{\text{sw}, 2j})], \quad (2.32)$$

and matches the following conditions

$$\Delta E_{\text{peq}} = \Delta E_p, \quad x(t_{\text{sw}, 2j}) = u_1(t_{\text{sw}, 2j}) + u_2(t_{\text{sw}, 2j}), \quad x(t_{\text{sw}, 2j+2}) = u_1(t_{\text{sw}, 2j+2}) + u_2(t_{\text{sw}, 2j+2}). \quad (2.33)$$

Inserting Eqs. (2.30)-(2.32) into Eq. (2.33) leads to the equivalent stiffness

$$\frac{k_{\text{eq}}}{k} = 2D_{k1}^2 - 2D_{k1} + 1 \quad (2.34)$$

and the equivalent natural frequency

$$\frac{\omega_{\text{eq}}}{\omega_0} = \sqrt{2D_{k1}^2 - 2D_{k1} + 1}, \quad \omega_{\text{eq}} = \sqrt{\frac{k_{\text{eq}}}{m_1}}, \quad T_{\text{eq}} = \frac{2\pi}{\omega_{\text{eq}}}. \quad (2.35)$$

According to Eq. (2.34)-(2.35), the equivalent stiffness and natural frequency of this switched system for open loop control can be depicted in Fig. 2.6. This analytical approximation also matches the above numerical simulation results in terms of the equivalent natural frequency  $\omega_{\text{eq}}$ . To further validate the above stated conclusion, the spectral analysis for the displacement response under different duty cycles  $D_{k1}$  in an interval of 0.05 from 0 to 1 is carried out through Fast Fourier Transformation (FFT). On the basis of the amplitude-frequency spectrum property, the lowest frequency cor-

responding to the highest amplitude is the equivalent natural frequency of the switched system. The calculated frequency results are normalized by  $\omega_0$  and shown with the gray points in Fig. 2.6. It is obvious to find that the spectrum analysis and the mathe-

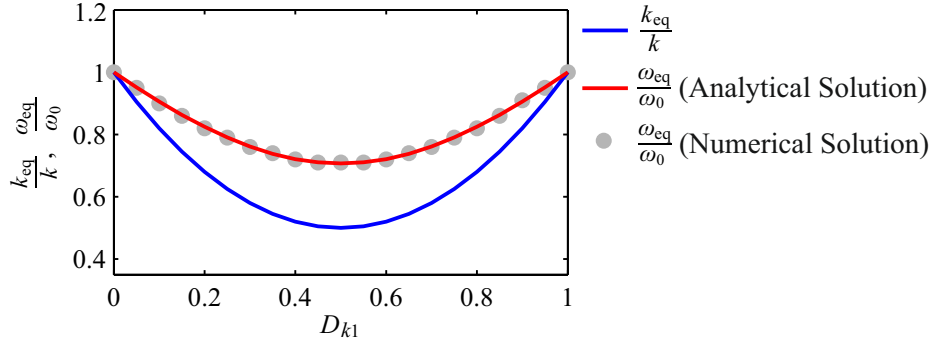


Figure 2.6.: The equivalent stiffness and natural frequency of 4S.

matical formulation also agree well. As shown in Fig. 2.6, the profiles of the equivalent stiffness and natural frequency are similar. When  $D_{k1} = 0$  and  $D_{k1} = 1$ , only one spring is active in 4S and the system works as a passive undamped system having the equivalent stiffness  $k_{eq} = k$  and the equivalent natural frequency  $\omega_{eq} = \omega_0$ . In all other cases it is a semi-active system and  $k_{eq}$  and  $\omega_{eq}$  change parabolically with the increase of  $D_{k1}$ . In the minimum at  $D_{k1} = 0.5$ ,  $k_{eq} = 0.5k$  and  $\omega_{eq} = \sqrt{2}\omega_0/2$ . This means that at an equal switching time period of two serial springs,  $T_1 = T_2$ , and  $\eta_{sw} \gg 1$ , the system behaves like a linear SDOF system.

## 2.4. Closed Loop Control for 4S

### 2.4.1. Switching Law based on Vibration Energy Harvesting

In order to realize vibration energy harvesting performance through vibration reduction, 4S is now analyzed in closed loop control based on the idea already outlined in Subsection 2.2.2 together with Fig. 2.3. Finally, the switching law can be given by

$$\mathbf{S}(t) = \begin{cases} [1, 0] & \text{if } \dot{x}_1 \geq 0 \\ [0, 1] & \text{if } \dot{x}_1 < 0 \end{cases} . \quad (2.36)$$

Inserting Eq. (2.36) into Eq. (2.16) gives the process force  $F_p$

$$F_p = \begin{cases} k u_2(t_{sw,i}) & \text{if } \dot{x}_1 \geq 0 \\ k u_1(t_{sw,i}) & \text{if } \dot{x}_1 < 0 \end{cases} , \quad (2.37)$$

for the closed loop controlled 4S. This switching law ensures that for all time instants the conditions  $u_1 > 0$  and  $u_2 < 0$  are valid. This switching between two springs is ideal. To consider a physically realizable zero-crossing detection and prevent chattering

a switching system, the switching law is slightly modified as

$$\mathbf{S}(t) = \begin{cases} [1, 0] & \text{if } \dot{x}_{1z} \geq 0 \\ [0, 1] & \text{if } \dot{x}_{1z} < 0 \end{cases}, \quad (2.38)$$

with the use of the zero-order-hold function of velocity, written as

$$\dot{x}_{1z}(\dot{x}_1, T_s) = \sum_{n=0}^{\infty} \dot{x}_1(nT_s) [\sigma(t - nT_s) - \sigma(t - (n+1)T_s)], \quad n \in \mathbb{N}, \quad (2.39)$$

or as

$$\dot{x}_{1z}(t, T_s) = \dot{x}_1(nT_s), \quad n \in \mathbb{N}, \quad nT_s \leq t < (n+1)T_s, \quad (2.40)$$

where  $T_s$  is the sampling period of the system, and  $\sigma(t)$  is the unit step function. Note that  $T_s$  is different from the aforementioned switching period  $T_{sw}$ . The former,  $T_s$ , is the minimal time interval, where the stiffness state is constant, but the latter,  $T_{sw}$ , is constant and is the minimal time interval, where two switching instants can occur. Thus, for a general switching time span  $T_{sw,j}$  ( $j = 0, 1, 2, \dots$ ), not similar to a regular switching in an open loop control, it may be variable, namely,  $T_{sw,j} \geq 2T_s$ , where  $j$  represents the  $j$ -th complete stiffness switching in 4S. Therefore, the relationship between the switching rate  $\Omega_{sw,j}$  and the sampling frequency  $\omega_s$  can be given by

$$\Omega_{sw,j} \leq \frac{1}{2}\omega_s, \quad \Omega_{sw,j} = \frac{2\pi}{T_{sw,j}}. \quad (2.41)$$

One case for the signal discretization is graphically shown in Fig. 2.7, where  $T_{s1} > T_{s2} > T_{s3}$ . It obviously reveals that the lower the sampling period, the more the discretized signal represents the original one. The discretization process for velocity results in a nonideal switching and produces switching delay. As an example, it is

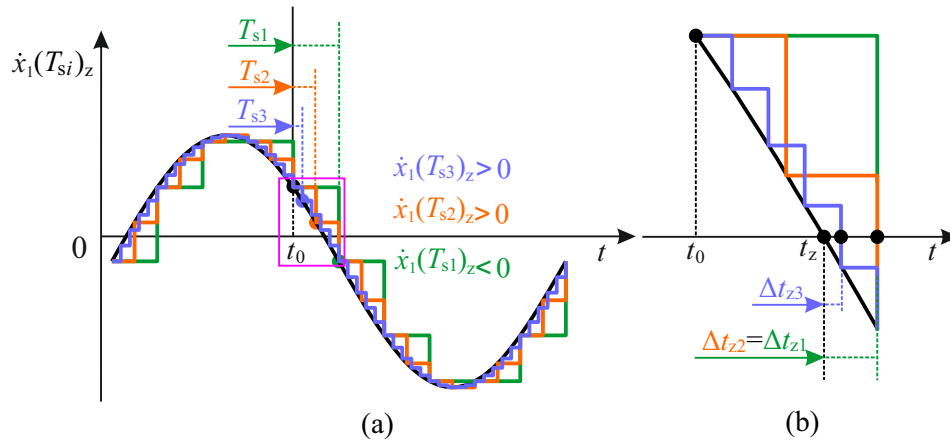


Figure 2.7.: Switching decision error for 4S with different sampling period  $T_s$ : (b) is a partly zoomed-in picture for (a). Black: original signal; Green: discretized signal with sampling period  $T_{s1}$ ; Orange: discretized signal with sampling period  $T_{s2}$ ; Blue: discretized signal with sampling period  $T_{s3}$ .

assumed that for three systems with different sampling time  $T_{s1}$ ,  $T_{s2}$  and  $T_{s3}$  and their velocity controllers start to process at a common time point  $t_0$  and they own a

common output at this moment. After one sampling period, different systems have different discretized outputs,  $\dot{x}_1(t, T_s)_z$ , according to Eq. (4.29). Here  $\dot{x}_1(t, T_{s2})_z > 0$ ,  $\dot{x}_1(t, T_{s3})_z > 0$ , but  $\dot{x}_1(t, T_{s1})_z < 0$ . Fig. 2.7(b) shows the switching decision error, which is a partly zoomed-in picture marked by a pink frame in Fig. 2.7(a). Here  $t_z$  is an ideal velocity zero-crossing moment. For 4S different sampling periods  $T_{si}$  result in different switching decision errors  $\Delta t_{zi}$ , as an example,  $\Delta t_{z1} = \Delta t_{z2} > \Delta t_{z3}$  here. As a result, 4S would operate in different stiffness states after the ideal zero-crossing moment  $t_z$ . This will further affect the system response.

## 2.4.2. System Dynamics

Based on the above switching law and discretization principle, the lumped control system dynamics can be written by

$$\begin{aligned} m_1 \ddot{x}_1 + kx_1 &= F + F_p(x_1, x_2, \dot{x}_1, T_s), \\ x_2 &= \begin{cases} x_2(t_{sw,i}) & \text{if } \dot{x}_{1z}(\dot{x}_1, T_s) \geq 0 \\ x_1 - [x_1(t_{sw,i}) - x_2(t_{sw,i})] & \text{if } \dot{x}_{1z}(\dot{x}_1, T_s) < 0 \end{cases}, \end{aligned} \quad (2.42)$$

with the process force  $F_p$  in Eq. (2.37)

$$F_p(x_1, x_2, \dot{x}_1, T_s) = \begin{cases} k u_2(t_{sw,i}) & \text{if } \dot{x}_{1z}(\dot{x}_1, T_s) \geq 0 \\ k u_1(t_{sw,i}) & \text{if } \dot{x}_{1z}(\dot{x}_1, T_s) < 0 \end{cases}, \quad (2.43)$$

with the zero-order-hold function of velocity

$$\dot{x}_{1z}(\dot{x}_1, T_s) = \sum_{n=0}^{\infty} \dot{x}_1(nT_s) [\sigma(t - nT_s) - \sigma(t - (n+1)T_s)], \quad n \in \mathbb{N}, \quad (2.44)$$

or

$$\dot{x}_{1z}(t, T_s) = \dot{x}_1(nT_s), \quad n \in \mathbb{N}, \quad nT_s \leq t < (n+1)T_s, \quad (2.45)$$

and the deformations of the two springs

$$u_1 := x_1 - x_2, \quad u_2 := x_2. \quad (2.46)$$

This is a nonlinear differential equation system, where the process force  $F_p$  contains a nonlinear term and is governed by the sampling period  $T_s$  as a process parameter. A graphical interpretation of this semi-active switching system is simplified in Fig. 2.8(a), which shows that the process force  $F_p$  can be interpreted as an active force on the payload. The actual spring forces  $F_k$  are derived from Eq. (2.17) and result in

$$F_k = kx_1 - F_p(x_1, x_2, \dot{x}_1, T_s), \quad (2.47)$$

with the time varying part  $kx_1$  and the piecewise constant part  $F_p$ .  $F_k$  and  $F_p$  for a harmonic oscillation are graphically depicted in Fig. 2.8(b) and (c). The spring force components  $F_{k1}$  and  $F_{k2}$  are piecewise constant owing to the switching between two springs.  $F_p$  is only mathematically defined and varies at the switching moments and then acts on a payload with a constant value during each switching state, denoted by blue line,  $F_{p1}$ , and green line,  $F_{p2}$ , in Fig. 2.8(b). So the resultant process force

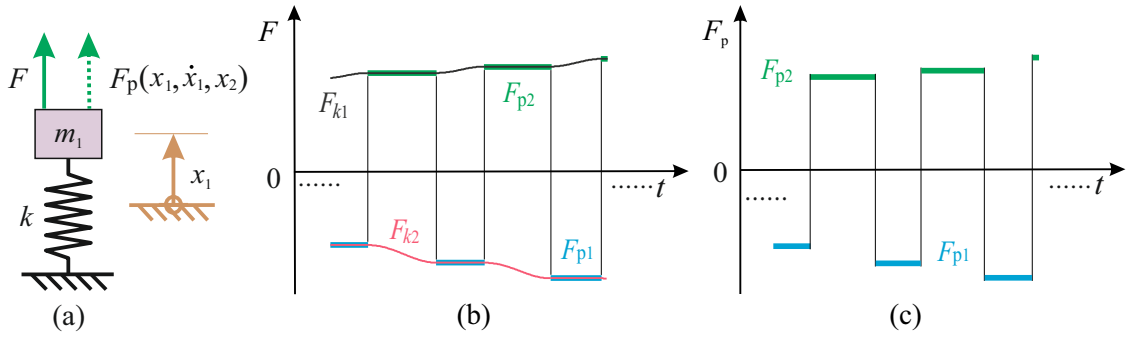


Figure 2.8.: Simplified representation for 4S and force components: (a) Simplified 4S model; (b) Force components:  $F_{k1}$  — spring force 1,  $F_{k2}$  — spring force 2,  $F_{p1}$  — process force 1,  $F_{p2}$  — process force 2; (c) Resultant process force  $F_p$ .

$F_p$  shows a positive and negative pulse-like increasing in Fig. 2.8(c). For the system analysis the resultant force  $F_{res}$ , as the combination of the external disturbance  $F$  and the actual spring force  $F_k$

$$F_{res} = F - F_k \quad (2.48)$$

is considered. Multiplying Eq. (2.48) with the velocity  $\dot{x}_1$ , the mechanical power balance can be given by

$$P_{res} = P_F - P_k. \quad (2.49)$$

In Subsection 2.2.2 the changing rate of potential energy was assumed to be positive in all time instants. This is equivalent to the instantaneous power  $P_k$  into the springs as given by

$$P_k = \frac{dU}{dt} = F_k \dot{x}_1 = [kx_1\dot{x}_1 - F_p(x_1, x_2, \dot{x}_1, T_s)\dot{x}_1] \geq 0. \quad (2.50)$$

according to Eq. (2.47).

### 2.4.3. Numerical Analysis

In order to explain how 4S operates in closed loop control, a numerical simulation is executed in MATLAB/Simulink. The block diagram for the new semi-active vibration control system is depicted in Fig. 2.9. The switches  $s_1$  and  $s_2$  in the Mechanical Unit are controlled using the sign of the step-wise discretized velocity  $\dot{x}_{1z}$  of the payload  $m_1$ . All parameters for numerical analysis are listed in Table 2.3. Apart from the dimensionless

Table 2.3.: Simulation parameters for 4S in closed loop control.

Name	Value	Unit	Name	Value	Unit	Name	Value	Unit
$\hat{F}$	1	N	$\eta_d$	10	-	$x_1(0)$	0	m
$m_1$	1	kg	$\eta_s$	1000	-	$x_2(0)$	0	m
$k$	1	N/m				$\dot{x}_1(0)$	0	m/s

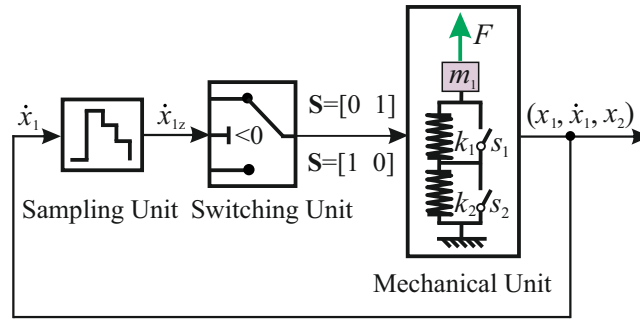


Figure 2.9.: Schematic for 4S in closed loop control

disturbance frequency  $\eta_d$ , defined in Eq. (2.22), the dimensionless sampling frequency  $\eta_s$ , is used here

$$\eta_s = \frac{\omega_s}{\omega_0}, \quad \omega_s = \frac{2\pi}{T_s}, \quad (2.51)$$

together with the sampling frequency  $\omega_s$ . 4S is excited by the harmonic disturbance according to Eq. (2.18). For a passive undamped system,  $m_1\ddot{x}_1 + kx_1 = \hat{F} \sin \Omega t$ , the solution is  $x_1(t) = \hat{x}_{1h} \sin(\omega_0 t + \varphi) + \hat{x}_{1p} \sin(\Omega t)$  with an initial phase angle  $\varphi$  and the displacement amplitude  $\hat{x}_1$  consists of the homogeneous displacement amplitude  $\hat{x}_{1h}$  and the particular displacement amplitude  $\hat{x}_{1p}$  given by

$$\hat{x}_{1h} = \frac{\hat{F}}{k} \frac{\eta_d}{1 - \eta_d^2}, \quad \hat{x}_{1p} = \frac{\hat{F}}{k} \frac{1}{1 - \eta_d^2}. \quad (2.52)$$

With the simulation parameters according to Table 2.3, this leads to a displacement amplitude of  $\hat{x}_1 \approx 11$  cm. The simulation results are shown in Fig. 2.10 and Fig. 2.11. One the basis of different qualitative behaviors all plotting curves in Fig. 2.10 are divided into four time phases and symbolized by A, B, C and D, respectively. Additionally, zoom-in pictures a, b, c and d are labeled in Fig. 2.10 and the zoom-in pictures are plotted in Fig. 2.11, where the switching sequence between two springs is shown by the colorful backgrounds. In all subfigures, the horizontal axes stand for the simulation time and the vertical axes represent different system response parameters including the displacement and velocity of payload  $x_1$  and  $\dot{x}_1$ , the deformations of two springs  $u_1$  and  $u_2$  and so on. In order to better evaluate the performance of 4S, a passive undamped system is taken into consideration and the system response at beginning chosen by orange frame in the right side subfigures are also amplified in the left side ones of Fig. 2.10.

Fig. 2.10(a)-(b) show the displacement response. It is known that a passive undamped  $m_1$ - $k$  system response does not decay and always oscillates. For the closed loop controlled 4S, the displacement decays fast but not asymptotically like in a passive damped system. After the disturbance vibrations have been reduced, the payload oscillates with a low amplitude ( $\hat{x}_1 \approx 1$  cm), according to Fig. 2.11 around an equilibrium position. Naturally, 4S shows a better vibration reduction performance than a passive undamped system based on Eq. (2.52). As mentioned before, the power of spring forces,  $P_k$ , expressed in Eq. (2.50), acting on payload is always positive and the potential energy, hence, always increases and is stored in two springs. So the deformations of the two



springs  $u_1$  and  $u_2$  will always increase in contrary directions as depicted in Fig. 2.10(c)-(f). This means that one spring is extended and the other compressed. Similar to the displacement response, the velocity also decays and finally oscillates around an equilibrium position, as shown in Fig. 2.10(g)-(h). The payload chatters around the equilibrium position, which is one common phenomenon existing in a switching system.

The force components acting on the payload are shown in Fig. 2.10(i)-(j). Compared to the spring force of a passive undamped system plotted by the black line,  $F_k$  of 4S increases pulse-wise due to the alternating switching between two springs. As described in Fig. 2.10(j), the actual spring force  $F_k$  always increases and becomes even larger than the external disturbance  $F$  after a sufficient amount of time. The resultant force  $F_{\text{res}}$  on the payload changes significantly and its amplitude rises with the increase of  $F_k$ .

Fig. 2.10(k) shows that the mechanical power into the springs is always positive, while in a passive undamped system its sign changes. Positive power means the potential energy of the spring increases. Fig. 2.10(l) shows the moving average value of three powers, the power  $\bar{P}_{\text{res}}$  of the resultant force  $F_{\text{res}}$  in Eq. (2.48) acting on the payload, the power  $\bar{P}_k$  of spring force  $F_k$  in Eq. (2.47) and the power  $\bar{P}_F$  of the external disturbance  $F$ . A moving average filter is applied to calculate the power over 6.283 s, because the chattering results in strong oscillations at high frequency and this causes a bad readability. As shown in Fig. 2.10(l),  $\bar{P}_k$  is always positive, which means that potential energy is always stored in the system.  $\bar{P}_F$  and  $\bar{P}_k$  are approximately equal, so the resultant power  $\bar{P}_{\text{res}}$  is close to zero according to Eq. (2.49) and the kinetic energy of the payload will remain near zero. Consequently, the payload will stay near an equilibrium position.

The detailed information about switching is shown in Fig. 2.11. It is obvious to find that 4S switches more and more frequently with the increase of time  $t$ , which can be demonstrated by a more and more densely varying colorful background, where blue and green areas stand for switching states  $\mathbf{S} = [1, 0]$  and  $\mathbf{S} = [0, 1]$ , respectively. At the beginning in section A, marked in Fig. 2.10(a), the springs have not stored much potential energy. Therefore, the external disturbance  $F$  dominates the system response. This results in a slow switching depending on the disturbance frequency. As mentioned before, the zero-order-hold function, as shown in Fig. 2.7, causes a nonideal switching. When the zero-crossing frequently happens due to the enough largely stored potential energy, the actual switching would be delayed till the end of a sampling period. As a result, the kinetic energy of the payload is not zero any more but increases till the end of the sampling period. Meanwhile, the newly stored potential energy decreases in the sampling period. Finally, the deformations of two springs might decrease, not continuously increase any more, denoted by  $u_1$  and  $u_2$ . Whether or not the potential energy will be continuously stored depends on the ratio of the ideally and delayed switching state. There are some sampling periods where the potential energy is reduced and the other increased, but the sum of potential energy over many sampling periods still increases as shown in the subfigures of Fig. 2.10(d) and (f) with respect to the spring deformations  $u_1$  and  $u_2$ . Thus, the spring deformations and spring forces still increase over time and even larger than the disturbance force in Fig. 2.10(j). This causes the direction of velocity to vary rapidly, and then fast switching occurs. Finally, the two springs are extremely frequently connected to system alternatively. This will need a high dynamic mechanical switch, namely, clamping device to finish the

connection or disconnection of two springs to or away from payload, which should be taken good care. It is important to note that if the steadily increasing potential energy becomes too large, it can be released by using 4S as an actuator or by opening both switches at once. In practice there is energy dissipation mechanism which removes potential energy from the springs when both switches are opened at once, which is similar to that in Fig. 2.2(a)-(b). The small damping can be neglected for system dynamics analysis in Fig. 2.2(a) but can not be neglected for the vibration energy dissipation analysis in Fig. 2.2(b).

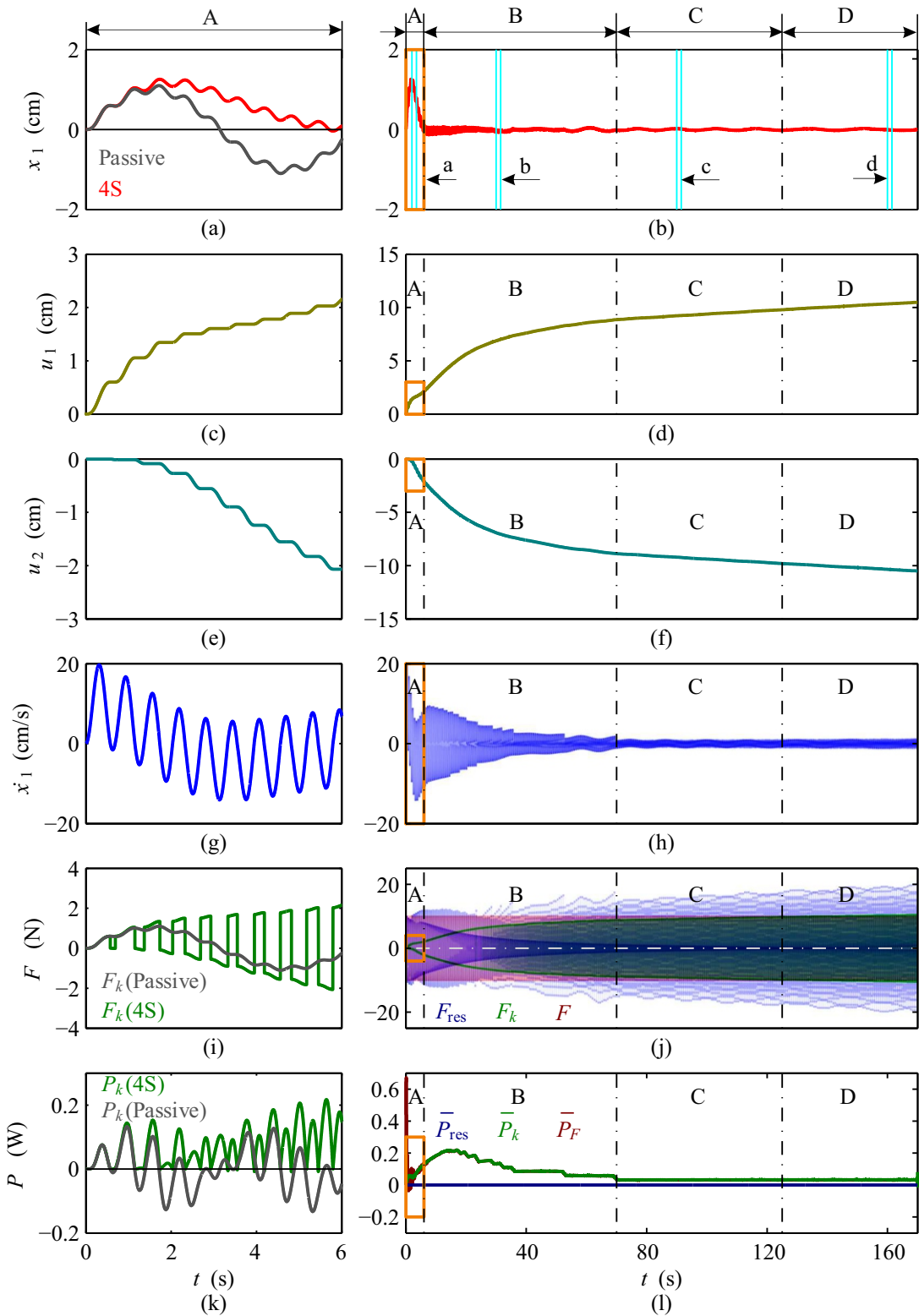


Figure 2.10.: Representation for system response for a short and a long time. (a) and (b): Displacement response; (c) and (d): Deformation of spring 1; (e) and (f): Deformation of spring 2; (g) and (h): Velocity response; (i) and (j): Force response,  $F_k$  — spring force,  $F$  — disturbance,  $F_{\text{res}}$  — resultant force; (k) and (l) Power response,  $P_k$  — power of spring force,  $\overline{P}_k$  — moving average power of spring force,  $\overline{P}_F$  — moving average power of disturbance,  $\overline{P}_{\text{res}}$  — moving average resultant power

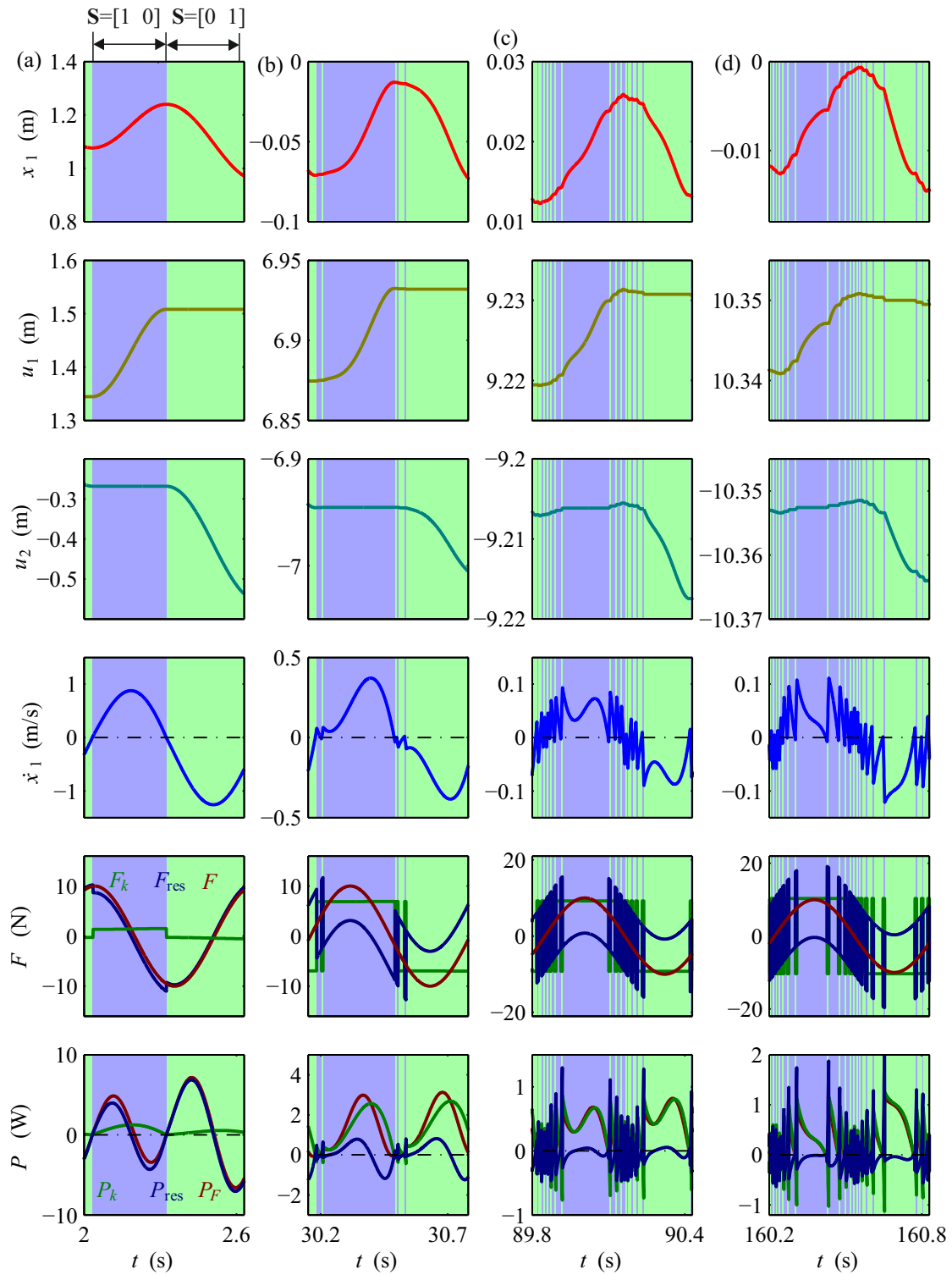


Figure 2.11.: Partly magnified representation for system response from time phase A to time phase D. Column (a): System response during time phase A; Column (b): System response during time phase B; Column (c): System response during time phase C; Column (d): System response during time phase D

---

## Vibration Energy Harvesting Limit Analysis

---

### 3.1. Introduction

From Fig. 2.10(d) and (f) in the last chapter, it seems that the deformations of two springs always increase. This means the potential energy will be always stored in system, as long as two springs are within their limits of strength. Whether or not the potential energy is always stored in 4S under a harmonic forced excitation will be discussed in this chapter.

Firstly, the spectrum analysis for system response under different stored potential energy levels is carried out to validate the existence of vibration energy harvesting limit. Following are the system dynamics analysis with respect to process force  $F_p$  and the analytical solution for the steady state system response. Finally, the vibration energy harvesting limit is analytically formulated and the numerical validation is also executed.

### 3.2. Spectrum Analysis for System Response

Fig. 2.11 shows that the switching between two springs occurs more and more frequently with an increase of the stored potential energy. Whether the phenomena of the switching with the maximum frequency, will happen depends on the stored potential energy level, denoted by  $u_1$  or  $u_2$ ,  $u_1 = -u_2$ . If it happens, what does the displacement response  $x_1$  look like? In order to provide a clear and concise interpretation, spectrum analysis by means of Fast Fourier Transformation (FFT) is performed for different potential energy pre-storage in 4S, namely,  $u_1(0)$  or  $u_2(0)$ ,  $u_1(0) = -u_2(0) \neq 0$ . According to Eq. (2.13), a nonzero potential energy pre-storage  $u_2(0)$  means a nonzero initial state variable  $x_2(0)$ , here  $x_1(0) = 0$ . The model parameters are listed in Table 3.1

Table 3.1.: Simulation parameters for frequency spectrum.

Name	Value	Unit	Name	Value	Unit	Name	Value	Unit
$\hat{F}$	1	N	$\eta_d$	10	-	$x_1(0)$	0	m
$m_1$	1	kg	$\eta_s$	1000	-	$\dot{x}_1(0)$	0	m/s
$k$	1	N/m				$x_2(0)$	variable	m

and the spectrum analysis results are shown in Fig. 3.1. With the aim of obtaining a complete spectrum of the displacement response signal, the time domain response for each  $x_2(0)$  lasts for 1000 s based on simulation experience. Here the horizontal axis stands for  $x_2(0)$  with a logarithmic scale,  $x_2(0) \in [-1000, 1]$  and the vertical axis for the angular frequency  $\omega$ . The colorful background denotes the amplitude distribution corresponding to the displacement response for different  $x_2(0)$ .

On the basis of the amplitude-frequency distribution characteristics, three frequency domains, where a large amplitude appears, are marked by dot-dash lines A and B in subfigure (a) and further magnified as shown in subfigures (b)-(d). An obvious limit, marked by dot-dash line C in subfigure (a), divide the entire spectrum distribution  $\hat{x}_1$  at different  $x_2(0)$  into two parts. On the left side of the limit, the spectrum is not distributed orderly. This means that 4S does not switch periodically, namely, it stays in a transient state. On the right side, the spectrum is distributed orderly with three obvious frequency components. It is not difficult to see that these are the disturbance frequency  $\Omega = 10$  as listed in Table 3.1, the equivalent natural frequency of the switched system  $\omega_{eq} = 0.707$  according to Eq. (2.35), and the maximal switching frequency  $\Omega_{sw} = 500$ , according to Inequality (2.41). In these cases, on the right side of the limit, 4S realizes the fastest switching between two stiffness states and switches in every sampling period  $T_s$ . For the limit value of  $x_2(0)$ , marked by dot-dash line C,  $x_{2critical}$  is equal to  $-32.1524$  m. This means that if the stored potential energy, denoted by  $x_2$  according to Eq. (2.13), is larger than the value,  $|x_2| \geq |x_{2critical}|$ , the system goes into steady state response and the displacement response consists of a free response term, disturbance response term, and switching response or chattering term. In order to solve for the steady state response, the analytical formulation is executed in the following sections.

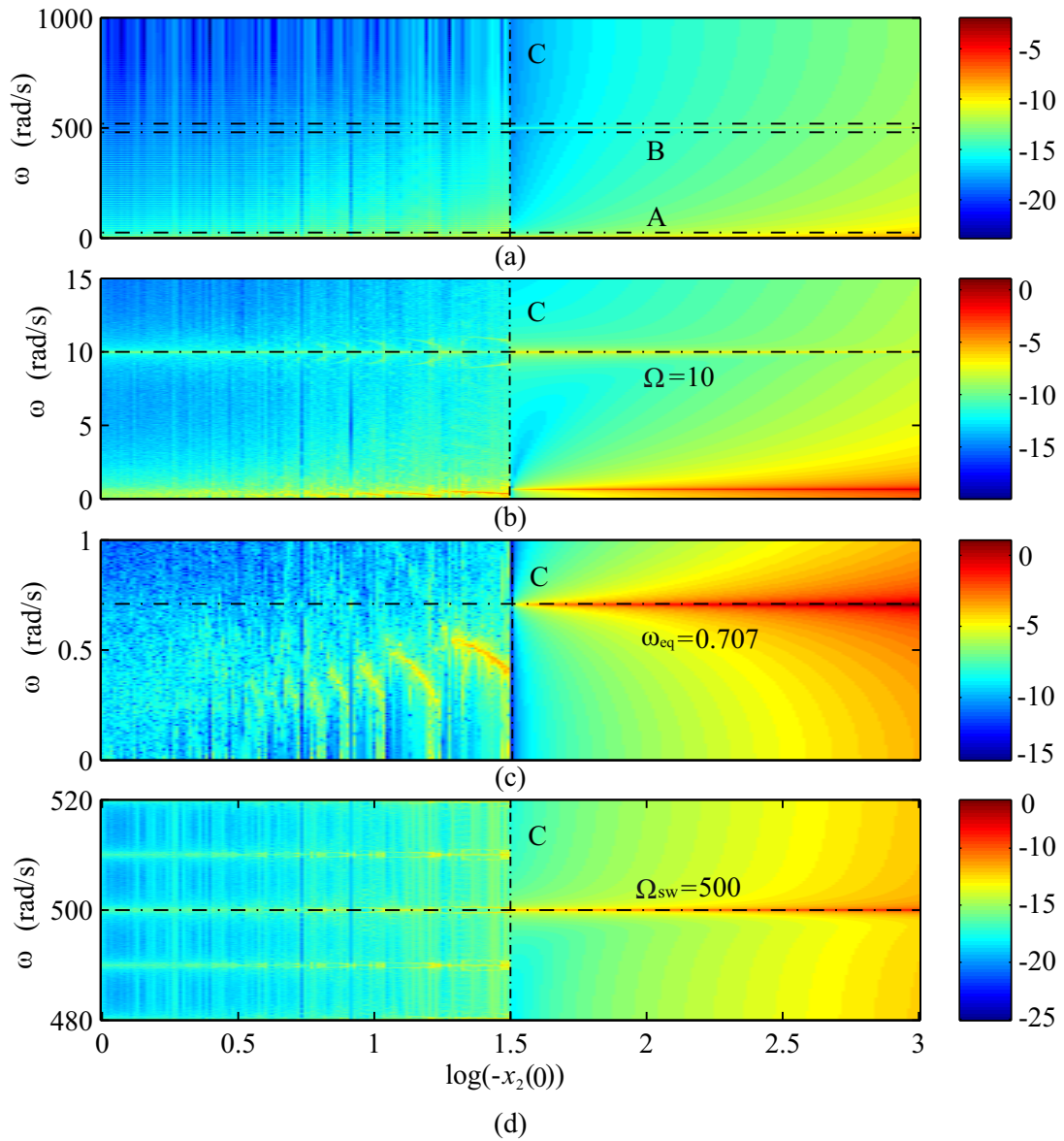


Figure 3.1.: Representation for spectrum analysis for different  $x_2(0)$ :  $\eta_d = 10$  and  $\eta_s = 1000$ . (a) Representation for the spectrum of the entire frequency domain; (b)-(d) Zoomed-in pictures for the partly magnified domains marked by dot-dash lines A and B in (a).

### 3.3. Steady State System Response

The objective in this section is to deliver an analytical solution for a steady-state system response of 4S with velocity switching law, (2.46)-(2.50), under harmonic forced excitation  $F(t)$ . The solution thought of is a steady-state chattering solution switching between both springs with the sampling frequency  $\omega_s$ . The system dynamics is given by two piecewise linear equations of motion as stated in (2.46)

$$m_1 \ddot{x}_1 + kx_1 = F + F_p(x_1, x_2, \dot{x}_1, T_s) . \quad (3.1)$$

Three different fundamental frequencies govern the dynamics of the system in the specific steady-state condition. The eigenfrequency  $\omega_0$  of each subsystem, the excitation frequency  $\Omega$  of the forced excitation due to  $F(t)$  and the stiffness switching frequency  $\Omega_{sw}$ . Due to the aforementioned assumption of chattering with the sampling frequency, the switching frequency is half of the sampling frequency  $\Omega_{sw} = \frac{1}{2}\omega_s$ . The way to come

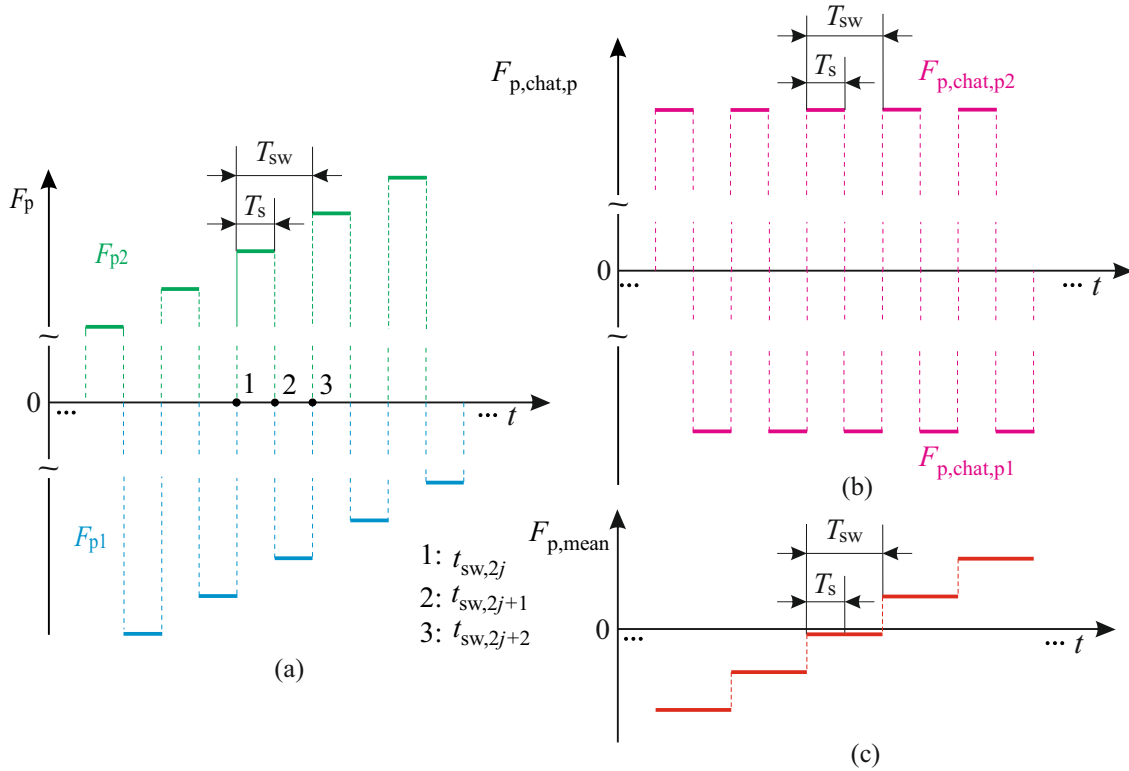


Figure 3.2.: Decomposition analysis for process force  $F_p$ . (a) Representation for  $F_p$ ; (b) Representation for  $F_{p,chat,p}$ ; (c) Representation for  $F_{p,mean}$ .

to an approximative analytical solution is divided into four steps. The first two steps treat the process force  $F_p$ . With the combination of Fig. 2.8(c),  $F_p$  can be split into two parts during the  $j$ -th switching time span  $T_{sw,j}$

$$F_p(t) = \begin{cases} F_{p1}(t_{sw,2j}) = ku_2(t_{sw,2j}) , & t_{sw,2j} \leq t \leq t_{sw,2j+1} \\ F_{p2}(t_{sw,2j+1}) = ku_1(t_{sw,2j+1}) , & t_{sw,2j+1} \leq t \leq t_{sw,2j+2} \end{cases} , \quad (3.2)$$



and

$$u_1 = x_1 - x_2, \quad u_2 = x_2 \quad (3.3)$$

where three adjacent switching time instants  $t_{sw,2j}$ ,  $t_{sw,2j+1}$  and  $t_{sw,2j+2}$  are chosen as shown in Fig. 3.3(a). According to Section 2.3.1 and Fig. 2.4,  $T_{1,j}$ ,  $T_{2,j}$  are the time spans, where spring 1 or spring 2 are active, respectively

$$T_{1,j} = t_{sw,2j+1} - t_{sw,2j}, \quad T_{2,j} = t_{sw,2j+2} - t_{sw,2j+1}. \quad (3.4)$$

The switching time span is the sum of the time spans of spring 1 and 2

$$T_{sw,j} = T_{1,j} + T_{2,j} = t_{sw,2j+2} - t_{sw,2j}, \quad j = 0, 1, 2, \dots \quad (3.5)$$

$u_2(t_{sw,2j})$ ,  $u_1(t_{sw,2j+1})$  are the deformations of the two springs at the switching time instants. It works as an active force on the payload  $m_1$  according to Eq. (2.42) and Fig. 2.8. It represents the piecewise constant parts  $F_{p1}$  and  $F_{p2}$  of the spring forces  $F_{k1}$  and  $F_{k2}$ , see 2.8(b). Numerical simulation results in Fig. 3.1 show, that the process force contains three fundamental frequencies, the high switching frequency  $\Omega_{sw}$  and the low eigenfrequencies  $\omega_{eq}$  and  $\Omega$ , respectively. This triggers the approach to divide the process force into two components

$$F_p = F_{p,mean} + F_{p,chat,p}, \quad (3.6)$$

where  $F_{p,mean}$  represents the step-like changing mean value and  $F_{p,chat,p}$  the periodic chattering part. Fig. 3.3(b) and (c) shows this decomposition. The high frequency component has the switching frequency  $\Omega_{sw}$  as its fundamental frequency and can be represented by a FOURIER series without mean value

$$F_{p,chat,p} = \sum_{n=1}^{\infty} C_n \cos n\Omega_{sw}t + S_n \sin n\Omega_{sw}t, \quad \text{with} \quad \Omega_{sw} = \frac{2n\pi t}{T_{sw}}, \quad (3.7)$$

and will be further defined as

$$F_{p,chat,p}(t) = \begin{cases} F_{p,chat,p1} = ku_{2s}, & t_{sw,2j} \leq t \leq t_{sw,2j+1} \\ F_{p,chat,p2} = ku_{1s}, & t_{sw,2j+1} \leq t \leq t_{sw,2j+2} \end{cases}, \quad (3.8)$$

where  $u_{1s}$  and  $u_{2s}$  represent a stored potential energy level with a fixed value,  $u_{1s} = -u_{2s}$ , unlike the deformations  $u_1$  and  $u_2$  with a variable level in different switching periods  $T_{sw,j}$  as shown in Fig. 3.3(a). The step-like changing mean value part  $F_{p,mean}$  can be obtained as the average over each switching time span

$$F_{p,mean,j} = \frac{1}{T_{sw}} \left( \int_{t_{sw,2j}}^{t_{sw,2j+1}} F_{p1}(t_{sw,2j}) dt + \int_{t_{sw,2j+1}}^{t_{sw,2j+2}} F_{p2}(t_{sw,2j+1}) dt \right), \quad t \in [t_{sw,2j}, t_{sw,2j+2}], \quad (3.9)$$

To solve  $F_{p,mean,j}$  the process force according to Eq. (3.2) and Eq. (3.3) is substituted into Eq. (3.9) and delivers

$$F_{p,mean,j} = \frac{1}{2} kx_1(t_{sw,2j+1}), \quad t \in [t_{sw,2j}, t_{sw,2j+2}]. \quad (3.10)$$

The combination of each part in one function gives the step-like changing mean value function

$$F_{p,\text{mean}} = \sum_{j=1}^{\infty} F_{p,\text{mean},j} [\sigma(t_{\text{sw},2j}) - \sigma(t_{\text{sw},2j+2})] \quad (3.11)$$

With this result, step one is finished.

In step two, the step-like changing mean value function  $F_{p,\text{mean}}$  is further decomposed into a low and high frequency component as shown in Fig. 3.3. The low frequency component  $F_{p,\text{low}}$  represents free and forced vibration as shown in Fig. 3.3(c) over a short time, and Fig. 3.3(d) depicts its time behavior over a long time, where the area chosen by a dotted frame is magnified in Fig. 3.3(c). The high frequency component  $F_{p,\text{chat,np}}$  belongs to the chattering, however it is non-periodic. Although it seems to be periodic in a short time as shown in Fig. 3.3(b), in fact it will slowly change with the time behavior of  $F_{p,\text{low}}$  in Fig. 3.3(d). Thus,  $F_{p,\text{mean}}$  in Eq. (3.11) can be decomposed

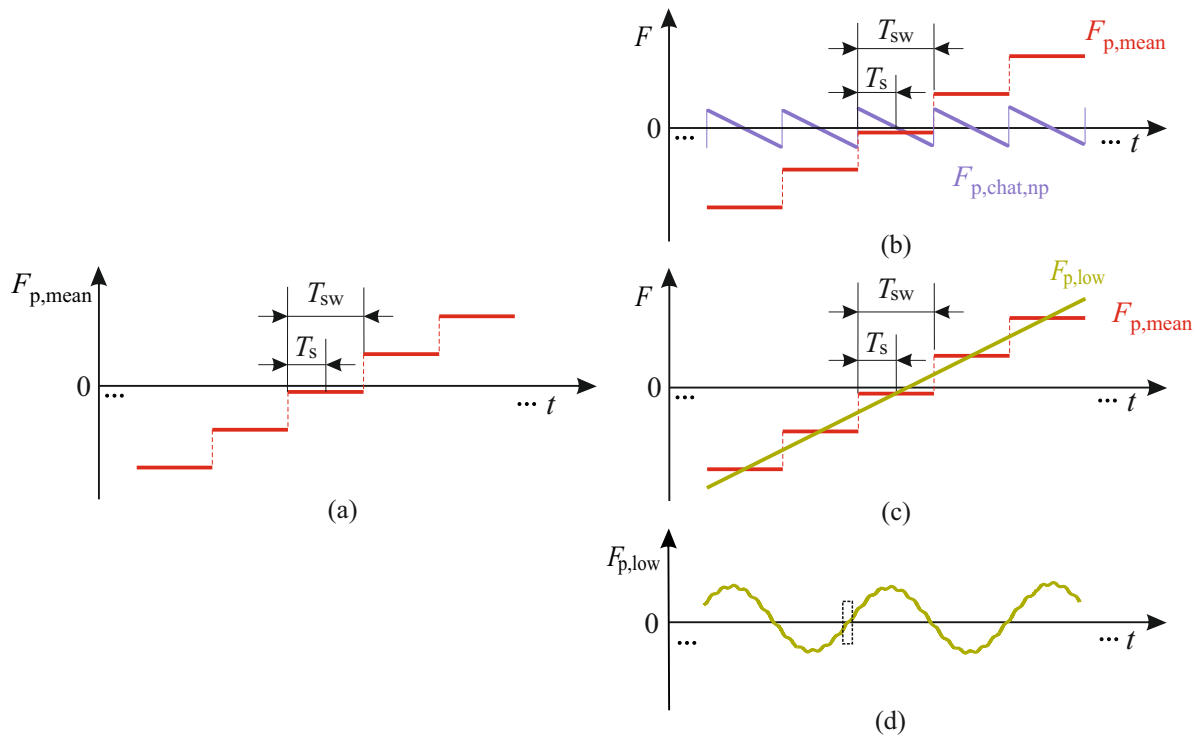


Figure 3.3.: Decomposition for the step-like changing mean value function  $F_{p,\text{mean}}$ . (a) Representation for  $F_{p,\text{mean}}$ ; (b) Representation for  $F_{p,\text{chat,np}}$ ; (c) Representation for  $F_{p,\text{low}}$ ; (d) The time behavior of  $F_{p,\text{low}}$  for a long time.

into

$$F_{p,\text{mean}} = F_{p,\text{low}} + F_{p,\text{chat,np}} , \quad (3.12)$$

such that  $F_{p,\text{low}}$  can be written as

$$F_{p,\text{low}} = \frac{1}{2} k x_1 . \quad (3.13)$$

With the combination of the first step results, the final decomposition for the process

force  $F_p$  can be given by

$$F_p = F_{p,\text{low}} + F_{p,\text{chat,np}} + F_{p,\text{chat,p}} . \quad (3.14)$$

Inserting Eq. (3.14) into Eq. (3.1), subtracting the term  $F_{p,\text{low}}$ , the system dynamics are modified to

$$m_1 \ddot{x}_1 + k_{\text{eq}} x_1 = F + F_{p,\text{chat,np}} + F_{p,\text{chat,p}} , \quad (3.15)$$

where

$$k_{\text{eq}} = \frac{1}{2}k , \quad \omega_{\text{eq}} = \frac{\sqrt{2}}{2}\omega_0 . \quad (3.16)$$

Compared to the system dynamics given by Eq. (2.42) and Eq. (2.43), Eq. (3.15) shows 4S in steady state can be taken as an equivalent linear system with a natural frequency  $\omega_{\text{eq}}$ , suffering from an external disturbance  $F$  and chattering disturbance,  $F_{p,\text{chat,np}}$  and  $F_{p,\text{chat,p}}$ .  $F_{p,\text{chat,np}}$  is non-periodic, but owns a low amplitude and high switching frequency  $\Omega_{\text{sw}}$ , whose output response can be neglected based on a low-pass filtering property of the left side of Eq. (3.15).  $F_{p,\text{chat,p}}$  is periodic with a very large amplitude,  $u_{1s} = -u_{2s}$ , and the same high frequency  $\Omega_{\text{sw}}$ . Accordingly, the general solution  $x_1(t)$  for steady state response based on Eq. (3.15) can be given by

$$x_1(t) = x_{1h}(t) + x_{1F}(t) + x_{1Fp,\text{chat,p}}(t) , \quad (3.17)$$

where the term  $x_{1h}(t)$  is the homogeneous solution, the other two terms  $x_{1F}(t)$  and  $x_{1Fp,\text{chat,p}}(t)$  are the particular solutions related to the external disturbance  $F$  and the periodic chattering part  $F_{p,\text{chat,p}}$ , respectively.

4S in steady state is identical to an open loop control with a duty cycle  $D_{k1}$  of 0.5 as mentioned in Subsection 2.3. Therein, low dynamic with respect to free and disturbance response components uses two equal springs resulting in an equivalent stiffness  $k_{\text{eq}}$ . High frequency chattering uses only a single spring within one sampling period  $T_s$ , which is related to each subsystem with natural frequency  $\omega_0$ . Therefore, the high frequency chattering term  $x_{1Fp,\text{chat,p}}(t)$  with respect to  $\omega_0$  will be solved, but the low frequency terms  $x_{1h}(t)$  and  $x_{1F}(t)$  will be considered at an equivalent natural frequency  $\omega_{\text{eq}}$ . Due to  $F_{p,\text{chat,p}}$  being split into two parts according to Eq. (3.8), the particular solution  $x_{1Fp,\text{chat,p}}(t)$  can be expressed by

$$x_{1Fp,\text{chat,p}}(t) = \begin{cases} x_{11Fp,\text{chat,p}}(t), & t_{\text{sw},2j} \leq t < t_{\text{sw},2j+1} \\ x_{12Fp,\text{chat,p}}(t), & t_{\text{sw},2j+1} \leq t \leq t_{\text{sw},2j+2} \end{cases} , \quad (3.18)$$

and

$$x_{11Fp,\text{chat,p}}(t) = K_1 \cos[\omega_0(t - t_{\text{sw},2j})] + K_2 \sin[\omega_0(t - t_{\text{sw},2j})] + u_{2s} , \quad (3.19)$$

$$x_{12Fp,\text{chat,p}}(t) = K_3 \cos[\omega_0(t - t_{\text{sw},2j+1})] + K_4 \sin[\omega_0(t - t_{\text{sw},2j+1})] + u_{1s} . \quad (3.20)$$

The transition conditions

$$x_{11Fp,\text{chat,p}}(t_{\text{sw},2j}) = x_{12Fp,\text{chat,p}}(t_{\text{sw},2j+2}) , \quad x_{11Fp,\text{chat,p}}(t_{\text{sw},2j+1}) = x_{12Fp,\text{chat,p}}(t_{\text{sw},2j+1}) , \quad (3.21)$$

$$\dot{x}_{11Fp,chat,p}(t_{sw,2j}) = \dot{x}_{12Fp,chat,p}(t_{sw,2j+2}) , \quad \dot{x}_{11Fp,chat,p}(t_{sw,2j+1}) = \dot{x}_{12Fp,chat,p}(t_{sw,2j+1}) , \quad (3.22)$$

must be satisfied at the time instants  $t_{sw,2j}$ ,  $t_{sw,2j+1}$  and  $t_{sw,2j+2}$  due to a periodic characteristic of the chattering. Here the subscript “11” stands for the time span  $t \in [t_{sw,2j}, t_{sw,2j+1}]$  and “12” for the time span  $t \in [t_{sw,2j+1}, t_{sw,2j+2}]$ . According to Eqs. (3.18)-(3.22), the coefficients  $K_1, K_2, K_3, K_4$  are derived as

$$K_1 = u_{1s} = -K_3 , \quad K_2 = \frac{\sin(\omega_0 T_s)}{1 + \cos(\omega_0 T_s)} u_{1s} = -K_4 . \quad (3.23)$$

The homogeneous solution  $x_{1h}(t)$  is given by

$$x_{1h}(t) = K_{1h} \cos(\omega_{eq}(t - t_{sw,2j})) + K_{2h} \sin(\omega_{eq}(t - t_{sw,2j})) , \quad (3.24)$$

and the term  $x_{1F}(t)$  by

$$x_{1F}(t) = K_{1F} \sin(\eta_d \omega_0 (t - t_{sw,2j})) , \quad K_{1F} = \frac{2\hat{F}}{k(1 - 2\eta_d^2)} . \quad (3.25)$$

Finally, inserting Eqs. (3.18), (3.24) and (3.25) into Eq. (3.17) results in the lumped formulation for  $x_1(t)$ ,

$$\boxed{x_1(t) = K_{1h} \cos(\omega_{eq}(t - t_{sw,2j})) + K_{2h} \sin(\omega_{eq}(t - t_{sw,2j})) + K_{1F} \sin(\eta_d \omega_0 (t - t_{sw,2j})) + x_{1Fp,chat,p}(t - t_{sw,2j}) ,} \quad (3.26)$$

where  $t_{sw,2j} \leq t < t_{sw,2j+2}$ . For the sake of simple formulation, here it is assumed that  $t_{sw,2j} = 0$ , the system goes into steady state. Given are the conditions,

$$x_1(0) = x_{10} , \quad \dot{x}_1(0) = \dot{x}_{10} , \quad x_2(0) = x_{20} , \quad t_{sw,2j} = 0 , \quad (3.27)$$

so the general solution  $x_1(t)$  can be determined and the coefficients  $K_{1h}, K_{2h}$  are calculated as

$$K_{1h} = x_{10} , \quad K_{2h} = \frac{\dot{x}_{10}}{\omega_{eq}} - \frac{\omega_0 \eta_d}{\omega_{eq}} K_{1F} - \frac{\omega_0}{\omega_{eq}} K_2 . \quad (3.28)$$

Finally, the steady state system response is obtained. How to determine  $u_{1s}$ , or in other words, seek a vibration energy limit, will be discussed in the next section.

### 3.4. Necessary Conditions for Vibration Energy Harvesting Limit

The spring forces become very large with the increase of the stored potential energy as shown in Fig. 2.11. Each spring can only accelerate the payload  $m_1$  in one direction, which leads to a unidirectional change of the payload velocity during each sample period  $T_s$ . So the sign of the velocity  $\dot{x}_1$ , as an example, can change in every sample

period due to large spring force as shown in Fig. 3.4, where

$$\dot{x}_1(t_{\text{sw},2j}) > 0, \quad \dot{x}_1(t_{\text{sw},2j+1}) < 0, \quad \dot{x}_1(t_{\text{sw},2j+2}) > 0. \quad (3.29)$$

Here  $t_{\text{sw},2j}$ ,  $t_{\text{sw},2j+1}$ , and  $t_{\text{sw},2j+2}$  are three adjacent switching time instants with a time interval  $T_s$ , namely,  $T_{1,j} = t_{\text{sw},2j+1} - t_{\text{sw},2j} = T_s$ ,  $T_{2,j} = t_{\text{sw},2j+2} - t_{\text{sw},2j+1} = T_s$  and  $T_{\text{sw},j} = 2T_s$ . In order to find necessary conditions for the velocity components

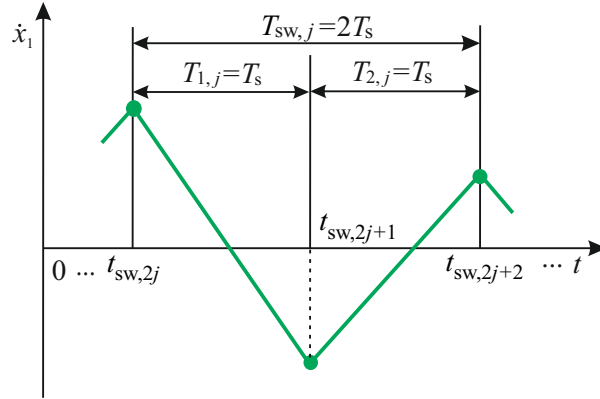


Figure 3.4.: Representation for the velocity response in one switching period  $T_{\text{sw},j}$ .

due to chattering, free vibration and forced vibration to fulfil the inequality conditions Eq. (3.29), the approximative time solution  $x_1(t)$  from Eq. (3.26) is inserted into Eq. (3.29). Evaluating the three inequality conditions leads to one common inequality condition

$$\omega_0 K_2 > \omega_{\text{eq}} \sqrt{K_{1h}^2 + K_{2h}^2} + \eta_d \omega_0 |K_{1F}|. \quad (3.30)$$

Substituting the expressions in Eq. (3.30) by their corresponding amplitudes of velocity components in terms of chattering response  $\hat{x}_{1Fp}$ , free response  $\hat{x}_{1h}$  and disturbance response  $\hat{x}_{1F}$

$$\hat{x}_{1Fp} = \omega_0 K_2, \quad \hat{x}_{1h} = \omega_{\text{eq}} \sqrt{K_{1h}^2 + K_{2h}^2}, \quad \hat{x}_{1F} = \eta_d \omega_0 |K_{1F}|,$$

finally results in the necessary conditions for the velocity amplitude of each vibration component

$$\boxed{\hat{x}_{1Fp} > \hat{x}_{1h} + \hat{x}_{1F}}. \quad (3.31)$$

It is concluded that if the chattering amplitude  $\hat{x}_{1Fp}$  produced by the process force  $F_p$  is larger than the sum of the other two parts, the system goes into steady state and will not harvest vibration energy any more. Out of the inequality (3.30) also necessary conditions for the system process parameters to obtain steady-state vibrations follow. Substituting the integration constants  $K_1, K_2, K_3, K_4, K_{1h}, K_{2h}$  in the inequality (3.30) gives the inequality condition for the initial spring deformations  $u_{1s}$  and  $u_{2s}$  or

the vibration energy harvesting limit

$$u_{1s} = -u_{2s} > \frac{1 + \cos\left(\frac{2\pi}{\eta_s}\right)}{\sin\left(\frac{2\pi}{\eta_s}\right)} \left( \frac{x_{10}^2}{4\omega_0 \dot{x}_{10}} + \frac{\dot{x}_{10}}{2\omega_0} + \frac{\eta_d \hat{F}}{k(\eta_d^2 - 1)} \right), \quad (3.32)$$

where  $\omega_{ep} = \sqrt{2}/2\omega_0$  according to Eq. (3.16). It is obvious when the deformations of the two springs are larger than a critical value, 4S allows a complete switching during  $2T_s$  as depicted in Fig. 3.4 and goes into steady state response. Based on the fundamental inequality principle, Eq. (3.32) can be rewritten as

$$u_{1s} = -u_{2s} > \frac{1 + \cos\left(\frac{2\pi}{\eta_s}\right)}{\sin\left(\frac{2\pi}{\eta_s}\right)} \left( \frac{\omega_{eq}}{\omega_0} |x_{10}| + \frac{\eta_d \hat{F}}{k(\eta_d^2 - 1)} \right). \quad (3.33)$$

If a zero initial condition is taken into consideration,  $x_1(0) = 0$  and  $\dot{x}_1(0) = 0$ , Eq. (3.33) will be further rewritten as

$$u_{1s} = -u_{2s} > \frac{1 + \cos\left(\frac{2\pi}{\eta_s}\right)}{\sin\left(\frac{2\pi}{\eta_s}\right)} \frac{\eta_d}{\eta_d^2 - 1} \frac{\hat{F}}{k}. \quad (3.34)$$

It can be deduced, that the pre-deformation of the springs depend on the static deformation due to the external disturbance  $\frac{\hat{F}}{k}$  as well as on the dimensionless excitation frequency  $\eta_d$  and sampling frequency  $\eta_s$ .

## 3.5. Numerical Analysis for Vibration Energy Harvesting Limit

In order to validate the above conclusion, the analytical solution for steady state vibrations according to Eq. (3.26) and the numerical simulation for 4S in the closed loop control with the velocity zero-crossing switching law Eq. 2.42 and Eq. 2.43 under several groups of different initial conditions according to Eqs. (3.32)-(3.34) are investigated.

### 3.5.1. Nonzero Initial Conditions

First, nonzero initial conditions,  $x_1(0) \neq 0$  and  $\dot{x}_1(0) \neq 0$ , are considered. The simulation parameters are listed in Table 3.1, and the initial conditions as expressed in Eq. (3.27),  $x_1(0) = x_{10} = 0.2$  m,  $\dot{x}_1(0) = \dot{x}_{10} = 0.35$  m/s, are used here as an example. Based on Eq. (3.32) the critical deformations of two springs are obtained,  $u_{1critical} \approx -u_{2critical} = 96.951$  m. Here  $x_2(0)$ , namely,  $u_{2s}$ , takes four values of -50, -90, -96.951 and -150, which represent different stored potential energy levels. The results

are depicted in Fig. 3.5. Green line denotes the numerical simulation results in closed

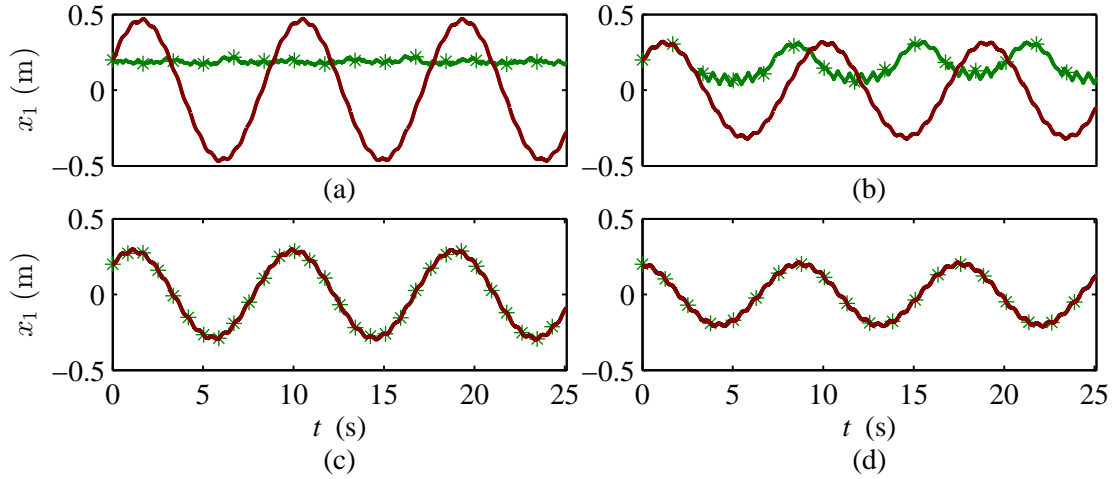


Figure 3.5.: System response for different deformations of two springs,  $u_{2\text{critical}} = -96.951$  m,  $x_1(0) = 0.2$  m and  $\dot{x}_1(0) = 0.35$  m/s. (a)  $x_2(0) = u_{2s} = -50$  m; (b)  $x_2(0) = u_{2s} = -90$  m; (c)  $x_2(0) = u_{2s} = -96.951$  m; (d)  $x_2(0) = u_{2s} = -150$  m. (Green: simulation in closed loop control; Red: analytical solution in open loop control)

loop control, and red line stands for the analytical solution, where 4S switches within every sampling period  $T_s$ .

Fig. 3.5(a)-(d) show that the analytical steady-state solution always oscillates like a passive system. This phenomena has been mentioned in Subsection 2.3. But the system response in closed loop control shows an obvious difference under different stored potential energies, denoted by  $u_{2s}$ . Fig. 3.5(a) shows that when the spring deformation quantity  $|u_{2s}| < |u_{2\text{critical}}|$ , that is to say, not enough potential energy is stored in the springs, 4S continues responding to the switching law and harvesting vibration energy. As a result, the system chatters around the initial position  $x_1(0)$ . With an increase in the spring deformation  $u_{2s}$ , more potential energy is stored in the system and it shows a larger amplitude oscillation as illustrated in Fig. 3.5(b). From Fig. 3.5(c)-(d) it is clear to see that if the spring deformation quantity  $|u_{2s}| \geq |u_{2\text{critical}}|$ , namely, enough potential energy is stored in the system, these two system response curves match quite well. This means that the system does not harvest vibration energy any longer and acts like an open loop control system and oscillates finally. Thus, it is concluded that vibration energy harvesting limit may occur in the proposed system governed by the switching law according to Eq. (2.38).

### 3.5.2. Zero Initial Conditions

Apart from nonzero initial conditions, zero initial conditions are also considered here,  $x_1(0) = 0$  and  $\dot{x}_1(0) = 0$ . According to Eq. (3.34), when the energy harvesting limit occurs,  $|u_{2\text{critical}}| = 32.1524$ . Similarly, both the simulation analysis in closed loop control and the analytical solution are executed and the results are shown in Fig. 3.6.

The other parameters are listed in Table 3.1. Like what happens under nonzero initial conditions, when  $|u_{2s}| \geq 32.1524$ , 4S does not harvest kinetic energy any more and oscillates similar to an open loop control system as depicted in Fig. 3.6(c) and (d). Differing from the nonzero initial condition case with a critical limit of  $|u_{2critical}| = 96.951$ , the free response term disappears in the zero initial condition case, having a critical limit of  $|u_{2critical}| = 32.1524$  as shown in Fig. 3.6(c), according to Eq. (3.26) and Eq. (3.28). 4S oscillates based on the superposition of the disturbance response and chattering response terms.

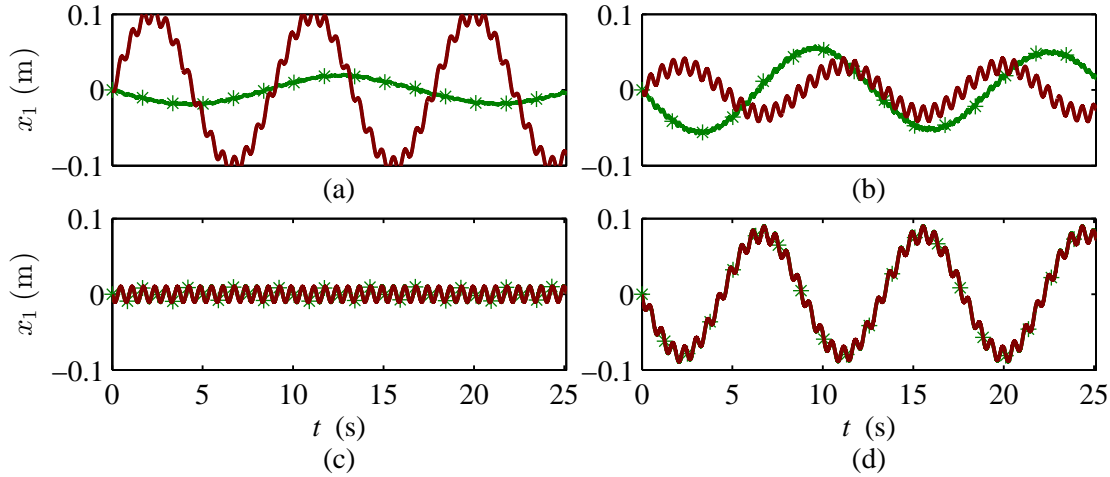


Figure 3.6.: System response for different deformations of springs,  $u_{2critical} = -32.1524$  m,  $x_1(0) = 0$  and  $\dot{x}_1(0) = 0$ . (a)  $x_2(0) = u_{2s} = -10$  m; (b)  $x_2(0) = u_{2s} = -25$  m; (c)  $x_2(0) = u_{2s} = -32.1524$  m; (d)  $x_2(0) = u_{2s} = -50$  m. (Green: simulation in closed loop control; Red: analytical solution)

### 3.5.3. Extended Time Numerical Simulation

As shown in Fig. 3.5 and Fig. 3.6, there must exist a vibration energy harvesting limit in system response. When the system has stored the maximum potential energy, denoted by  $u_{2critical}$ , it will go into steady state response. In order to show the entire vibration energy harvesting process, from zero to the maximum, the numerical simulation is executed for a long time. The model parameters are listed in Table 3.1 and the results are depicted in Fig. 3.7. The left side zoomed-in subfigure pairs [(b), (d), (f), (h)] show the free and disturbance response terms, where  $t \in [t_0, t_0 + 20]$ . In order to further show the chattering response, the right side subfigure pairs [(c), (e), (g), (i)] are drawn at  $t \in [t_0 + 10, t_0 + 10.05]$ , where  $t_0 = 10^6$  s.

From Fig. 3.7(a) it is obvious that the system harvests the maximum potential energy at  $t \approx 9.2 \times 10^5$  s and then goes into steady state. Afterwards, the displacement of the payload,  $x_1$  and the deformations of two springs,  $u_1$  and  $u_2$  remain at an equilibrium-like position. Note that this is not a strict equilibrium but chattering around an equilibrium position. As mentioned before, the steady state response consists of a free



response term with the frequency  $\omega_{\text{eq}}$ , a disturbance response term with the frequency  $\Omega$  as depicted in subfigure pairs [(b), (d), (f), (h)], and a chattering response term with the frequency  $\Omega_{\text{sw}}$  in subfigure pairs [(c), (e), (g), (i)]. When 4S goes into steady state, a large enough potential energy stored in two springs makes the chattering velocity amplitude larger than the sum of the free and disturbance response according to Eq. (3.30) and Eq. (3.31). As a result, the sign of velocity will change within every sampling period  $T_s$  as shown in Fig. 3.7(i). Fig. 3.7(h) shows that similar to the displacement response, the velocity of payload  $\dot{x}_1$  also varies periodically.

When the system goes into steady state, the switching law allows 4S to behave like an open loop controlled system with the duty cycle  $D_{k1} = 0.5$  as mentioned in Section 2.3. If  $D_{k1} = 0.5$ , the entire system can be seen as a passive system with two identical springs in serial with each other, where the displacement of payload,  $x_1$  is the sum of the deformations of two springs,  $u_1$  and  $u_2$ . Meanwhile, the amplitude of the former is two times that of the latter. The equivalent natural period of the system, marked by  $T_{\text{eq}}$  in Fig. 3.7(f), is equal to 8.8871 s, which agrees with Eq. (2.35).

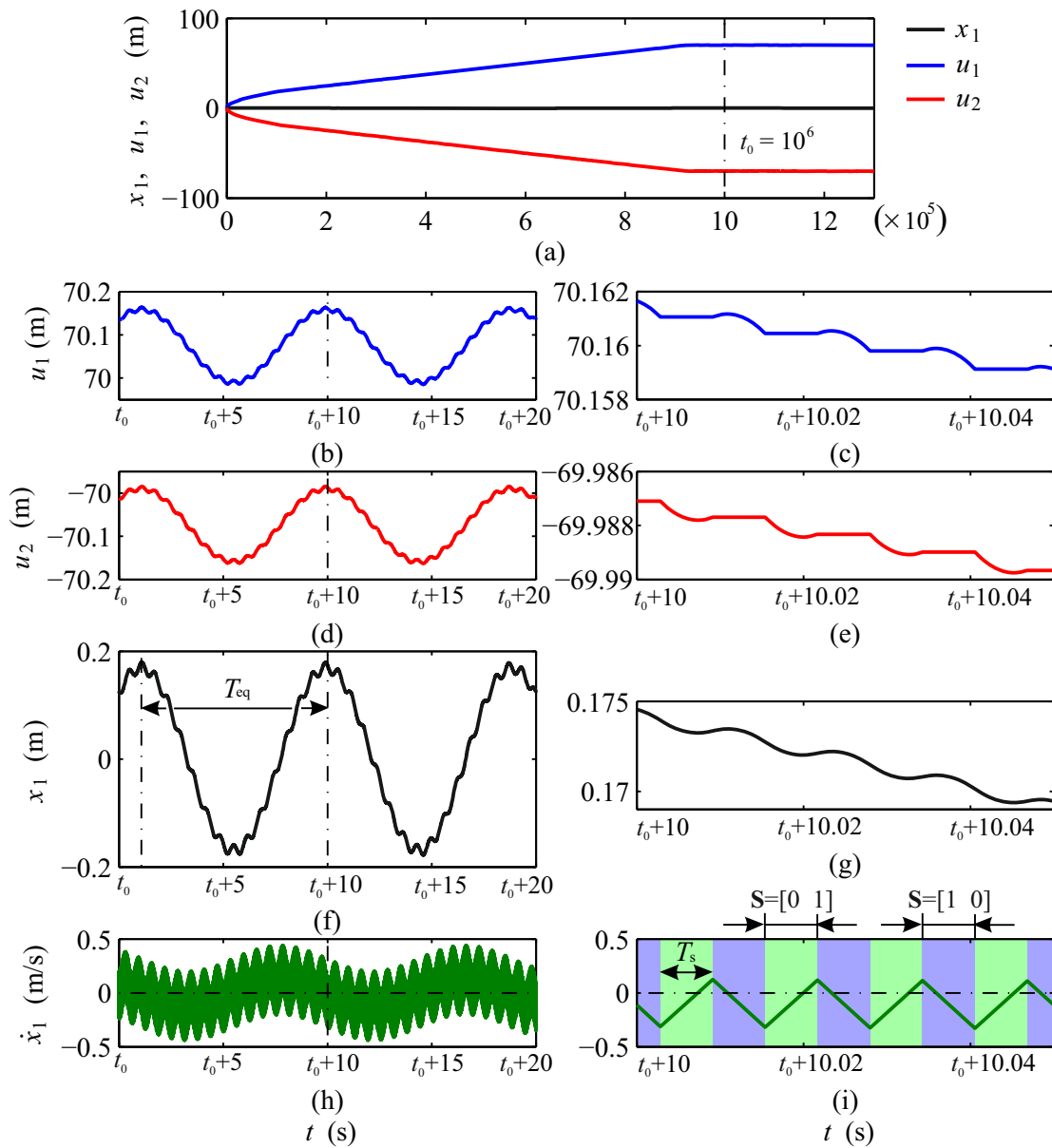


Figure 3.7.: System response for a long time, here  $t_0 = 10^6$  s. (a) Lumped system response for a long time; (b), (d), (f) and (h): Zoomed-in pictures at  $t_0 = 10^6$  s marked by dot dash line in (a); (c), (e), (g) and (i): Zoomed-in pictures at  $t_0 + 10$  s marked by dot dash line in (b), (d), (f) and (h), respectively.

---

## Experimental Validation

---

### 4.1. Introduction

As mentioned in Subsection 2.4.3, a fast clamping device, namely, a mechanical switch, is required for 4S to achieve fast stiffness switching as shown in Fig. 2.11, therein  $\eta_s = 1000$ . In practice it is difficult to design such a fast mechanical switch, therefore the proposed vibration control strategy should be applied to a low natural frequency system with a low stiffness or a high inertial payload. Considering the cost of a test rig, an electromagnet actuator is used as the mechanical switch firstly. The settling time of an electromagnet actuator ranges from several to several tens of milliseconds. This constrains 4S to work under a low switching frequency of several tens to several hundreds of Hertz. In order to achieve a reliable switching, system sampling frequency  $\omega_s$  should not be extremely high due to switching frequency  $\omega_{sw}$  being determined by the sampling frequency. A high sampling frequency will result in a high switching frequency and for this a fast mechanical switch is needed.

A low translation system stiffness contributes to a low dynamic system design but leads to a relatively large linear deformation and further enlarges a setup space. To avoid this, a rotational test rig is taken into consideration. The natural frequency of a rotational dynamic system  $\omega_0$  is given by

$$\omega_0 = \sqrt{\frac{k_\theta}{J}} = \sqrt{\frac{k_\theta}{\sum m_i r_i^2}}, \quad i = 1, 2, \dots \quad (4.1)$$

where  $k_\theta$  is rotational stiffness,  $J$  is the moment of inertia of the protected payload and  $m_i, r_i$  are the corresponding effective rotation mass and radius.

In this chapter, at first, the operation principle and modeling of a rotational test rig are considered. Following is the setup construction including the mechanical structure and

electronic part. After that the experiment investigating vibration energy harvesting and vibration reduction performance is carried out.

## 4.2. Operation Principle and Modeling of Setup

### 4.2.1. Operation Principle

A compact rotational setup is introduced as shown in Fig. 4.1, where the model in Fig. 4.1(a) is added to aid in understanding the rotational setup. Considering the two springs to be not equal in reality due to a manufacturing error, different stiffness  $k_1$  and  $k_2$  are used here.

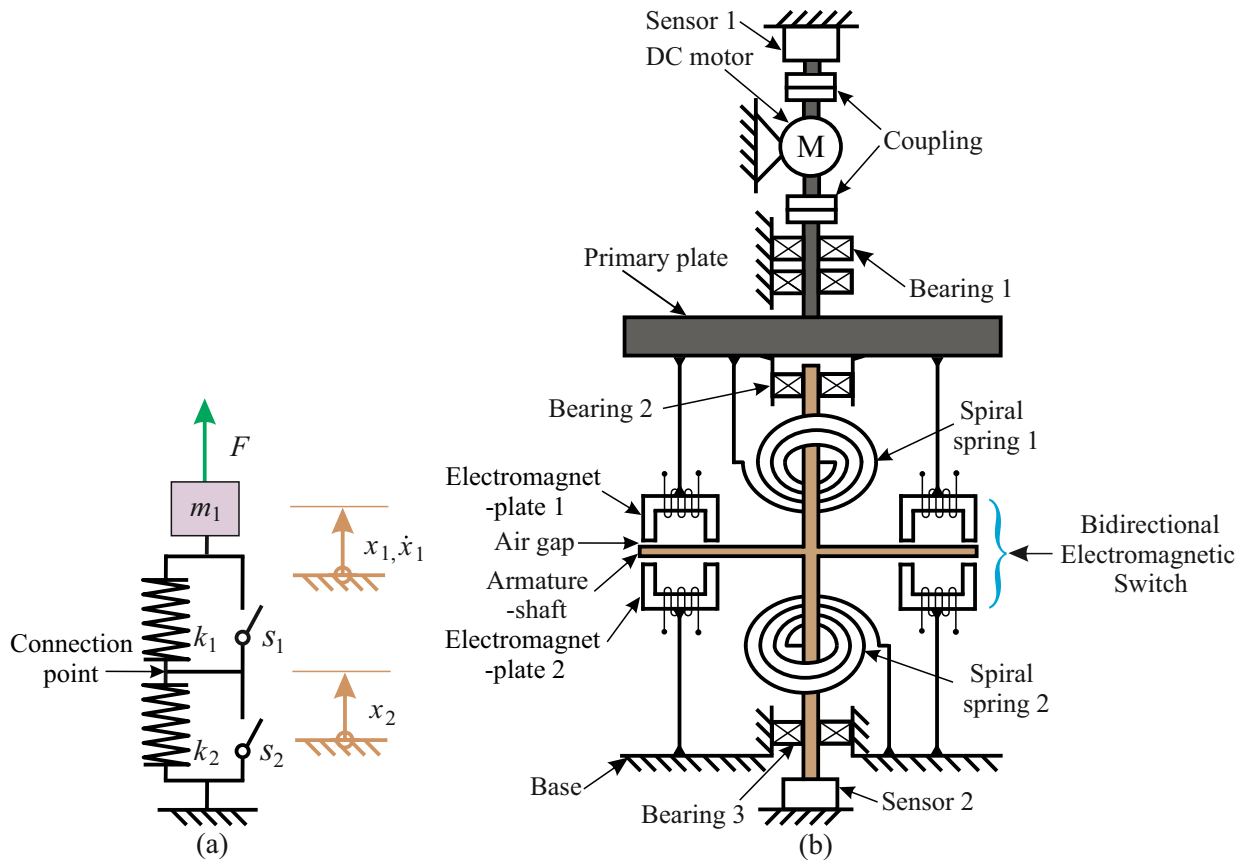


Figure 4.1.: Schematic for 4S setup. (a) Translation model of 4S; (b) Schematic for rotational test rig.

The setup consists of two spiral springs, a primary plate, an armature-shaft, three bearing blocks, two electromagnet-plates and a DC motor. The electromagnet-plate here refers to a circular plate with eight built-magnet cores attached. These eight magnet cores are distributed evenly in the circumferential direction to produce an evenly distributed friction force on the armature when they are attracted to the armature. There exist two rotation blocks in the system, the first one is composed of the DC motors rotor, coupling and primary plate, and the second one is the armature-shaft. An

armature-shaft consists of one armature and one rotation shaft, which are connected together. The armature-shaft and two electromagnet-plates constitute a bidirectional clamping device, which works as two mechanical switches, in other words, two electromagnetic switches or one bidirectional electromagnetic switch as marked in Fig. 4.1(b). One end of two spiral springs is fixed on the armature-shaft and the other ends are fixed on the primary plate and the base, respectively.

For a rotation case, the moment of inertia of the system, determined by both of the mass and geometry of a rotation block according to Eq. (4.1), plays an important role on system dynamics. The connection point mass, marked in Fig. 4.1(a), is theoretically neglected as mentioned in Subsection 2.2.3. Therefore, in order to satisfy the above mentioned massless condition, two design aspects must be considered. One is that the moment of inertia of the armature-shaft should be as low as possible and the other is the moment of inertia of the primary plate as high as possible. With the aim of increasing the moment of inertia of the primary plate, not only its mass but also its geometry variables might be taken into consideration according to Eq. (4.1).

Whether or not two springs are active depends on the attraction between the armature-shaft and two electromagnet-plates. The operation principle can be described as follows. When electromagnet-plate 2 is powered on, the electromagnetic force allows the connection of the armature-shaft to the base, namely,  $s_2$  is closed as shown in Fig. 4.1(a). As a result, spiral spring 2, namely,  $k_2$  is blocked and spiral spring 1,  $k_1$  is active and the non-energized electromagnet-plate 1 would follow the primary plate and rotate together. Spiral spring 1,  $k_1$  would be extended and harvests kinetic energy as potential energy stored in spring 1 according to the switching law in Eq. (2.38). When the switching between two stiffness states occurs, electromagnet-plate 2 is powered off and electromagnet-plate 1 powered on. The electromagnetic force would connect the armature-shaft to the primary plate. Consequently, the primary plate, electromagnet-plate 1 and armature-shaft are combined together and driven by the DC motor, namely,  $s_1$  is closed and  $s_2$  is open as shown in Fig. 4.1(a). At this time phase, spiral spring 1,  $k_1$  is blocked and spiral spring 2,  $k_2$  is active, compressed and would harvest kinetic energy.

### 4.2.2. Modeling

The lumped model of the rotational setup is depicted in Fig. 4.2(a) with Fig. 4.2(b) being the corresponding translational model. The previously mentioned system refers to a translational model, where the connection point is assumed to be massless. Here a rotational setup is designed. The connection point, namely, the armature-shaft has mass  $m_2$  or moment of inertia,  $J_2$ , but it is still neglected initially in order to match with the aforementioned theory analysis. Of course, the moment of inertia of the primary plate  $J_1$  being much larger than  $J_2$  makes this more reasonable. The electromagnetic force friction-based clamping device is still simplified to be an ideal switch as denoted by  $s_1$  and  $s_2$ . System damping including viscous damping and Coulomb damping is considered. The system dynamics can be expressed as follows. The deformations of two spiral springs  $u_1$  and  $u_2$  can be given by

$$u_1 := \theta_1 - \theta_2, \quad u_2 := \theta_2, \quad (4.2)$$

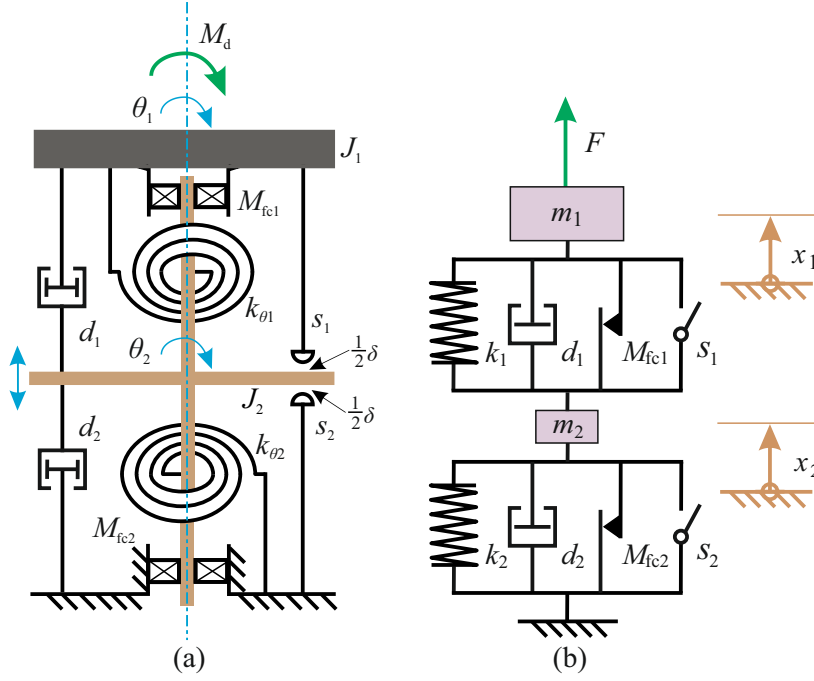


Figure 4.2.: Simplified model of the 4S setup. (a) Partly simplified rotation model with damping; (b) Simplified translation model with damping.

where  $\theta_1$  and  $\theta_2$  are the rotation angles of the primary plate and the armature-shaft, respectively. Accordingly, the two spiral springs torques  $M_{k1}$ ,  $M_{k2}$  are given by

$$M_{k1} = k_{\theta 1} u_1, \quad M_{k2} = k_{\theta 2} u_2. \quad (4.3)$$

The frictional moment  $M_f$  includes viscous damping  $M_{fv}$  such as air damping, and Coulomb damping  $M_{fc}$  around a bearing and a sensor.  $M_{f1}$  can be expressed by

$$M_{f1} = M_{fv1} + M_{fc1}, \quad M_{fv1} = d_1(\dot{\theta}_1 - \dot{\theta}_2), \quad (4.4)$$

and  $M_{f2}$  is given by

$$M_{f2} = M_{fv2} + M_{fc2}, \quad M_{fv2} = d_1 \dot{\theta}_2, \quad (4.5)$$

here  $M_{fc1}$  and  $M_{fc2}$  are complicated to formulate and not given. These damping can be further confirmed in experiments.

When  $\mathbf{S} = [1, 0]$ , electromagnet-plate 1 is powered off and electromagnet-plate 2 powered on. The armature-shaft is connected to the base. As a result, spiral spring 2 is blocked and spring 1 is active. Similar to the translation model in Subsection 2.2.3, the motion equation of the system will be given by

$$J_1 \ddot{\theta}_1 = M_d - M_{k1} - M_{f1}, \quad \theta_2 = \theta_2(t_{sw,i}), \quad (4.6)$$

where  $t_{sw,i}$  is the  $i$ th switching time instant as expressed in Subsection 2.2.3.  $M_d$  is the external disturbance torque produced by a DC motor, similar to the disturbance  $F$  depicted in Fig. 4.2(b).

In the case  $\mathbf{S} = [0, 1]$ , where spiral spring 1 is not active but spiral spring 2 active,

the system dynamics can be given by

$$J_1\ddot{\theta}_1 = M_d - M_{k2} - M_{f2} , \quad \theta_2 = \theta_1 - [\theta_1(t_{sw,i}) - \theta_2(t_{sw,i})] . \quad (4.7)$$

In order to achieve a pure stiffness system as mentioned in the theory analysis, the frictional torque  $M_f$  should be as low as possible. Similar to the theory model according to Eq. (2.15)-Eq. (2.16), a compact formulation for the rotational model can be given by

$$J_1\ddot{\theta}_1 + k_\theta\theta_1 = M_d + M_p(\mathbf{S}) \quad (4.8)$$

and

$$\theta_2(\mathbf{S}) = \begin{cases} \theta_2(t_{sw,i}) & \text{if } \mathbf{S}(t) = [1, 0] \\ \theta_1 - [\theta_1(t_{sw,i}) - \theta_2(t_{sw,i})] & \text{if } \mathbf{S}(t) = [0, 1] \end{cases} , \quad (4.9)$$

and the process torque  $M_p(\mathbf{S})$  is given by

$$M_p(\mathbf{S}) = \begin{cases} k_\theta u_2 & \text{if } \mathbf{S}(t) = [1, 0] \\ k_\theta u_1 & \text{if } \mathbf{S}(t) = [0, 1] \end{cases} , \quad (4.10)$$

where  $k_{\theta_1} = k_{\theta_2} = k_\theta$  and the damping is not considered. Considering the difference of two springs and the moment of inertia of armature-shaft  $J_2$ , the natural frequencies of two undamped subsystems, denoted by  $J_1-k_{\theta_1}$  and  $(J_1 + J_2)-k_{\theta_1}$  here, differ from the aforementioned one according to Eq. (2.21) and can be given by

$$\omega_{01} = \sqrt{\frac{k_{\theta_1}}{J_1}} \quad \text{and} \quad \omega_{02} = \sqrt{\frac{k_{\theta_2}}{J_1 + J_2}} . \quad (4.11)$$

If  $J_1 \gg J_2$  and  $k_{\theta_1} \approx k_{\theta_2}$  are set in design,  $\omega_{01} \approx \omega_{02}$ , which agrees with the mentioned theory model. The attraction and releasing between the electromagnet-plate and armature-shaft creates the switching between two stiffness states. During this process, the armature-shaft moves between two electromagnet-plates in the vertical direction with an air gap of  $\delta$  as shown in Fig. 4.2(a), where the armature lies in the middle of air gap. The linear motion equation of armature in the vertical direction can be given by

$$m_2\ddot{\delta} = F_{em} , \quad (4.12)$$

where  $m_2$  is the mass of armature and  $F_{em}$  is an electromagnetic force. As such, the needed motion time  $t_{\text{motion}}$  of the proposed mechanical switch can be written as

$$t_{\text{motion}} = \sqrt{\frac{2\delta m_2}{F_{em}}} . \quad (4.13)$$

In order to obtain a realizable switching between two stiffness states and reduce the effect of a switching delay governed by  $t_{\text{motion}}$  on the system response, the switching time  $t_{\text{motion}}$  should be as low as possible, namely,

$$t_{\text{motion}} \ll T_s . \quad (4.14)$$

where  $T_s$  is the sampling period. To achieve a reliable clamping, the stored potential energy, namely, spiral spring torques  $M_{k1}$  and  $M_{k2}$  should satisfy with the following

inequality,

$$(M_{k1} + M_{k2}) < M_c . \quad (4.15)$$

where  $M_c$  is defined as the clamping torque or frictional torque produced by the mechanical switch. It is obvious to see that the stored potential energy denoted by  $M_{k1}$  and  $M_{k2}$  must be always lower than an external provided energy partly represented by  $M_c$ . If the above condition holds, the spiral spring can be blocked. The clamping torque  $M_c$  can be expressed by

$$M_c = F_{em} r_{em} , \quad (4.16)$$

where  $r_{em}$  is an effective distance between electromagnet force  $F_{em}$  acting point and rotation shaft. The simulation analysis is executed in Matlab/Simulink, where the motion time of the armature-shaft  $t_{motion}$  is not considered initially to simplify the simulation analysis.

## 4.3. Setup Construction

### 4.3.1. Mechanical Structure

For 4S, as a switching system, a mechanical switch is important and would directly determine the system performance. As such, the design of a mechanical switch will be explained in detail in the following subsection.

#### Mechanical switch unit

The electromagnetic switch is a kind of friction-based clamping device based on an electromagnetic actuator. Through the attraction and releasing between the armature-shaft and electromagnet-plate, the connection or disconnection of two spiral springs to or from the primary plate can be realized. With the aim of a reliable attraction, the electromagnetic torque should be not only large enough but also evenly distributed in circumferential direction on the surface of armature. As a result, a ring-arranged electromagnet-plate and a hollow armature structure are proposed as shown in Fig. 4.3(a). Eight U-magnets are evenly arranged in an aluminium housing and share one coil to reduce space. Magnetic cores are chosen to be the stacking structure consisting of metal sheets in order to reduce the intensity of eddy current losses and keep a high flux carrying capacity. The provided static electromagnetic force  $F_{em}$  can be given by

$$F_{em} = \frac{B^2 A_{em}}{2\mu_0} \cdot n , \quad (4.17)$$

where  $A_{em}$  is the working area of an electromagnet and  $n$  is the number of electromagnets, here  $n = 8$ .  $\mu_0$  is the vacuum permeability and  $B$  is magnetic flux density and can be given by

$$B = \frac{\Theta \mu_0}{2\delta}, \quad \Theta = Ni , \quad (4.18)$$



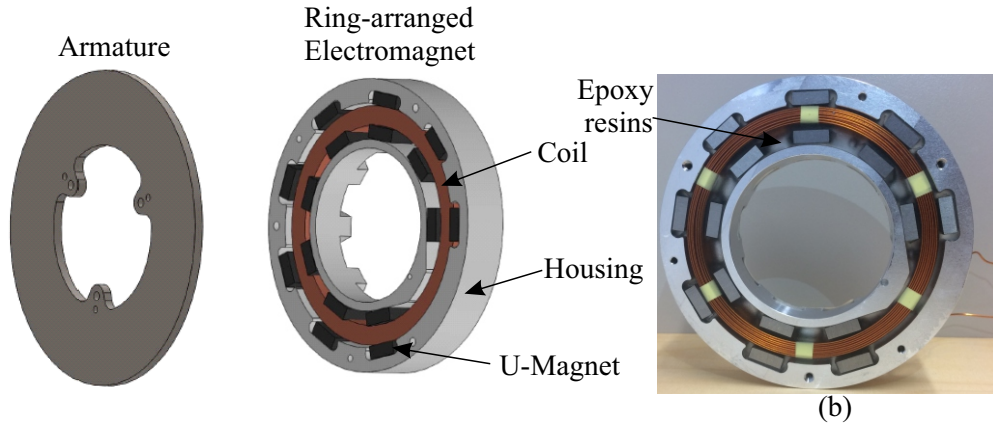


Figure 4.3.: Schematic for the build-up of a mechanical switch. (a) CAD model for an armature and a ring-arranged electromagnet plate; (b) Prototype of a ring-arranged electromagnet plate.

where  $N$  is the number of coils and  $i$  is the current applied to an electromagnet and  $\Theta$  is magnetomotive force. Here compared to the reluctance produced by air gap, the reluctance produced by an magnet core is small and can be neglected. The relationship between the current  $i$  and voltage  $U$  for the electromagnet can be given by

$$U = iR + L(\delta) \frac{di}{dt} + i \frac{dL(\delta)}{d\delta} \frac{d\delta}{dt}, \quad (4.19)$$

where  $R$  is the resistance of coils and  $L(\delta)$  is a variable inductance with respect to the variation of air gap. In order to fix the coil and magnet cores, the housing is filled with transparent epoxy resins. This experimental ring-arranged electromagnet-plate is shown in Fig. 4.3(b). Unalloyed structural steel 1.0037 is used for the armature design. Cast steel C5 is used for the U magnet cores (information from Gebrueder Waasner Elektrotechnische Fabrik GmbH, SM42 C5-110). The electromagnetic force causes the vertical translation of armature-shaft, as depicted in Fig. 4.2(a), and allows the clamping and releasing of the electromagnet-plate and armature-shaft. A long motion time of the armature-shaft will result in a switching delay and strongly affect the system response. In order to reduce the motion time of armature-shaft, a lightweight armature is required. For this a hollow circular armature structure is used as shown in Fig. 4.3(a). Meanwhile, the cross section of the armature should be large enough to increase magnetic flux and reduce magnetic resistance.

Here, two designs for the outside radius  $R$  of the armature are proposed as depicted in Fig. 4.4 and Fig. 4.5, where subfigures (a) and (b) represent the magnetic field lines in different viewing directions. The inside diameter  $r$  of the armature is determined by the outside radius of the used spiral spring as mentioned in the following subsection.  $a$  and  $b$  are the two sides of the U-magnet working area and  $c$  represents the distance between two magnetic poles N and S. The first design aims to reduce the thickness of the armature with a larger outside radius  $R$  and meanwhile, in order to avoid an oversized cross section, the distance from the rand of the magnet working area to the rand of the armature is set to be  $a/2$  considering the symmetrical distribution of magnetic field. The second design aims to decrease the outside radius  $R$  of the

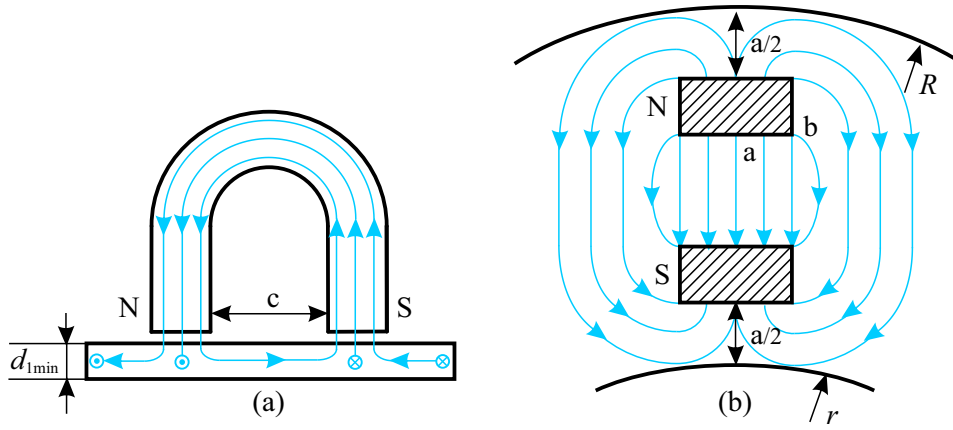


Figure 4.4.: Schematic for the magnetic field lines distribution for the first design.

armature as much as possible. The distance from the rand of the magnet working area to the rand of the armature is nearly zero. The minimum thickness of armature  $d_{1min}$  in Fig. 4.4 and  $d_{2min}$  in Fig. 4.5 according to Eq. (B.3) can be given by

$$d_{1min} \approx \frac{ab}{2(a+b)}, \quad \text{and} \quad d_{2min} \approx \frac{ab}{a+2b}, \quad (4.20)$$

Although  $d_{1min}$  is smaller than  $d_{2min}$ , it is proven that the armature volume for the first design is larger than the second one according to Eq. (B.9). Therefore, the second design is taken.

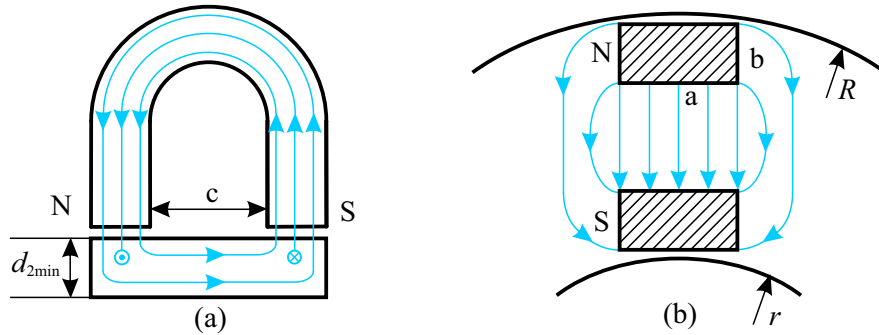


Figure 4.5.: Schematic for the magnetic field lines distribution for the second design.

Because the armature, not the armature-shaft, moves axially in the working air gap between the two electromagnet-plates, a reasonably low axial stiffness of the armature is able to avoid the reduction of effective normal electromagnetic force acting on the armature. At the same time, the armature should also be stiff enough to transmit circumferential torque from the primary plate to rotation shaft, here a triangle spring is designed as depicted in Fig. 4.6. Fig. 4.6(a) is the experimental triangle spring and Fig. 4.6(b) shows the stress analysis when the maximum axial deformation, equaling to the maximal working air gap between two electromagnet-plates,  $\delta = 1$  mm, is applied to the triangular spring. Except the stress concentration, the design can be accepted in experiment. A corresponding axial deformation force  $F_d$  produced by an

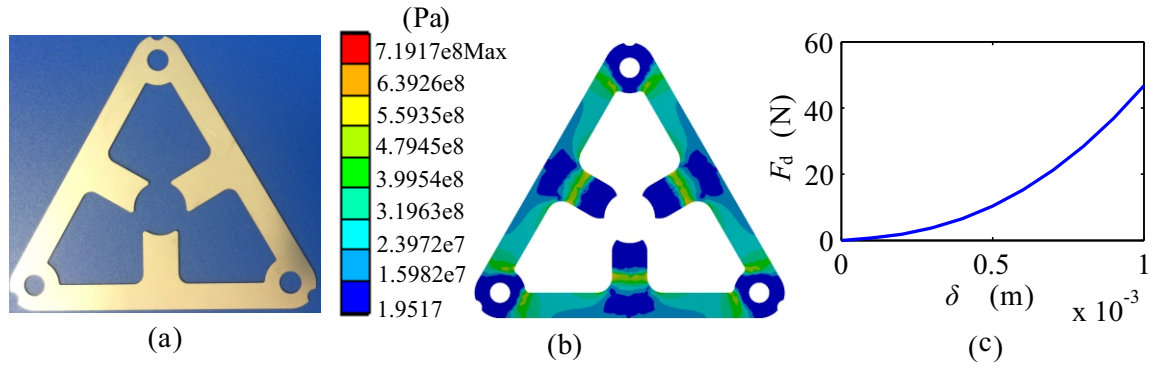


Figure 4.6.: Schematic for the triangle spring. (a) Experimental triangle spring; (b) Stress analysis for the triangular spring structure; (c) Relationship between the force and the axial deformation as denoted by the working air gap of electromagnet  $\delta$ .

axial deformation of the triangle spring is larger than 45 N as shown in Fig. 4.6(c), which shows the nonlinear relationship between the axial deformation force  $F_d$  and the axial deformation. In fact, the applied working air gap in experiment is about 0.6 mm. This means  $F_d \approx 15$  N. According to Eq. (4.13), the motion time  $t_{\text{motion}}$  of armature from one electromagnet plate to the other can be approximately modified to

$$t_{\text{motion}} = \sqrt{\frac{2\delta m_2}{F_{\text{em}} - F_d}}. \quad (4.21)$$

Here  $m_2 = 0.33$  kg,  $\delta = 0.6$  mm and  $F_{\text{em}} = 35$  N according to Eq. (4.17), so the motion time  $t_{\text{motion}}$  of the armature from one electromagnet to the other is 4.5 ms. As a result, the sampling time  $T_s$  of the controller should be larger than 4.5 ms. Fig. 4.7 shows the construction of the armature-shaft. The armature and triangle spring are connected

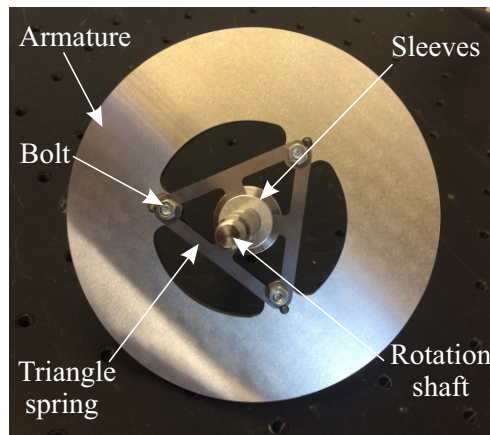


Figure 4.7.: Build up of the armature-shaft.

through three bolts and then can be fixed on a rotation shaft through the squeezing of sleeves.

## Spring unit

A spiral spring (Gebr. Schmidt Federnspezialfabrik GmbH) is used for potential energy storage on the rotational test rig. The rotational stiffness  $k_\theta$  is given by

$$k_\theta = \frac{Ebt^3}{12l}, \quad l = \pi n(R_o + R_i), \quad (4.22)$$

where  $E$  is the elastic modulus of the spiral spring material;  $b$ ,  $t$  and  $l$  are the width, thickness and length of a spiral spring, respectively;  $R_o$  and  $R_i$  are the outside and inside radius of the spiral spring. The maximum acceptable torque  $M_{k_{\max}}$  can be expressed by

$$M_{k_{\max}} = \frac{\sigma bt^2}{6}, \quad (4.23)$$

where  $\sigma$  is the yield strength of the spiral springs material. As such, the potential energy harvesting level of the rotational setup should be lower than  $M_{k_{\max}}$ . The above spiral spring design principle is from the company. The fixture of a real spiral spring is shown in Fig. 4.8, where one end of the spiral spring is fixed on the circular plate by a bolt and the other is inserted into the groove of a sleeve.

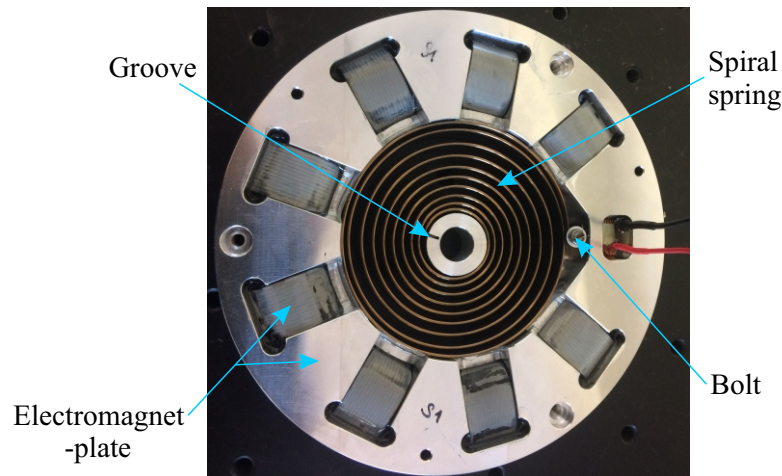


Figure 4.8.: Fixture of a spiral spring in an electromagnet-plate.

## Lumped mechanical setup

The lumped mechanical setup is shown in Fig. 4.9. In order to see the internal structure of 4S, marked by a blue rectangular frame in the upper subfigure, a CAD cross-sectional view is shown in the lower subfigure. To avoid the spiral spring coils falling off and contacting the wall of electromagnet-plate due to gravity, the setup is hung vertically fixed on an aluminum frame. Considering the massless connection point in the theory analysis, the moment of inertia of the armature-shaft should be much lower than that of the primary plate. Thus, an auxiliary rotation block is fixed to the primary plate. After that, the ratio of the moment of inertia of the primary state to that of the

armature-shaft is 15.37. As a result, the moment of inertia of the armature-shaft can be neglected in modeling.

### Sensor and electric drive

Two incremental rotary encoders are used for the angular positioning of the primary plate and armature-shaft. One is from Hohner Elektrotechnik GmbH, PR90-11C1C-C, and has a resolution of 16384 pulse per turn. The other is from Dr. Johannes Heidenhain GmbH, ROD 426.000B, and owns a resolution of 10000 pulses per turn. According to the aforementioned switching law Eq. (2.38), an accurate switching between two stiffness states requires an accurate real-time acquisition of the angular position of the primary plate. Therefore, the former is used for the primary plate and the latter for the armature-shaft. The moment of inertia of the rotary encoders rotors are  $30 \text{ (g} \cdot \text{cm}^2)$  and  $26 \text{ (g} \cdot \text{cm}^2)$ , respectively. They can be neglected when compared to the primary plate. The starting torque of two sensors rotors, seen as frictional torque, is lower than 0.01 Nm. The two sensors are connected to the output shaft of a DC motor and the armature-shaft by means of two couplings, respectively.

A graphite brushed DC motor from Maxon Motor GmbH, DCX32L, with the advantage of high reliability, simple control and low cost, is used for the production of an external disturbance acting on the primary plate.

## 4.3.2. Power Electronics

### Current control scheme for electromagnet

The current control for electromagnet is schematically shown in Fig. 4.10. In order to reduce electric power loss and overheating, a switching power circuit, Motor Control Shield with BTN8982TA for Arduino(Infineon Company), is applied. It mainly consists of a H bridge circuit. A hysteresis controller is used to reduce the chattering frequency resulting from a switching power electronic. The reference current  $i_{em, ref}$ , governing the power on-off states of two electromagnets, is controlled by the switching law. The high-low signal level from the hysteresis controller determines the positive and negative circuit of H Bridge. As such, a switching voltage is exerted on an electromagnet.

### Current control for DC motor

A specified disturbance torque is needed for the validation of vibration reduction performance and vibration energy harvesting of the proposed vibration control system. Therefore, the disturbance torque should be accurately provided and controlled. Considering the difficulty and the cost of direct torque control for a DC motor and the linear relationship between the current in the motor and the output torque, a current control scheme for the DC motor is applied here. First, the governing equations to describe the system dynamics of a DC motor are given by

$$M_d = K_t i_m, \quad (4.24)$$

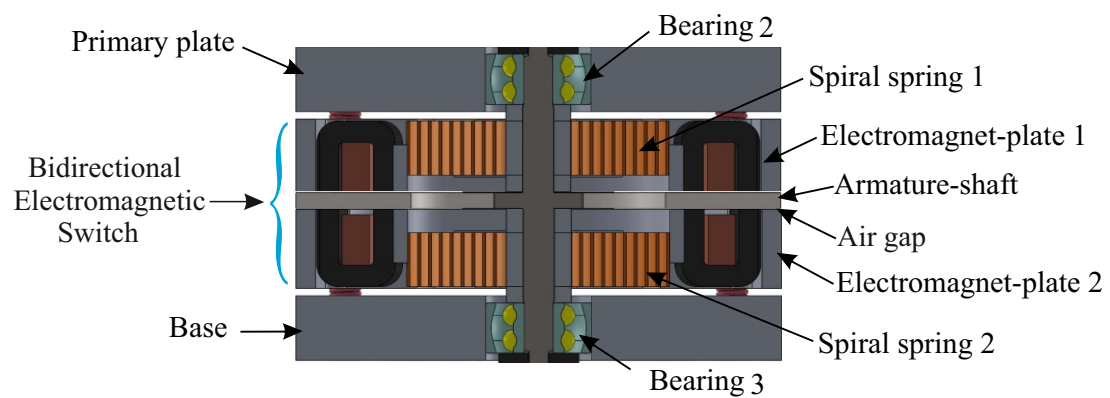
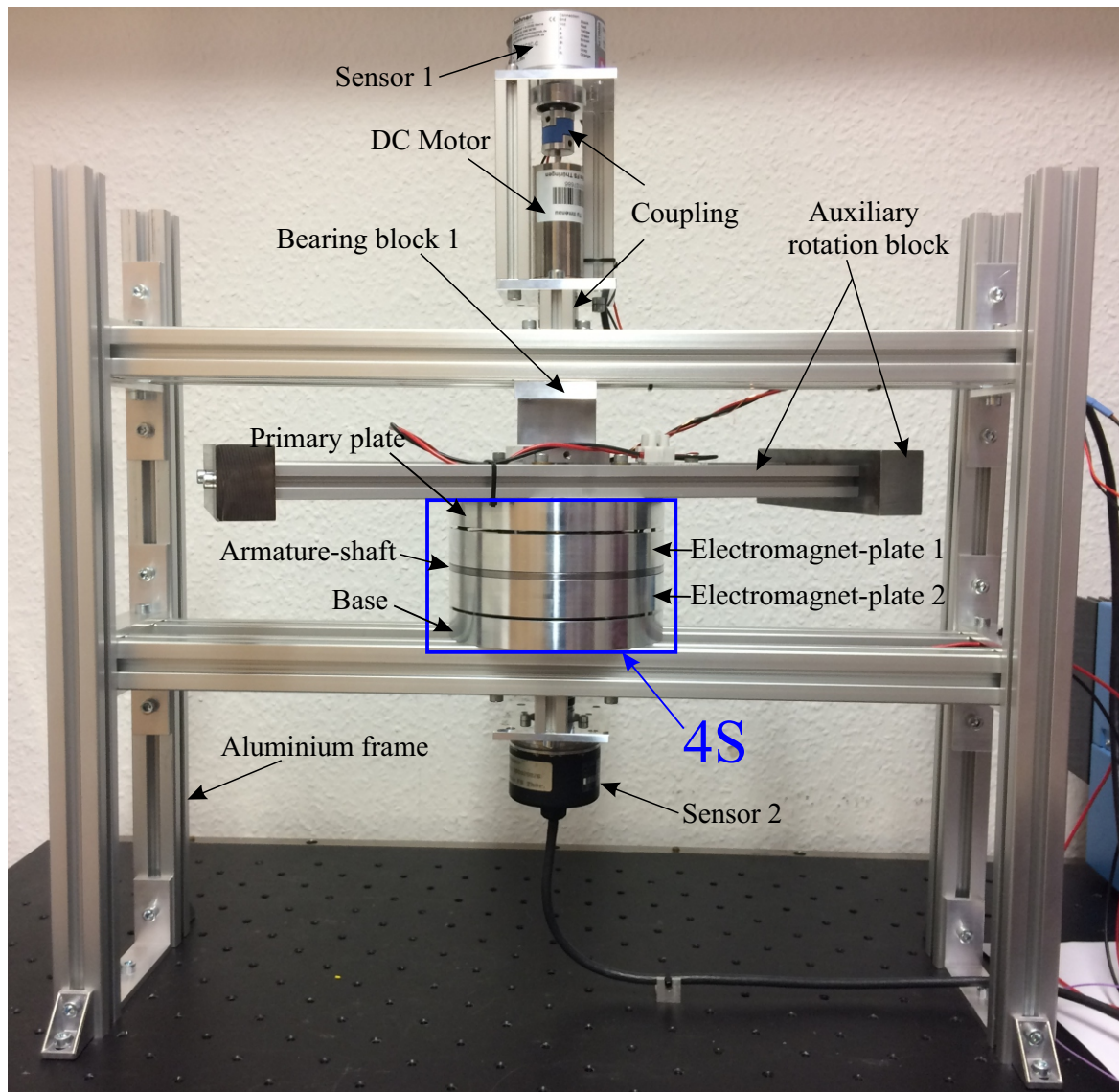


Figure 4.9.: Lumped mechanical setup.

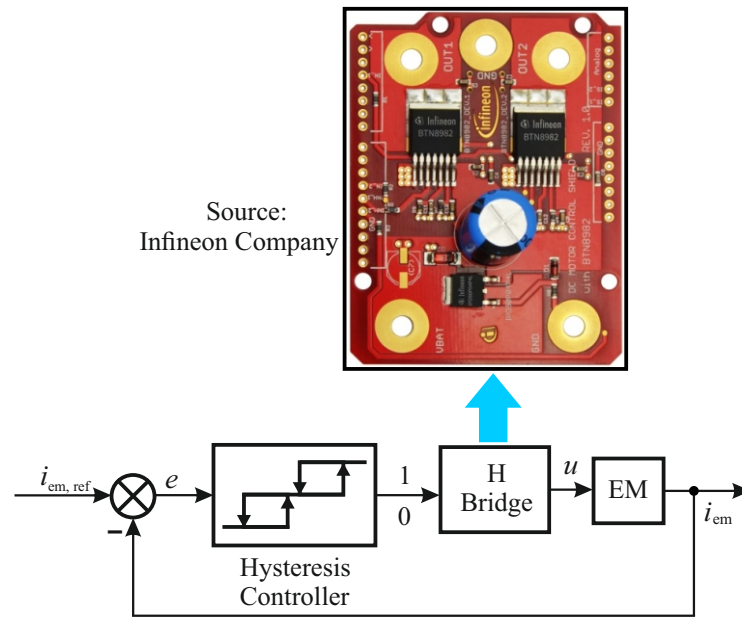


Figure 4.10.: The current control for electromagnet.

and

$$L \frac{di_m}{dt} + Ri_m + K_e \dot{\theta}_1 = U, \quad (4.25)$$

where  $M_d$  is the output torque of the DC motor, namely, the disturbance torque as mentioned in Eq. (4.6) and Eq. (4.7).  $R$ ,  $L$ ,  $K_t$ ,  $K_e$  are the moment of inertia of the motors rotor, electric resistance, electric inductance, torque constant, and electromotive force constant, respectively. In order to obtain the needed torque, a current PI control for the DC motor is applied as shown in Fig. 4.11, where  $i_{m,ref}$  is the demand current of the DC motor and decided by the reference disturbance torque  $M_{d,ref}$ . Here Motor Model 1, marked in Fig. 4.11 is  $1/K_t$  according to Eq. (4.24). Meanwhile, a model-based voltage feed forward control is added to speed up system response and decrease the steady state error as well. Due to the angular velocity of the primary plate,  $\dot{\theta}_1$  being very low, Motor Model 2 only consists of the electric resistance  $R$  according to Eq. (4.25).

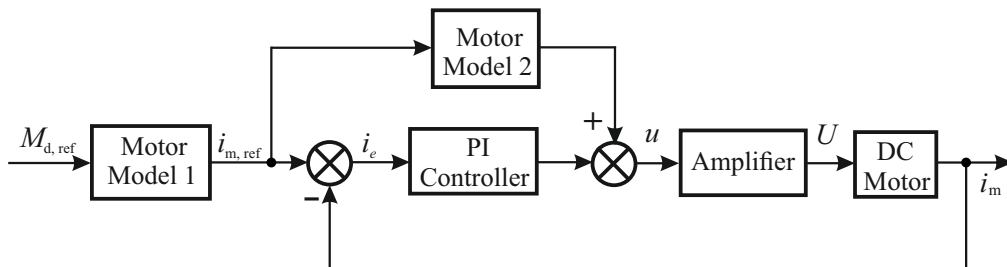


Figure 4.11.: Current control for the used DC motor.

### 4.3.3. Lumped System

The lumped system consists of a Mechanical Unit, Velocity Zero-crossing Decision Unit, Current Control for DC Motor Unit, and Current Control for Electromagnet Unit, as shown in Fig. 4.12. A specified disturbance torque  $M_d$  is exerted on the mechanical unit, which responds accordingly to the proposed velocity zero-crossing switching law. Depending on the state variable  $\dot{\theta}_1$  feedback control information, the switching control vector  $\mathbf{S}$  will govern the power on-off state of two electromagnets. This allows the bidirectional electromagnetic switch, as shown in Fig. 4.9, to connect or disconnect two spiral springs to the primary plate. By means of such a system, vibration reduction performance and vibration energy harvesting can be realized.

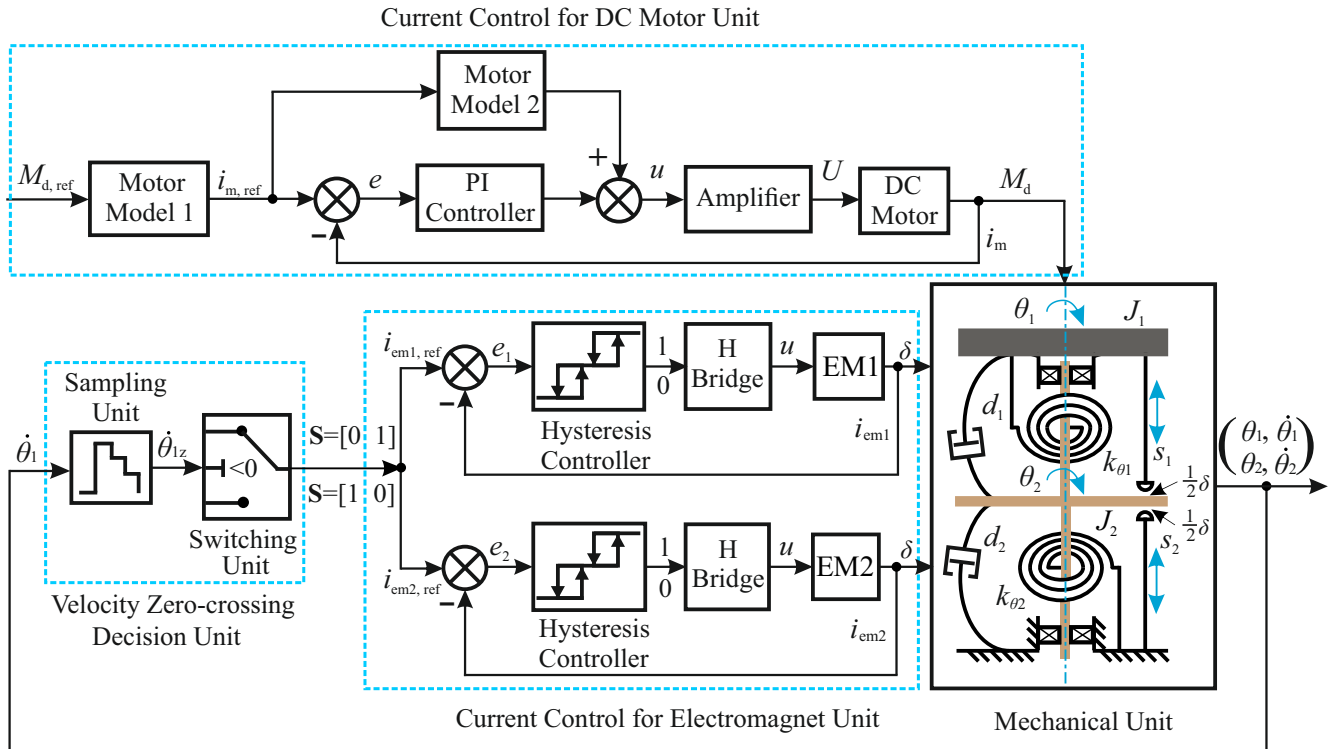


Figure 4.12.: Schematic for the lumped controlled rotational test rig.

## 4.4. Experiment

In this section, the experiments to validate the vibration energy harvesting and vibration reduction performance of the proposed system are executed using the design parameters listed in Table. 4.1. The rotational stiffness of two spiral springs,  $k_{\theta 1}$  and  $k_{\theta 2}$  are considered to be equal based on the data sheet from the company (Gebr. Schmidt Federnspezialfabrik GmbH). In fact, these two springs are not the same, as will be formulated in the following subsection. The maximum torque for one spiral spring  $M_{k_{max}}$  can be calculated according to Eq. (4.23). This will limit the maximum rotation angle of the primary plate. The maximum clamping torque  $M_c$  represents the working



ability of the bidirectional electromagnetic switch and determines the vibration energy harvesting level. The maximum vibration energy harvesting level should be lower than half of  $M_c$  in order to obtain a reliable attraction between the electromagnet-plate and armature-shaft according to Eq. (4.15). The frictional torque of the bearings,  $M_b$  is provided by SKF, 2200 ETN9 and the maximum disturbance torque produced by a DC motor is also provided by Maxon Motor GmbH, DCX32L. According to Eq. (2.38),

Table 4.1.: System Design Parameters.

Name	Symbol	Value	Unit
Moment of inertia of the primary plate	$J_1$	0.121	$\text{kg} \cdot \text{m}^2$
Moment of inertia of the armature-shaft	$J_2$	0.008	$\text{kg} \cdot \text{m}^2$
Stiffness of spiral spring	$k_\theta$	0.12	$\text{Nm}/\text{rad}$
Frictional torque of bearing	$M_b$	0.008	$\text{Nm}$
Max. torque of spiral spring	$M_{k\max}$	0.677	$\text{Nm}$
Max. clamping torque	$M_c$	1.85	$\text{Nm}$
Max. disturbance torque	$M_{d\max}$	0.1	$\text{Nm}$
Dimensionless frequency of the disturbance	$\eta_d$	variable	-
Dimensionless sampling frequency	$\eta_s$	variable	-

the switching law for the rotational test rig can be given by

$$\mathbf{S}(t) = \begin{cases} [1, 0] & \text{if } \dot{\theta}_{1z} \geq 0 \\ [0, 1] & \text{if } \dot{\theta}_{1z} < 0 \end{cases}, \quad (4.26)$$

and

$$k(t) = \begin{cases} k_{\theta 1} & \text{if } \dot{\theta}_{1z} \geq 0 \\ k_{\theta 2} & \text{if } \dot{\theta}_{1z} < 0 \end{cases}, \quad (4.27)$$

with the use of the zero-order-hold function of angular velocity Eq. (4.28)

$$\dot{\theta}_{1z}(\dot{\theta}_1, T_s) = \sum_{n=0}^{\infty} \dot{\theta}_1(nT_s) [\sigma(t - nT_s) - \sigma(t - (n+1)T_s)], \quad n \in \mathbb{N}, \quad (4.28)$$

or

$$\dot{\theta}_{1z}(t, T_s) = \dot{\theta}_1(nT_s), \quad n \in \mathbb{N}, \quad nT_s \leq t < (n+1)T_s, \quad (4.29)$$

where  $T_s$  is the sampling period of the controller, and  $\sigma(t)$  is the unit step function. In order to determine the sampling period  $T_s$ , the natural frequency  $\omega_0$  of each subsystem should be determined according to Eq. (2.51). This switching law will be tested. In the following sections system parameter identification is initially executed.

#### 4.4.1. System Parameter Identification

The current control for a DC motor is tested and as an example, a desired harmonic disturbance torque,

$$M_d(t) = K_t \hat{i}_m \sin(\Omega t) = \hat{M}_d \sin(\Omega t). \quad (4.30)$$

is applied as shown in Fig 4.13, where  $K_t$  is the torque constant of the DC motor,  $K_t = 0.0585$  Nm/A and the current of the motor  $i_m$  is measured. Here the DC motor is connected to the primary plate and they rotate together. It is not difficult to see that the current controller allows the real-time current to track the reference current well and this can be further used for other experiments.

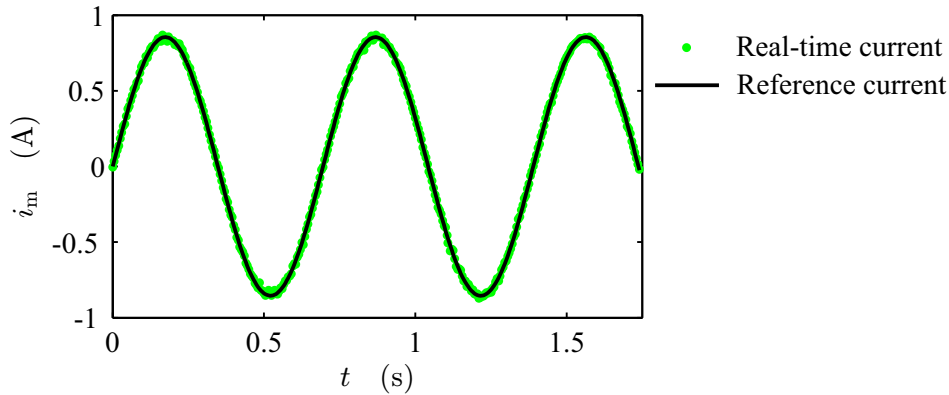


Figure 4.13.: Example for the current control of the DC motor.

In order to determine the natural frequency of each subsystem  $\omega_0$ , according to Eq. (2.21) and further set the sampling frequency  $\omega_s$  of the controller accurately, the system parameters such as system stiffness and damping are first identified. In fact, two subsystems in experimental analysis, denoted by  $J_1-k_{\theta_1}$  and  $(J_1 + J_2)-k_{\theta_2}$ , are not the same as in the theory analysis,  $m_1-k$ , due to two stiffness being equal,  $k_1 = k_2 = k$ , and the connection point mass  $m_2$  being neglected. Considering there might exist viscous damping such as air damping and Coulomb friction torque around the bearings and sensors, the hysteresis relationship between the driving torque  $M_d$  and the rotation angle  $\theta_1$  of the primary plate is investigated. The results are shown by red points in Fig. 4.14(a) and Fig. 4.15(a), where three cycles of rotation for the primary plate in each figure are carried out. Here  $\hat{i} = 1.5$  A,  $\Omega = 0.11$  rad/s, in order to reach a quasi static state measurement.

Fig. 4.14(a) shows the results, when spring 1 is active. In this case only the primary plate rotates and the system moment of inertia is  $J_1$ . To solve system stiffness, two sets of data, denoted by blue and cyan points, standing for two different rotation directions, are used for linear regression. The regression lines are denoted by black lines are shown and demonstrate the linear relationship between the driving torque, namely, the disturbance torque  $M_d$  as mentioned in Subsection 4.2.2, and the rotation angle  $\theta_1$ . As shown in Fig. 4.14(a), the upper and lower fitting lines are expressed by

$$M_d = 0.1513\theta_1 + 0.0109, \quad \text{and} \quad M_d = 0.1489\theta_1 - 0.0065. \quad (4.31)$$

As such, the mean value of the stiffness  $k_{\theta_1}$  according to Eq. (4.31) is taken as  $(0.1513+0.1489)/2 \approx 0.15$  Nm/rad and the Coulomb friction torque  $M_{fcl}$ , as mentioned in Subsection 4.2.2, is  $(0.0109 - (-0.0065))/2 = 0.0087$  Nm. In order to obtain the viscous damping  $d_1$  of the subsystem  $J_1-k_{\theta_1}$ , a numerical simulation considering Coulomb friction and viscous damping is executed in MATLAB/Simulink and the results are shown in Fig. 4.14(b), where the system responds under non-zero initial conditions.

In order to match the experiment, the viscous damping ratio  $D_1$ ,  $D_1 = d_1/2\sqrt{k_{\theta_1}J_1}$  in modeling is changed step by step, until both of them agree well, and  $D_1$  is set to 0.023.

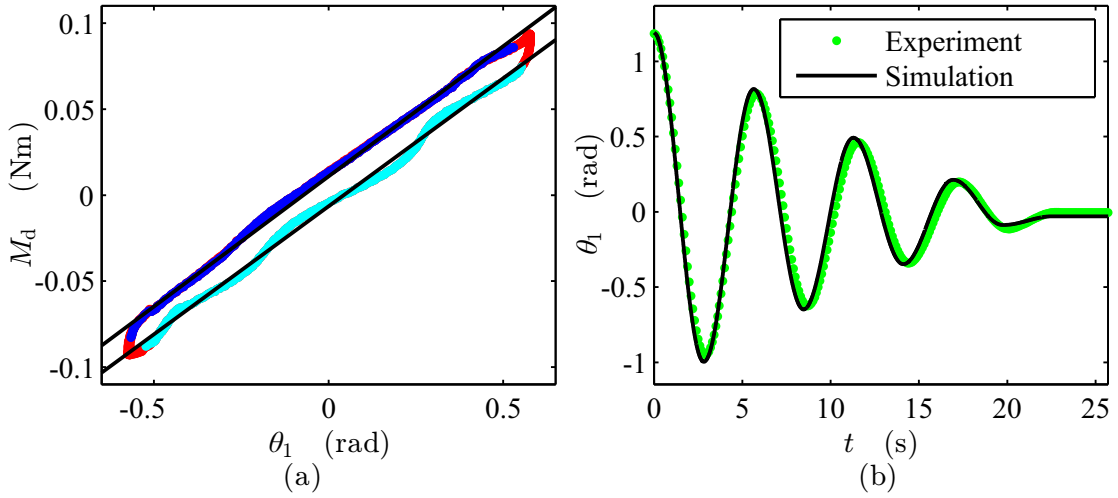


Figure 4.14.: System identification when spring 1 is active. (a) The hysteresis relationship between the output torque of motor and the rotation angle of primary plate; (b) System response under a non-zero initial position.

Fig. 4.15(a) shows the system identification results when spring 2 is active, namely, the primary plate and armature-shaft rotate together,  $\theta_1 = \theta_2$ . It is related to subsystem

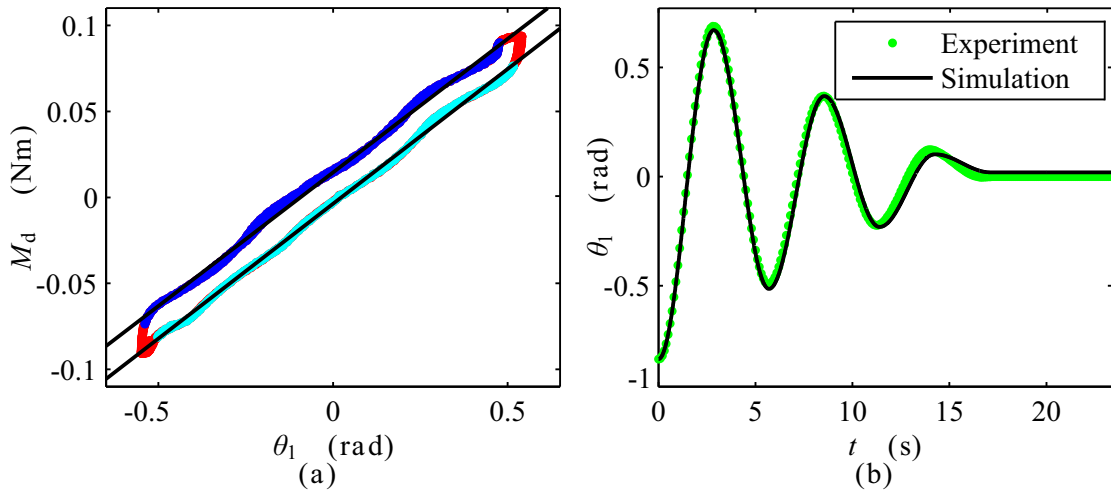


Figure 4.15.: System identification when spring 2 is active. (a) The hysteresis relationship between the output torque of motor and the rotation angle of primary plate; (b) System response under a non-zero initial position.

2, denoted by  $(J_1 + J_2)k_{\theta_1}$ . The fitting lines can be expressed by

$$M_d = 0.1567\theta_1 + 0.0146, \quad M_d = 0.1553\theta_1 - 0.0037. \quad (4.32)$$

Similar to the analysis for subsystem 1, the mean value of the stiffness  $k_{\theta 2}$  is taken as 0.156 Nm/rad and the Coulomb friction torque is set to 0.0092 Nm. The numerical analysis is also finished and the fitting viscous damping ratio  $D_2$ ,  $D_2 = d_2/2\sqrt{k_{\theta 2}(J_1 + J_2)}$ , equals to 0.02.

The system parameter identification is summarized in Table. 4.2. Here  $T_{\text{dsim}}$  is the natural period of the damped subsystems,  $J_1-k_{\theta 1}-d_1$  and  $(J_1 + J_2)-k_{\theta 2}-d_2$ , for the simulation analysis and  $T_{\text{dexp}}$  for the experiment as shown in Fig. 4.14(b) and Fig. 4.15(b). Here the stiffness of two springs slightly differ from the theoretical calculation results listed in Table 4.1. The error between the simulation and experimental damped natural period,  $T_{\text{dsim}}$  and  $T_{\text{dexp}}$ , is low and the system identification parameters can be further applied for other experiment analysis. The sampling period  $T_s$  or sampling frequency  $\omega_s$  of the controller can be determined, according to

$$\omega_s = \eta_s \omega_0 , \quad (4.33)$$

where  $\eta_s$  is set to 100 in experiment, not 1000 as in the theoretical analysis, considering the switching delay  $t_d$  of a mechanical switch. The natural frequency  $\omega_{01}$  of the undamped subsystem 1,  $J_1-k_{\theta 1}$ , is equal to 1.113 rad/s according to Eq. (4.11). As such, the sampling frequency  $\omega_s$  is set be 111.3 rad/s and the sampling time  $T_s$  is approximately equal to 56.45 ms.

Table 4.2.: System Identification Results.

System	$k_{\theta}$ (Nm/rad)	$D$	$M_{fc}$ (Nm)	$T_{\text{dsim}}$ (s)	$T_{\text{dexp}}$ (s)	Error(%)
Subsystem 1	0.15	0.023	0.0087	5.7	5.624	1.34
Subsystem 2	0.156	0.02	0.0092	5.57	5.699	2.32

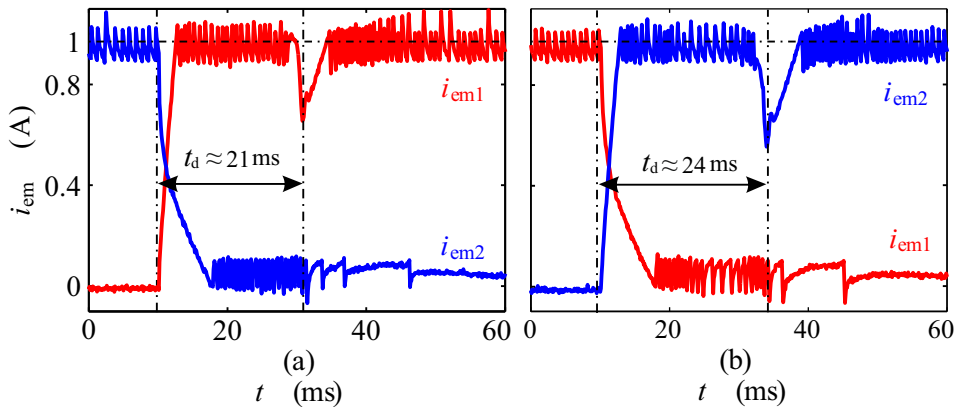


Figure 4.16.: Switching time with respect to current of two electromagnets,  $i_{\text{em}}$ . (a) Electromagnet 1 is powered on and electromagnet 2 is powered off; (b) Electromagnet 1 is powered off and electromagnet 2 is powered on.

In order to evaluate switching time of a mechanical switch, the current applied to the two electromagnets is measured as depicted in Fig. 4.16 and a correspondingly controlled supply voltage measurement is shown in B.2. Subfigure (a) shows that at

beginning the current  $i_{em1}$  of electromagnet 1, denoted by red line, increases slowly due to coils inductance and then goes into an oscillation state responding to the current control strategy as depicted in Fig. 4.10, which is a property of a switching power electronics and the mean value of the oscillating current is close to a reference current of 1 A. After an oscillation duration the current  $i_{em1}$  falls off because motion of armature will change the electromotive force, which results in a current decrease until the armature and electromagnet are tightly attracted together according to Eq.( 4.19). Therefore, the time span as chosen by two dot-dashed lines can be taken as switching time of the mechanical switch. From subfigure(a) and (b), the switching time of two mechanical switches, or in other words, switching delay  $t_d$  is 21 ms and 24 ms, respectively. It is obviously larger than the motion time of armature  $t_{motion}$ , which does not consider the settling time of electronics and the effect of eddy current in an electromagnet. Of course, this is lower than the chosen sampling time 56.45 ms. This is beneficial for an accurate stiffness switching. It means that 4S is able to achieve a stiffness switching in one sampling period and further experiments can be executed.

#### 4.4.2. Step Response

In this section, the velocity zero-crossing switching law, according to Eq. (4.27), would be experimentally validated.

First, the step response of the experimental setup is executed. Considering the nominal output torque of the used DC motor, a step torque,  $M_d = 0.0585$  Nm, namely,  $i_m = 1$  A, is applied as shown in Fig. 4.17. The sampling frequency  $\eta_s$  is initially set to be 100 and the other experiment parameters are shown in Table 4.1. Here the static deflection is defined as  $\hat{M}_d/k_\theta = 0.0585/0.15 = 0.39$  rad. The experiment and simulation results are shown in Fig. 4.18. Note, that before the step torque is exerted on 4S, the system has begun to switch. Because at beginning  $\theta_1 = 0$ , the switching law Eq. (2.38) leads to the attraction between electromagnet-plate 2 and base. This will result in a slight shaking of the primary plate and therefore an extremely low amplitude chattering occurs in system. Thus, the initial position and velocity,  $\theta_1(0)$ ,  $\dot{\theta}_1(0)$  and  $\theta_2(0)$ ,  $\dot{\theta}_2(0)$ , can only be approximately equal to zero. This will be slightly adjusted in the simulation model to match the experiment.

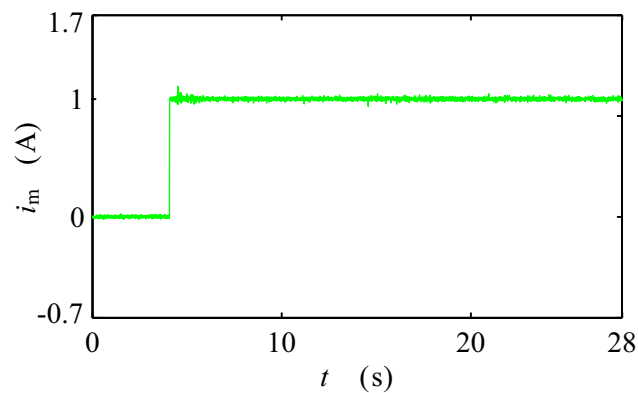


Figure 4.17.: The step torque exerted on 4S test rig.

Neither like a passive undamped SDOF system nor a passive underdamped one, 4S performs without overshoot and oscillation, but the angular displacement of the primary plate  $\theta_1$  always increases with the deformation of spring 2 denoted by  $u_2$ . The deformation of spring 2 is positive,  $u_2 > 0$ , differing from the desired working principle, in which spring 2 should be compressed,  $u_2 < 0$ . This is because the external disturbance  $M_d$  is positive and large enough such that the primary plate always moves in the positive direction, even if working in the stiffness 2 state. Due to viscous damping and Coulomb damping existing in 4S, the deformation of spring 1,  $u_1$  does not reach the maximum deformation of  $2M_d/k_{\theta_1}$  like a passive undamped SDOF system. Considering the experimental errors, the results can be reasonably accepted.

In order to avoid the risk of 4S failing due a long time operation, the experiment is not carried out for a long time, but the simulation is executed as depicted in Fig. 4.19. Fig. 4.19(b) shows detail from Fig. 4.19(a), marked by the orange rectangular frame at  $t = 100$  s. It is obvious to see that the primary plate always rotates in a positive

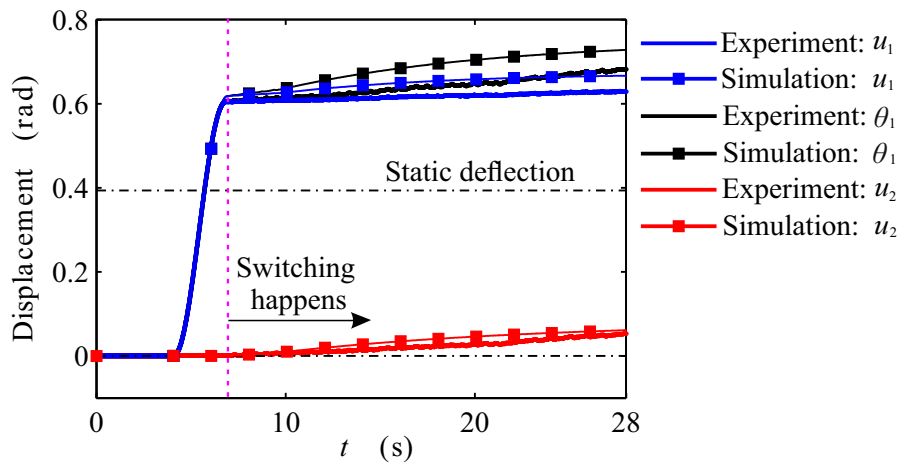


Figure 4.18.: Step response of 4S:  $\hat{M}_d = 0.0585$  Nm,  $\eta_d = 0$  and  $\eta_s = 100$ .

direction denoted by the increasing angular position  $\theta_1$ . It starts to rotate in subsystem 1,  $J_1-k_{\theta_1}-d_1$  and then reaches a peak level quickly at half of a damped natural period,  $T_d/2$ . Afterwards, due to the deformation of spring 2,  $u_2$ , being extremely low as shown in Fig. 4.18, and a large constant positive disturbance torque  $M_d$ , as denoted by the motors current  $i_m$  in Fig. 4.17, the angular velocity of the primary plate  $\dot{\theta}_1$  at this switching time instant, where the primary plate moves in stiffness 1 state, is so large that the deformation of spring 1 still increases. This will last until  $t \approx 35$  s, where the deformation of spring 1,  $u_1$ , reaches a maximum, as marked by pink dashed line in Fig. 4.19(b). Meanwhile, the disturbance torque also results in the increase of  $u_2$ . The increasing  $u_2$  causes the velocity and kinetic energy of the primary plate to decrease at the above mentioned switching time instant. Consequently, the released quantity of stored potential energy in spring 1 will be larger than the harvested quantity of kinetic energy in the following stiffness 1 state. But in spring 2 the harvested kinetic energy is larger than the released potential energy. Finally,  $u_1$  starts to decrease and  $u_2$  still increases after  $t \approx 35$  s. This continues until steady stat is reached: the kinetic energy at each switching time instant, from stiffness state 1 to 2 or vice versa, are equal, and the energy dissipation due to the system damping can be compensated through

the work of the constant disturbance torque acting on the primary plate. Thus, the potential energy in each spring hardly changes and  $\theta_1$  stays around an equilibrium-like position. Of course, due to the stiffness of two springs not being equal,  $k_{\theta_1} \neq k_{\theta_2}$ , as listed in Table 4.2, the final deformations of two springs are not the same,  $u_1 \neq u_2$ .

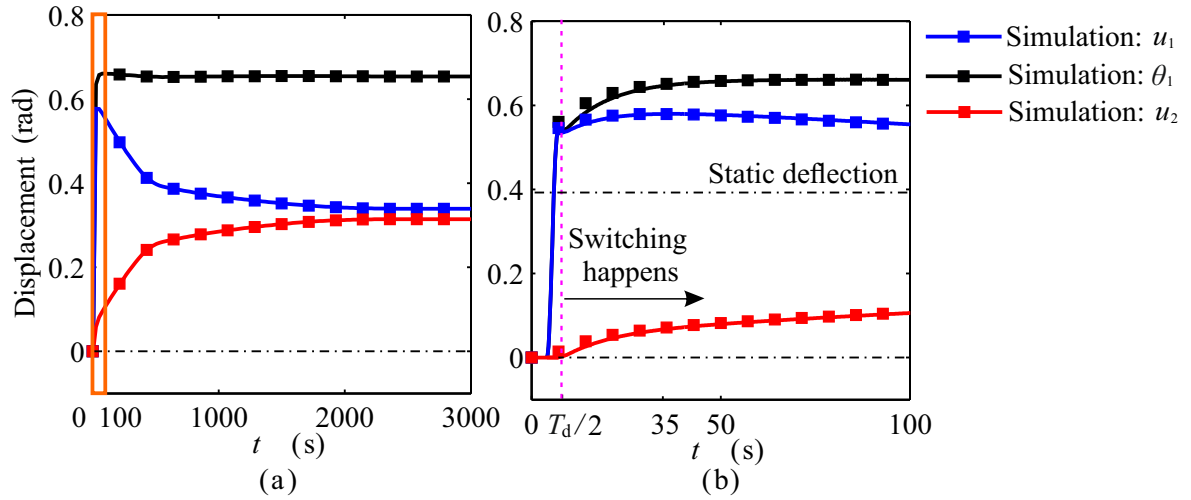


Figure 4.19.: Simulation for step response of 4S. (a) Lumped long time simulation; (b) Partly zoomed-in picture for (a).

### 4.4.3. Harmonic Response

The proposed vibration control system shows vibration energy harvesting and vibration reduction performance under a harmonic disturbance in the above mentioned theory in chapter 2. Here a harmonic disturbance torque according to Eq. (4.30) is exerted on the primary plate, corresponding to  $F$  in Fig. 4.1(a). The experiment and simulation results are shown in Fig. 4.20, where the vertical axis stands for different displacements including the position of the primary plate  $\theta_1$ , the deformation of spring 1,  $u_1$  and the deformation of spring 2,  $u_2$ , and the horizontal axis for the time history. Here the static deflection is defined as  $\hat{M}_d/k_\theta = 0.05/0.15 = 0.33$  rad. It is clear to see that the deformations of the two springs increase positively and negatively. This means that potential energy is stored into two springs. The experiment and simulation match well in the beginning but a slight difference occurs with the increase of time. This is reasonable, because some switching decision errors due to the delay of the electromagnetic switch, as denoted by  $t_{\text{set}}$ , occur in experiment. This would enlarge the system response difference. What's more, the primary plate stays around a non-zero equilibrium-like position, because the system lacks a position feedback control and only the velocity is considered according to Eq. (2.38).

#### Different disturbances

In order to test how an external disturbance affects the system response, different disturbance frequencies,  $\eta_d$  and disturbance amplitudes,  $\hat{M}_d$  are set, and the resulting

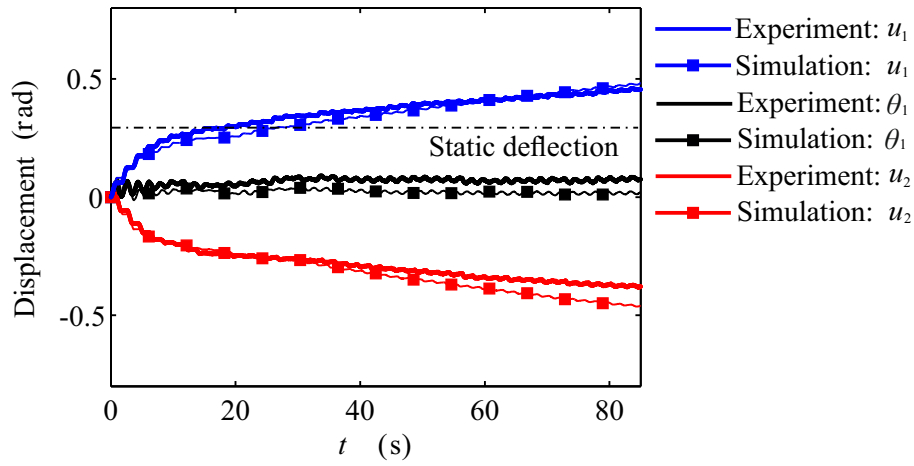


Figure 4.20.: System response under a harmonic excitation:  $\hat{M}_d = 0.05$  Nm,  $\eta_d = 3$  and  $\eta_s = 100$ .

experiment and simulation results are shown in Fig. 4.21 - Fig. 4.24.

Fig. 4.21 show the experiment results for the system response under different disturbance frequencies. Here the static deflection is defined as  $\hat{M}_d/k_\theta = 0.05/0.15 = 0.33$  rad. It is obvious to see that 4S is able to harvest kinetic energy and show vibration reduction performance under different disturbance frequencies. However, the system response under a lower frequency disturbance,  $\eta_d < 1$ , shows a high oscillation amplitude, because a lower frequency disturbance would dominate the fundamental frequency term of system response. A higher frequency disturbance,  $\eta_d > 1$ , enables more frequent switching and results in a much smoother system response profile. Meanwhile, a higher frequency disturbance leads to a lower deformation of two springs, namely, a lower stored potential energy. This can be explained on the basis of the low-pass filtering property of second-order system.

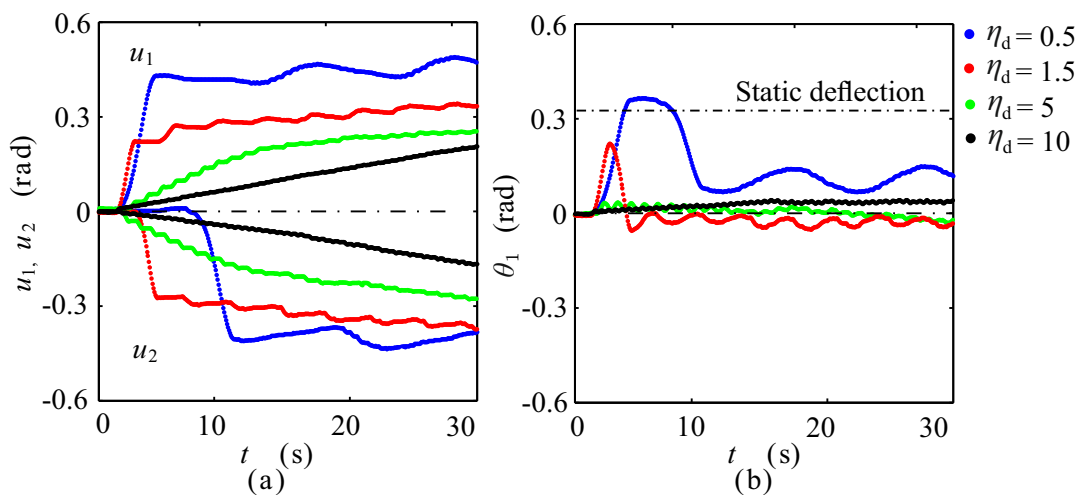


Figure 4.21.: Experimental results of the system response under different harmonic disturbance frequencies  $\eta_d$ :  $\hat{M}_d = 0.05$  Nm and  $\eta_s = 100$ .



The simulation results are depicted in Fig. 4.22 and match well with the experimental results. For the angular displacement of the primary plate  $\theta_1$ , there exists little difference owing to the stiffness variation in experiment.

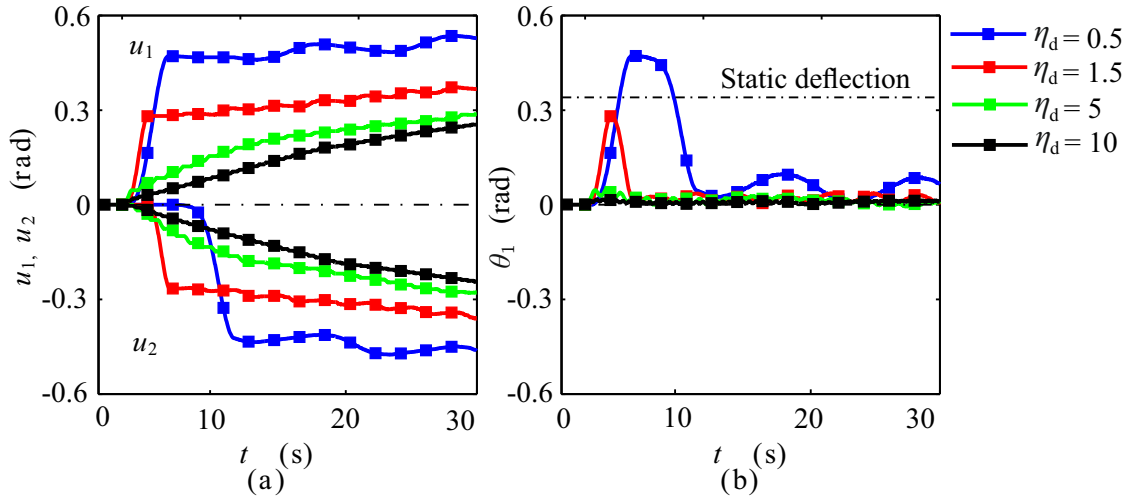


Figure 4.22.: Simulation of the system response under different harmonic disturbance frequencies  $\eta_d$ :  $\hat{M}_d = 0.05$  Nm and  $\eta_s = 100$ .

Fig. 4.23 shows the experimental results for the system response under different disturbance amplitudes. Obviously, the vibration energy harvesting increases with the disturbance torque amplitude  $\hat{M}_d$  as depicted in Fig. 4.23(a), because the mechanical power of the disturbance torque to 4S increases, but the primary plate always keeps a similar equilibrium-like position under different disturbance amplitudes as shown in Fig. 4.23(b). Note that there exists a large difference between experiment and sim-

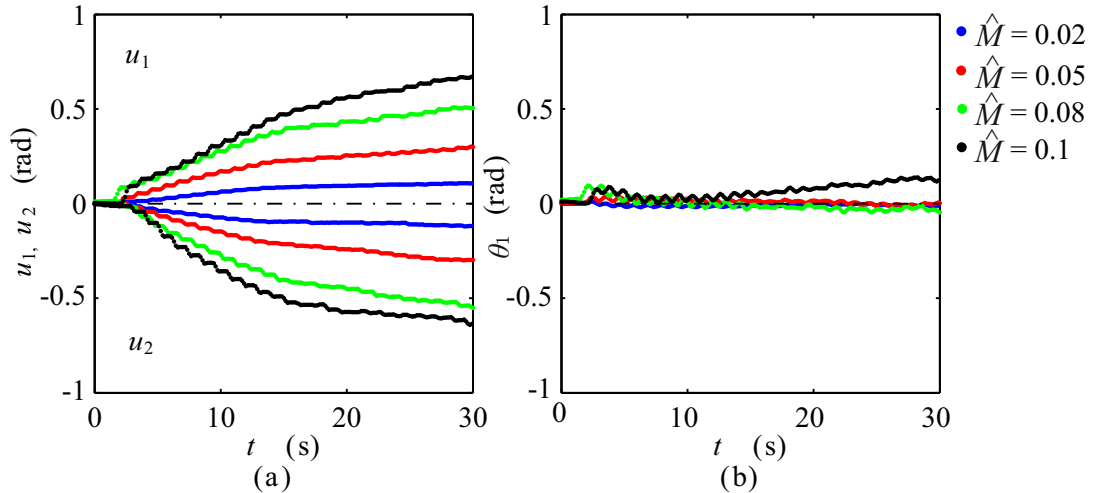


Figure 4.23.: Experimental results for the system response under different harmonic disturbance amplitudes  $\hat{M}_d$ :  $\eta_s = 100$  and  $\eta_d = 5$ .

ulation results, when  $\hat{M}_d = 0.1$ . Because when the deformations of two springs are large, the outside of spiral springs unavoidably touches the wall of the housing as

shown in Fig. 4.8. This changes the stiffness of one spiral spring and further affects the deformation of the two springs and the angular displacement of the primary plate.

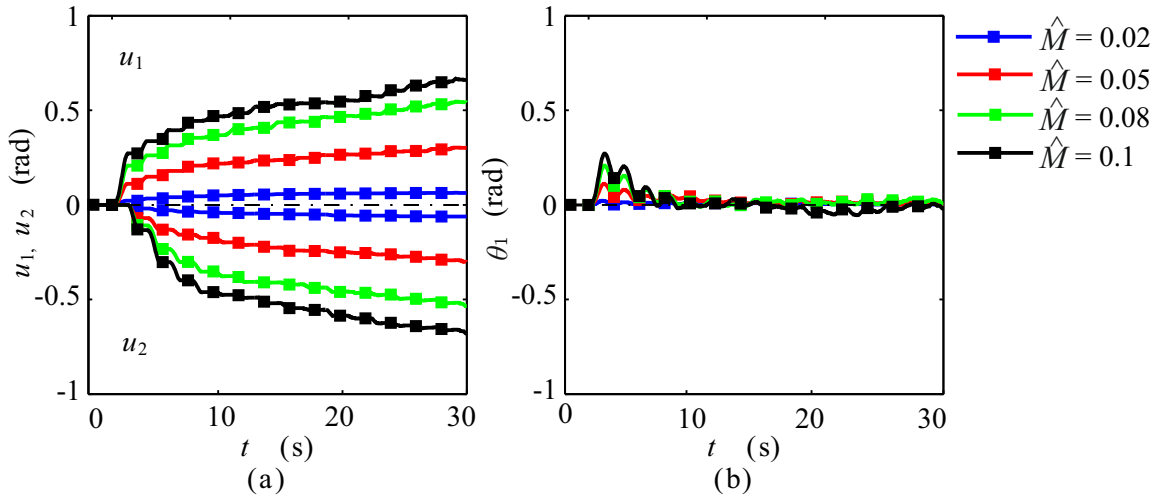


Figure 4.24.: Simulation results for the system response under different harmonic disturbance amplitudes  $\hat{M}_d$ :  $\eta_s = 100$  and  $\eta_d = 5$ .

### Different sampling frequencies

As mentioned before, the sampling frequency  $\omega_s$  affects the switching decision error between two springs as depicted in Fig. 2.7 and further affects the system response. Thus, different sampling frequencies are applied here. The experiment and simulation results are shown in Fig. 4.25 and Fig. 4.26. It clearly shows that an extremely low

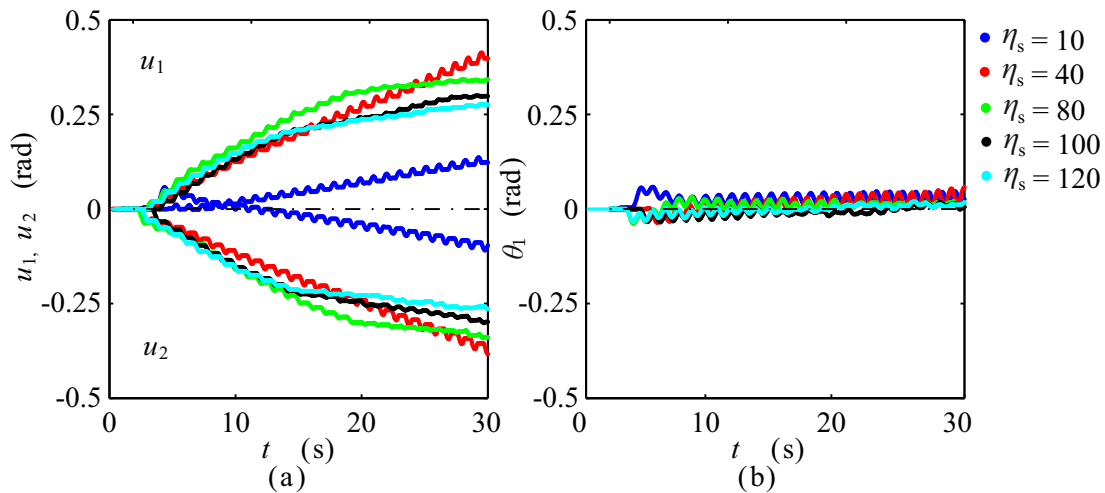


Figure 4.25.: Experimental results for the system response under different sampling frequencies  $\eta_s$ :  $\hat{M}_d = 0.05$  and  $\eta_d = 5$ .

sampling frequency,  $\eta_s = 10$ , lowers the energy harvesting level and results in a larger

amplitude oscillation as well, because low sampling frequency increases the switching decision error and the disturbance torque  $M_d$  will dominate system response. With the increase of the sampling frequency, the stored potential energy increases. When the sampling frequency is large enough, the switching decision error is much lower, namely, the angular velocity of the primary plate would always stay close to zero. This results in a low mechanical power of the disturbance torque  $M_d$  to the system. The stored potential energy increases slowly with the sampling frequency. Meanwhile, the system response shows up a low amplitude oscillation around an equilibrium-like position under a high sampling frequency as shown in Fig. 4.25(b), because the forced vibration disappear under a high sampling frequency, for example,  $\eta_s = 120$ . Additionally, the experiment and simulation match well.

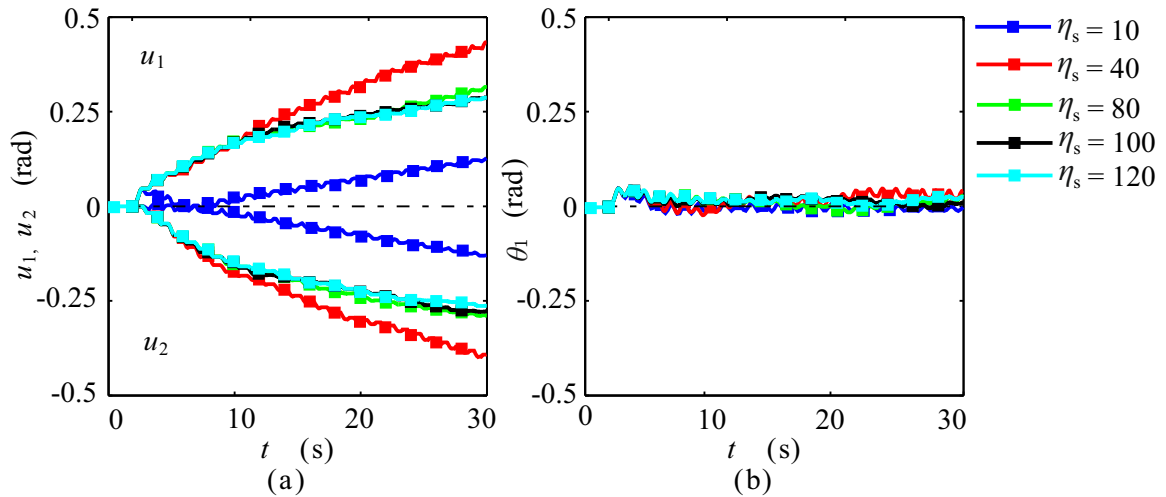


Figure 4.26.: Simulation results for the system response under different sampling frequencies  $\eta_s$ :  $\hat{M}_d = 0.05$  and  $\eta_d = 5$ .



---

## Improved Switching Law for 4S

---

### 5.1. Introduction

Harmonic excitation as an external disturbance is tested on 4S in the aforementioned chapters and 4S shows vibration energy harvesting and vibration reduction performance based on the velocity zero-crossing switching law. Apart from a harmonic disturbance, nonzero initial velocity, in other words, a shock excitation can be also seen to be an external disturbance. How 4S responds to a nonzero initial velocity disturbance will be discussed in this chapter.

Based on the variable structure characteristic of 4S and phase plane, a new switching law is introduced to accelerate the transformation of initial vibration energy into potential energy between two springs and improve the vibration reduction performance. This switching law is numerically and experimentally verified. What's more, due to the introduction of position feedback in this switching law, 4S can reach a better equilibrium-like position even under a harmonic excitation.

### 5.2. Nonzero Initial Velocity Problem for 4S

Vibration control as understood here is to reduce the vibration produced by a nonzero initial velocity as shown in Fig. 5.1(a). In order to state the problem and make the comparison between the simulation analysis and the following experiment, the initial conditions in experiment are applied to the simulation analysis in advance. Meanwhile, several model parameters are also modified to agree with the aforementioned theory analysis. Here the stiffness of two spiral springs are seen to be the same, namely,  $k_{\theta 1} = k_{\theta 2} = k_{\theta} = 0.15 \text{ Nm/rad}$ . Similar to a massless connection point in the translational model, the moment of inertia of the armature-shaft,  $J_2$ , is neglected. The damping,

Table 5.1.: Simulation parameters for nonzero initial velocity problem analysis.

Name	Value	Unit	Name	Value	Unit	Name	Value	Unit
$\hat{M}_d$	0	Nm	$\eta_d$	0	-	$\theta_1(0)$	-1.75	rad/s
$J_1$	0.121	$\text{kg} \cdot \text{m}^2$	$\eta_s$	100	-	$\theta_2(0)$	0	rad
$k_\theta$	0.15	Nm/rad	$\theta_1(0)$	0	rad	$\dot{\theta}_2(0)$	0	rad/s

including viscous damping  $M_{fv}$  and Coulomb damping  $M_{fc}$  are also initially neglected. The other simulation parameters are listed in Table 5.1 and the results are shown in Fig. 5.1(b).

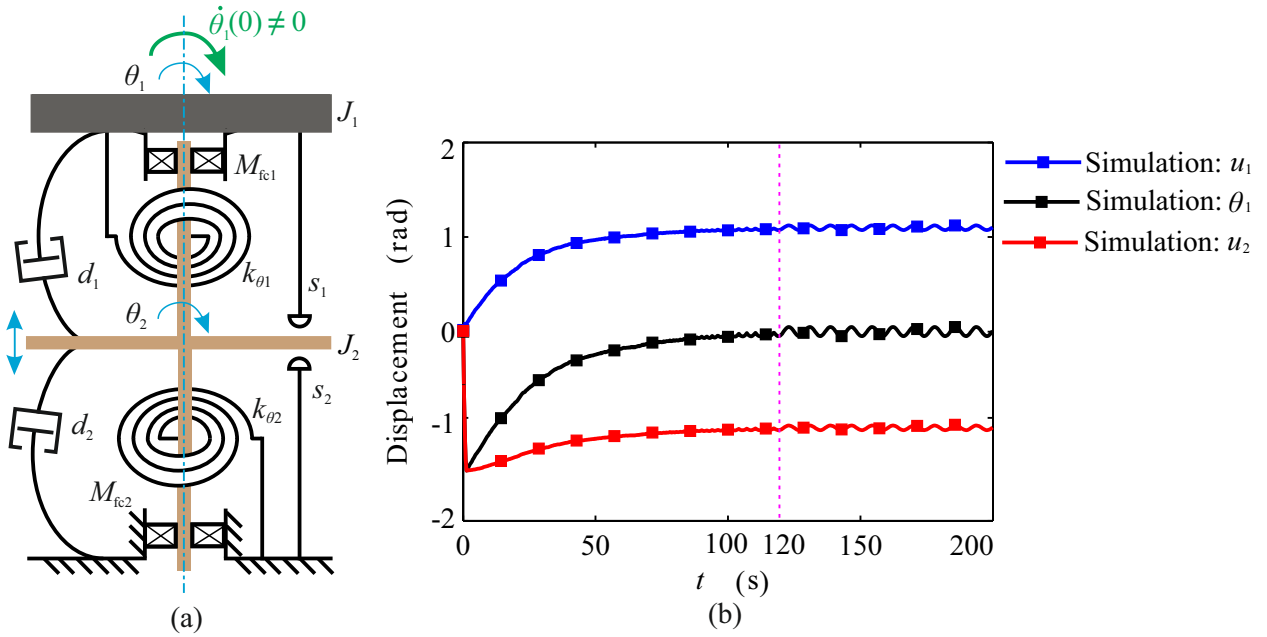


Figure 5.1.: Numerical analysis for the system response under nonzero initial velocity  $\dot{\theta}_1(0) = -1.75$  rad/s, here  $\eta_s = 100$ . (a) Simplified rotational model; (b) Simulation results.

A nonzero initial velocity condition means that the system has a certain amount of kinetic energy  $T$  at the initial time instant. Due to a negative angular velocity of the primary plate at the initial time instant, according to the velocity zero-crossing switching law Eq. (4.27), spiral spring 2,  $k_{\theta 2}$ , is active initially and reaches negative maximum quickly,  $u_2$ , as denoted by the red line in Fig. 5.1(b). Afterwards, the deformation of spring 1,  $u_1$  increases and the deformation of spring 2,  $u_2$  decreases, until the system goes into a steady state and the initial kinetic energy is transformed into potential energy equally stored into two spiral springs. Due to sampling frequency  $\eta_s$  not being large enough, here  $\eta_s = 100$ , unlike that in the previously mentioned theory analysis,  $\eta_s = 1000$ , a large amplitude oscillation happens in steady state. This phenomena has been explained in Subsection 4.4.3. The increasing deformations of the two springs represent that 4S are still able to harvest vibration energy and transform the initial kinetic energy into potential energy stored in two springs. Although the

velocity zero-crossing switching law allows 4S to reduce vibration and remain at an equilibrium-like position, this needs a long settling time, here  $t \approx 120$  s as marked by the pink dotted line. How to reduce the settling time will be discussed in this chapter.

## 5.3. Variable Structure System Control for 4S

A variable structure system (VSS) consists of a group of continuous subsystems and a suitable switching law. These subsystems will be in an active mode or not, dependent on the switching law. A distinguishing feature of VSS control is its ability to result in a very robust control system. An asymptotically variable structure system can be composed of two non-asymptotically stable subsystems, see [125, 126]. In fact, 4S with a velocity zero-crossing switching law is a variable structure system consisting of two continuous subsystems,  $m_1-k_1$  and  $m_1-k_2$  in a translational model or  $J_1-k_{\theta_1}$  and  $J_1 + J_2-k_{\theta_2}$  in a rotational model, together with a switching surface  $s = \dot{x}_1 = 0$  or  $s = \dot{\theta}_1 = 0$ . The process force  $F_p$  or torque  $M_p$  works as a control input  $u$  and can be modified to

$$F_p(M_p) = u = \begin{cases} u^+ = F_{p1}(M_{p1}) = ku_2 & \text{if } s = \dot{x}_1(\dot{\theta}_1) \geq 0 \\ u^- = F_{p2}(M_{p2}) = ku_1 & \text{if } s = \dot{x}_1(\dot{\theta}_1) < 0 \end{cases} . \quad (5.1)$$

Note, that  $u$  is a control input and  $u_1, u_2$  are the deformations of the two springs. How to combine variable structure control and vibration reduction for 4S will be discussed in the following sections.

### 5.3.1. State Trajectory Analysis

Variable structure system dynamics is generally analyzed by means of phase plane. In order to further study the system response of 4S with the velocity zero-crossing switching law, the phase portrait with respect to the displacement  $\theta_1$  and the velocity  $\dot{\theta}_1$  of the primary plate is shown in Fig. 5.2. Based on the quantitative behavior the state trajectory is divided into four phases, Initial Condition A; Phase B, in which the velocity of the primary plate decreases from maximum to a near-zero value; Phase C, transient chattering state and Phase D, steady chattering state. The state trajectory initially moves from the initial condition A and moves into phase B according to the velocity zero-switching law and then reaches the switching surface  $s = \dot{\theta}_1 = 0$ . Afterwards, the state trajectory will move below and above the switching surface in the transient chattering state, Phase C and finally goes into steady chattering state, Phase D.

As mentioned in the last chapter, 4S is split into two subsystems: Subsystem 1,  $J_1-k_{\theta_1}$  and Subsystem 2,  $(J_1 + J_2)-k_{\theta_2}$ . Here the armature-shaft  $J_2$  and system damping are neglected for a simplified analysis. As a result, the two subsystems are conservative systems and energy balance holds in them. The energy balance in the two subsystems

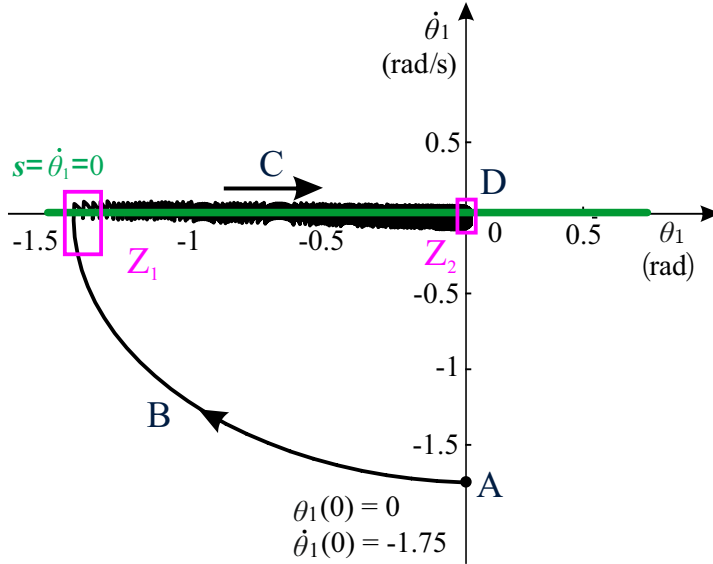


Figure 5.2.: State trajectory representation for nonzero initial velocity excitation.

can be expressed as

$$J_1 - k_{\theta_1} : \quad \dot{\theta}_1^2 + \omega_0 \theta_1^2 = \dot{\theta}_1^2(t_{sw,i}) + \omega_0 u_1^2(t_{sw,i}) \quad (5.2)$$

and

$$J_1 - k_{\theta_2} : \quad \dot{\theta}_1^2 + \omega_0 \theta_1^2 = \dot{\theta}_1^2(t_{sw,i+1}) + \omega_0 u_2^2(t_{sw,i+1}), \quad (5.3)$$

where  $\omega_0 = \sqrt{k_{\theta}/J_1}$  and  $t_{sw,i}$ ,  $t_{sw,i+1}$  are two adjacent switching time instants. The right sides of Eq. (5.2) and Eq. (5.3), consisting of initial kinetic energy terms  $\dot{\theta}_1^2(t_{sw,i})$ ,  $\dot{\theta}_1^2(t_{sw,i+1})$  and potential energy terms  $\omega_0 u_1^2(t_{sw,i})$ ,  $\omega_0 u_2^2(t_{sw,i+1})$  at each switching time instant  $t_{sw,i}$  and  $t_{sw,i+1}$ , will govern the phase portrait in the upcoming active subsystem. In order to show the state trajectory in detail, the transient chattering state, Phase C and the steady chattering state, Phase D are enlarged, marked by  $Z_1$  and  $Z_2$  in Fig 5.2. First, the transient chattering state trajectory is drawn in Fig. 5.3.

The state trajectory starts from Initial Condition A with a negative velocity  $\dot{\theta}_1(0)$  and moves in Subsystem 2, Phase B, according to the velocity zero-crossing switching law. When the primary plate reaches the maximum negative position, namely, the switching surface  $s = \dot{\theta}_1 = 0$ , it will be accelerated in the reverse direction. As a result, the state trajectory moves above the switching surface and goes into Subsystem 1 as marked in Fig. 5.3. Afterwards, the state trajectory stays in the transient chattering state, Phase C. In this time phase, because the deformation of spring 2,  $u_2$  is much larger than that of spring 1,  $u_1$ , the transition velocity,  $\dot{\theta}_1(t_{sw,i+1})$ , when the state trajectory moves into Subsystem 1, is larger than that, when the state trajectory moves into Subsystem 2. As a result,  $u_2$  decreases and  $u_1$  increases, namely, potential energy in subsystem 2 decreases and potential energy in subsystem 1 increases. Thus, the radii of subsystem 2 trajectories (red lines) decrease and the radii of subsystem 1 trajectories (blue lines) increase as shown by the state trajectory numbers 1, 2, 3. This phenomena will last for the time instant, where  $u_1$  and  $u_2$  are equal,  $u_1 = u_{1s}$ ,  $u_2 = u_{2s}$ ,  $u_{1s} = u_{2s}$ , namely, the initial energy is equally divided and stored in the two springs and then 4S goes into



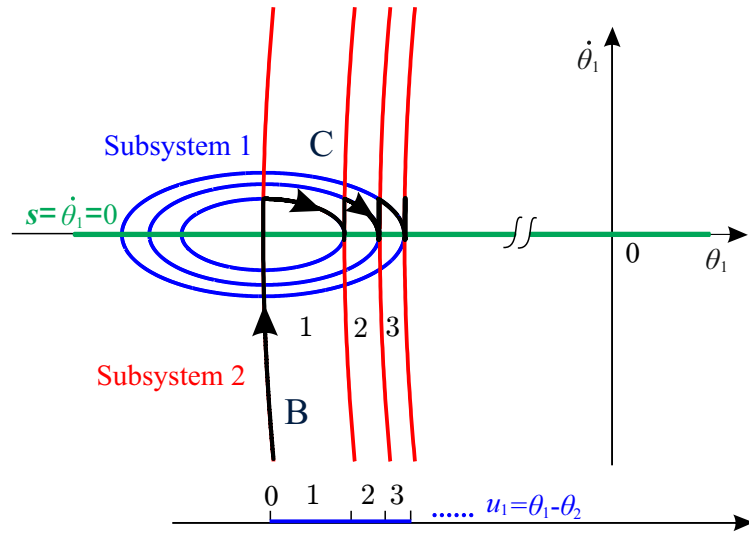


Figure 5.3.: State trajectory representation for transient chattering state.

steady chattering state, Phase D.  $u_{1s}$  and  $u_{2s}$  mean the deformations of two springs in steady chattering state,  $u_{1s} = u_{2s}$ . In steady chattering state, 4S will switch its stiffness state every sampling period  $T_s$  as shown in the zoomed-in picture in Fig. 5.4. In Subsection 2.4.1 a translational model was introduced with a velocity zero-crossing

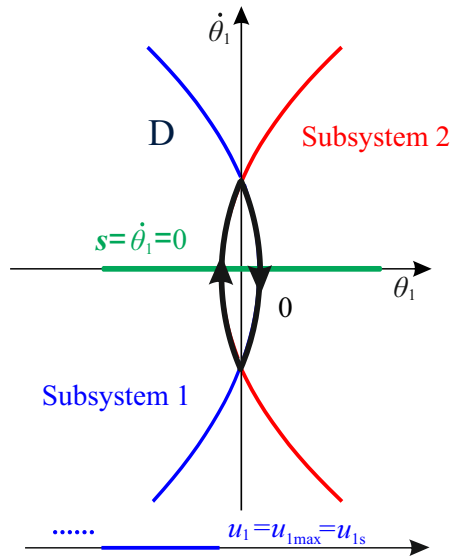


Figure 5.4.: State trajectory representation for steady chattering state.

switching law, see Eq. (2.36)-Eq. (2.37). An equivalent rotational model was presented in Subsection 4.2.2.

$$J_1 \ddot{\theta}_1 + k_\theta \theta_1 = M_d + M_p(\mathbf{S}) \quad (5.4)$$

with

$$\theta_2(\mathbf{S}) = \begin{cases} \theta_2(t_{sw,i}) & \text{if } \mathbf{S}(t) = [1, 0] \\ \theta_1 - [\theta_1(t_{sw,i}) - \theta_2(t_{sw,i})] & \text{if } \mathbf{S}(t) = [0, 1] \end{cases} \quad (5.5)$$

and process torque  $M_p(\mathbf{S})$

$$M_p(\mathbf{S}) = \begin{cases} k_\theta u_2 & \text{if } \mathbf{S} = [1, 0] \\ k_\theta u_1 & \text{if } \mathbf{S} = [0, 1] \end{cases}, \quad u_1 = \theta_1 - \theta_2, \quad u_2 = \theta_2. \quad (5.6)$$

Here, it is assumed that only initial disturbances act on the system, no external forces, namely,  $M_d = 0$ . The velocity zero-crossing switching law to switch between the two process torques  $M_{p1}$  and  $M_{p2}$  is

$$M_p(t) = \begin{cases} M_{p1} = k_\theta u_2 & \text{if } s = \dot{\theta}_1 \geq 0 \\ M_{p2} = k_\theta u_1 & \text{if } s = \dot{\theta}_1 < 0 \end{cases}. \quad (5.7)$$

Considering the sliding mode control stated in Appendix C.1, the switching condition  $s = \dot{\theta}_1$  corresponds to a switching surface  $s$ . Next, it is shown that this is indeed a sliding surface. To do so, it must be shown that  $s \dot{s} < 0$  holds for all states  $(\theta_1, \dot{\theta}_1, \theta_2)$ . It must be distinguished between two cases, either states above the switching surface  $s > 0$  and those below it,  $s < 0$ . In case of  $s = \dot{\theta}_1 > 0$  the necessary condition,  $\dot{s} = \ddot{\theta}_1 < 0$  must hold. The equation of motion reads

$$J_1 \ddot{\theta}_1 + k_\theta \theta_1 = k_\theta \theta_2, \quad \text{and} \quad \theta_2 = \theta_2(t_{\text{sw},i}) \quad (5.8)$$

This results in

$$\ddot{\theta}_1 = -\omega_0^2 (\theta_1 - \theta_2) = -\omega_0^2 u_1. \quad (5.9)$$

Because spring 1 is considered to be extended,  $u_1 > 0$  holds. This gives

$$\ddot{\theta}_1 = -\omega_0^2 u_1 < 0, \quad (5.10)$$

and fulfills the sliding mode condition. An equivalent formulation shows that  $\ddot{\theta}_1 = -\omega_0^2 u_2 > 0$  for spring 2 in case of  $s < 0$ . Overall,  $s \dot{s} < 0$  is valid. Therefore, a sliding mode motion occurs in 4S with the velocity zero-crossing switching law.

It is not difficult to see that the transient chattering phase is the initial energy redistribution phase, since the switching system without damping can be ideally taken as a conservative system. With the aim of more intuitively describing the energy transformation process between two springs, their deformations are depicted in Fig. 5.5. After the first half motion cycle, Phase B, the angular velocity of the primary plate,  $\dot{\theta}_1$  decreases from the maximum to the minimum and the deformation of spring 2 reaches a maximum, denoted by  $u_{2\text{max}}$ . Afterwards,  $u_2$  will decrease, as denoted by  $(u_{2\text{max}} - u_{2n})$ , and  $u_1$  will increase step by step, as denoted by  $u_{1n}$ , namely in Phase C, until two deformations are equal and reach  $u_{1s}$  and  $u_{2s}$ , respectively, in Phase D. How to avoid a long time transient chattering phase, as marked by a red dotted frame, is of importance to reduce the settling time of the system response.

### 5.3.2. New Switching Surface

In order to reduce the settling time of the system response, a better switching surface should be able to speed up the initial kinetic energy transformation. So a new switching

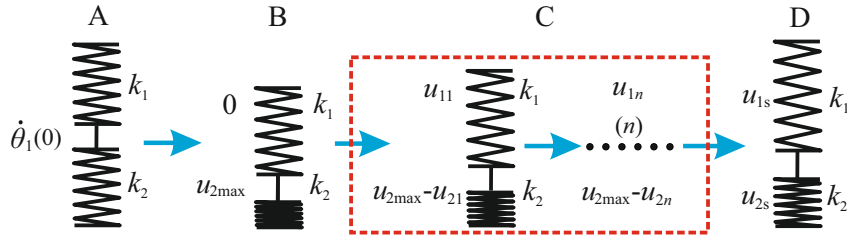


Figure 5.5.: Representation for the potential energy transformation between two springs.

surface is put forward

$$s = \dot{\theta}_1 + \omega_0 \theta_1 = 0. \quad (5.11)$$

As shown in Fig. 5.6, state trajectory (black line) starts from Initial Condition A and

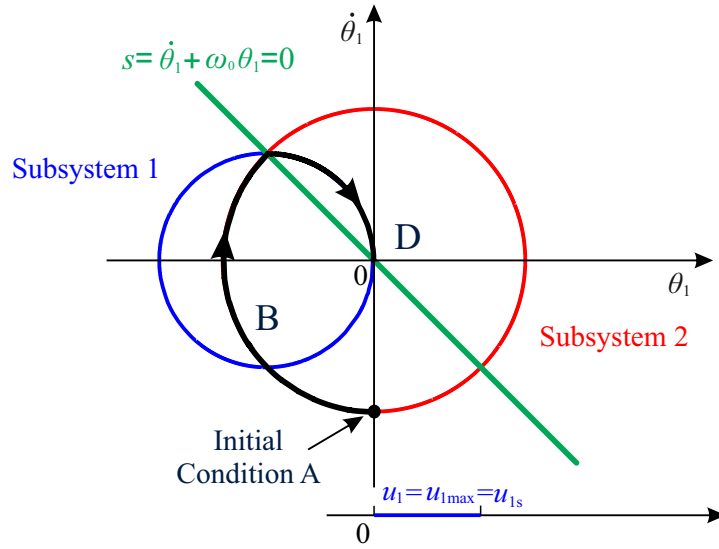


Figure 5.6.: Representation for new switching surface.

then moves into Subsystem 2 trajectory (red line). When the state trajectory reaches the switching surface  $s = \dot{\theta}_1 + \omega_0 \theta_1 = 0$  (green line) for the first time, the potential energy  $U$  and the kinetic energy  $T$  are the same as expressed by

$$\dot{\theta}_1 + \omega_0 \theta_1 = 0 \quad \Rightarrow \quad T = \frac{1}{2} J_1 \dot{\theta}_1^2 = \frac{1}{2} k_\theta \theta_1^2 = \frac{1}{2} k_\theta u_1^2 = U, \quad (5.12)$$

where  $u_1 = \theta_1 - \theta_2$ . Due to  $\theta_2(0) = 0$ , the deformation of spring 1,  $u_1$  is equal to the angular displacement of the primary plate,  $\theta_1$  at this switching time instant. Accordingly, the above conclusion Eq. (5.12) holds. If at this time instant 4S switches into Subsystem 1 trajectory (blue line), the remaining kinetic energy will be transformed into potential energy and stored in Subsystem 1. This means that the new switching law allows 4S to finish an equal transformation of the initial kinetic energy between two springs after the first crossing of the switching surface  $s$  in Eq. (5.11), namely,  $u_1 = u_{1\max} = u_{1s}$ ,  $u_2 = u_{2s}$ . Consequently, the system can go directly into steady chattering state unlike the old switching law and the transient chattering state, Phase

C as shown in Fig. 5.3, is avoided.

Whether or not a sliding mode motion occurs for the new switching surface  $s = \dot{\theta}_1 + \omega_0\theta_1 = 0$  will be further analyzed. Base on the necessary condition for the sliding mode control,  $s\dot{s} < 0$ , the following inequalities must be satisfied

$$\text{If } s > 0 \wedge \dot{s} < 0 \Rightarrow \ddot{\theta}_1 + \omega_0\dot{\theta}_1 < 0 \quad (5.13)$$

and

$$\text{If } s < 0 \wedge \dot{s} > 0 \Rightarrow \ddot{\theta}_1 + \omega_0\dot{\theta}_1 > 0. \quad (5.14)$$

With the combination of Eq. (5.7)-Eq. (5.10), it is not difficult to find that Inequalities (5.13) and (5.14) do not always hold for the new switching surface  $s = \dot{\theta}_1 + \omega_0\theta_1 = 0$ . For example, just after the state trajectory crosses the switching surface for the first time and moves into Subsystem 1 as shown in Fig. 5.6, it tends to move away from but not towards the switching surface, although it still eventually reaches the surface. Thus, the new switching law does not always enable sliding mode motion in 4S. Finally, the new switching law can be given by

$$\mathbf{S}(t) = \begin{cases} [1, 0] & \text{if } s \geq 0 \\ [0, 1] & \text{if } s < 0 \end{cases}, \quad (5.15)$$

where  $s = \dot{\theta}_1 + \omega_0\theta_1$ . Similar to a lumped control system for a translational case as depicted in Fig. 2.9, the block diagram for 4S with the new switching surface  $s$  for a rotational case is shown in Fig. 5.7. where  $s_z$  is discretized like  $\dot{x}_{1z}$  in the translational

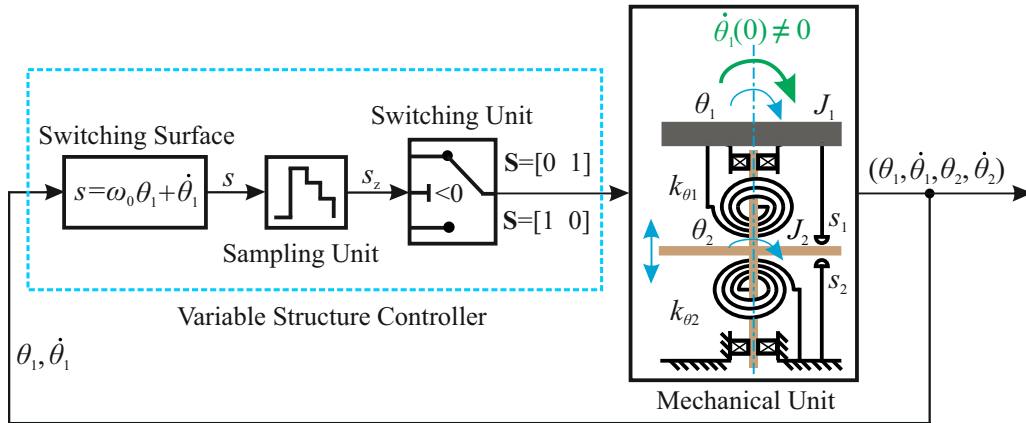


Figure 5.7.: Schematic for 4S with new switching law.

model and can be given by

$$s_z(s, T_s) = \sum_{n=0}^{\infty} s(nT_s) [\sigma(t - nT_s) - \sigma(t - (n+1)T_s)], \quad n \in \mathbb{N}, \quad (5.16)$$

or by

$$s(t, T_s) = s(nT_s), \quad n \in \mathbb{N}, \quad nT_s \leq t < (n+1)T_s, \quad (5.17)$$

so the switching law in Eq. (5.15) will be slightly modified to

$$\mathbf{S}(t) = \begin{cases} [1, 0] & \text{if } s_z \geq 0 \\ [0, 1] & \text{if } s_z < 0 \end{cases} . \quad (5.18)$$

Differing from the velocity zero-crossing switching law, the two state variables  $\theta_1$  and  $\dot{\theta}_1$  should be measured as feedback signals. They are further processed through Variable Structure Controller to produce stiffness switching signals to govern the connection or disconnection of two spiral springs to or away from the primary plate in Mechanical Unit. In order to validate the efficiency of the new switching law, numerical analysis is executed again and the simulation parameters are listed in Table 5.1. Fig. 5.8 shows that the new switching law largely reduces the settling time of the system response compared to the old law as depicted in Fig. 5.1, from  $t = 120$  s to  $t = 6$  s, as marked by a pink dotted line. Fig. 5.9 shows the system state trajectory for the new switching

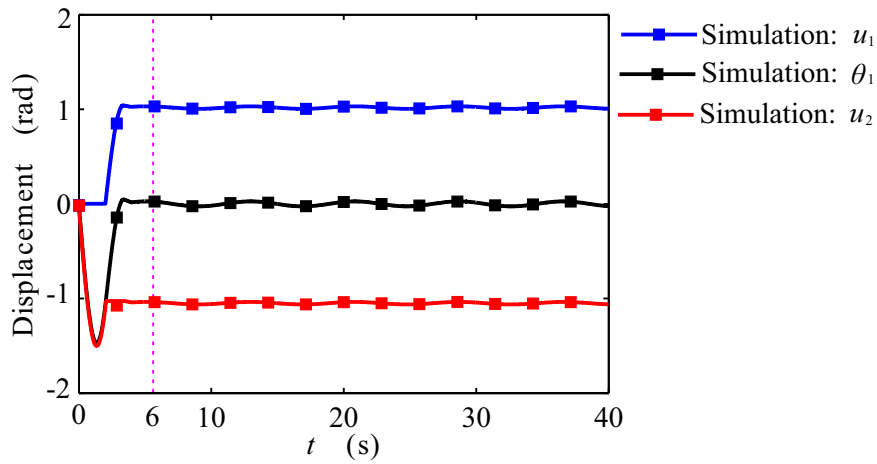


Figure 5.8.: Simulation for 4S with new switching law under nonzero initial velocity  $\dot{\theta}_1(0) = -1.75$  rad/s, here  $\eta_s = 100$ .

law. Differing from the old switching law, the new switching law allows 4S to avoid the transient chattering state, Phase C and to go directly into steady chattering state, Phase D as shown in Fig. 5.2.

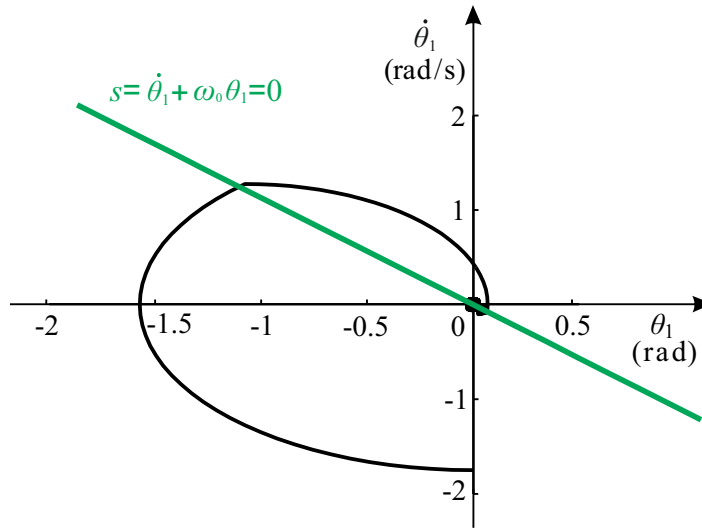


Figure 5.9.: Phase plane for 4S with new switching law under nonzero initial velocity  $\dot{\theta}_1(0) = -1.75$  rad/s, here  $\eta_s = 100$ .

## 5.4. Experimental Verification

### 5.4.1. Nonzero Initial Velocity Condition

In order to further verify the new switching law, an experiment under nonzero initial velocity conditions is carried out.

As mentioned in the theory analysis, the initial angular velocity of the primary plate  $\dot{\theta}_1(0)$  is equal to  $-1.75$  rad/s and the initial deformation of spring 2,  $u_2(0)$ ,  $u_2(0) = \theta_2(0) = 0$ . In practice, it is difficult to realize a zero initial position, here  $\theta_1(0) = 0$  and  $\theta_2(0) = -0.08$  rad. Because before a nonzero initial velocity disturbance is exerted on 4S, the system has begun to switch. At the beginning  $\dot{\theta}_1 = 0$ , the switching law Eq. (5.18) leads to an attraction between electromagnet-plate 2 and the base as shown in Fig. 4.1(b). This will result in a slight shaking of the primary plate and therefore an extremely low amplitude chattering occurs in the system. Compared to a high initial kinetic energy,  $T = 1/2 J_1 \dot{\theta}_1^2(0) = 0.1853$  J, the initial potential energy  $U$ , as expressed by

$$U = \frac{1}{2} k_\theta u_1^2(0), \quad u_1(0) = \theta_1(0) - \theta_2(0), \quad (5.19)$$

is equal to  $4.8 \times 10^{-4}$  J according to Table 5.1 and can be neglected and therefore Eq. (5.12) still holds. As shown in the system parameter identification experiment in Subsection 4.4.1, there exists system damping  $M_f$  including viscous damping,  $D_1 = 0.023$  and  $D_1 = 0.02$ , and Coulomb damping  $M_{fc1} = 0.0087$  Nm and  $M_{fc2} = 0.0092$  Nm in setup, but these factors are not considered in the above theory analysis. Therefore, the simulation results under an ideal nonzero initial velocity condition are shown here in order to comparably explain the damping effect on the system response. The results are shown in Fig. 5.10, where solid lines stand for the experimental results and square-solid lines for the simulation. Fig. 5.10(a) shows the simulation under an ideal nonzero initial velocity condition, which is a partly zoomed-in picture of Fig. 5.8, from  $t = 0$  to

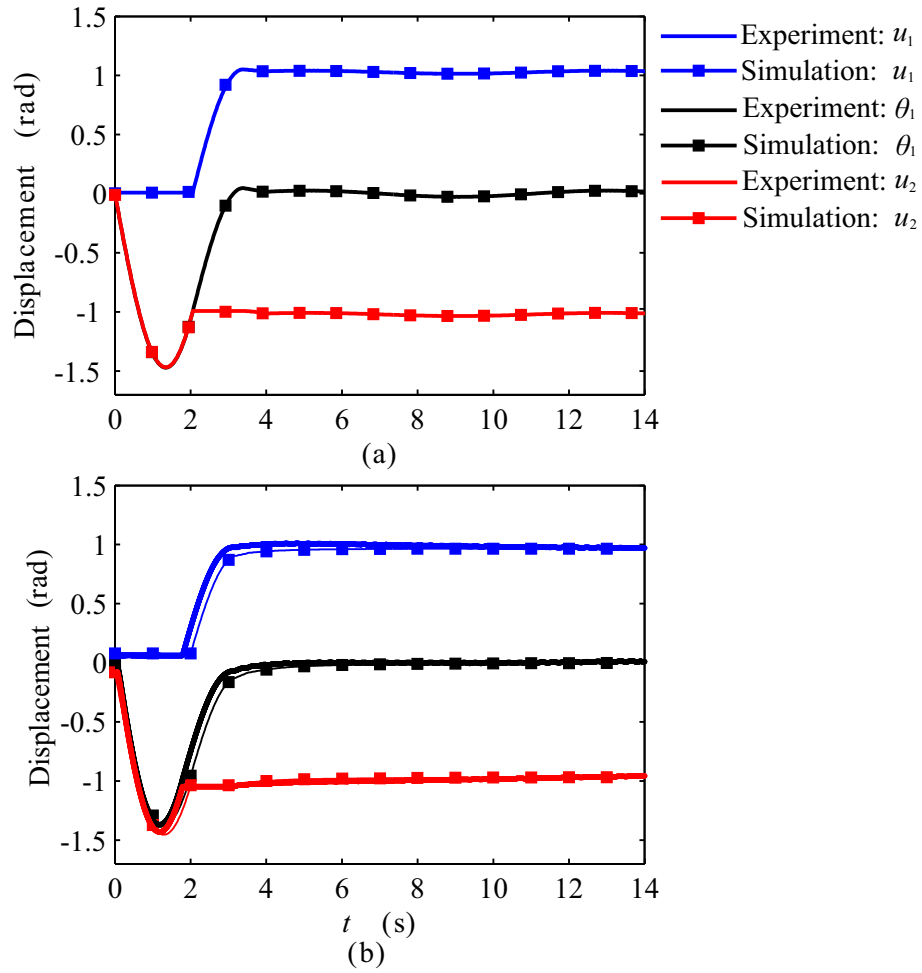


Figure 5.10.: System response under nonzero initial velocity for new switching law. (a) Simulation under ideal nonzero initial velocity condition  $\dot{\theta}_1(0) = -1.75$  rad/s:  $M_f = 0$ ,  $\theta_1(0) = 0$  and  $\theta_2(0) = 0$ ; (b) Experimental and simulation results for system response under nonideal initial velocity condition  $\dot{\theta}_1(0) = -1.75$  rad/s:  $M_f \neq 0$ ,  $\theta_1(0) = 0$  and  $\theta_2(0) = -0.08$  rad.

$t = 14$  s. Fig. 5.10(b) depicts the simulation and experiment results under a nonideal nonzero initial velocity condition. The initial velocity disturbance,  $\dot{\theta}_1 \neq 0$ , is achieved here by suddenly pushing the primary plate. Through a preliminary calculation of the slope of an approximately linear ( $u_2-t$ ) curve in the beginning and further adjustment in simulation model, the initial velocity can be obtained,  $\dot{\theta}_1(0) = -1.75$  rad/s. These initial conditions will be eventually adjusted in the simulation model to match the experiment. This has been also explained in the last chapter.

It is clear to see that 4S with the new switching law can finish the initial kinetic energy transformation equally between two springs in only one switching time phase and then moves into steady state. Compared to the no damping condition in Fig. 5.10(a), the stored potential energy in the two springs decreases slightly in experiment due to a low viscous damping and Coulomb damping. Meanwhile, the system is able to remain around a better equilibrium-like position without fine oscillations. A nonzero initial position, here  $\theta_2(0) = -0.08$  rad produces a small difference between the angular displacement of the primary plate  $\theta_1$  and the deformation of spring 2,  $u_2$  at beginning. Compared to the system response under the old switching law, the settling time is largely reduced as shown in Fig. 5.1(b). However, this new switching law has the disadvantage of requiring two state variables feedback information. Additionally, the experiment agrees with the simulation well as shown in Fig. 5.10(b). In order to show

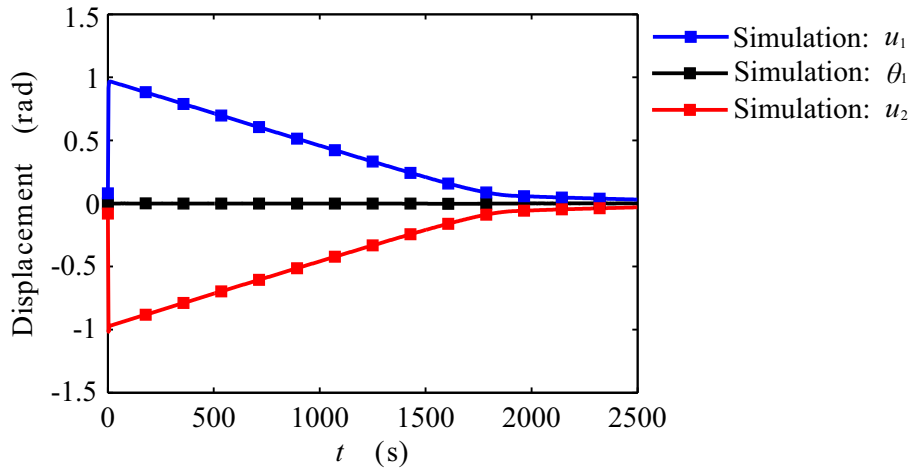


Figure 5.11.: Long time system response under nonideal nonzero initial velocity condition for new switching law at  $\dot{\theta}_1(0) = -1.75$  rad/s:  $M_f \neq 0$ ,  $\theta_1(0) = 0$  and  $\theta_2(0) = -0.08$  rad.

the long time system response for the new switching law and avoid the risk of the setup failure under a long time operation, the simulation is instead executed here and the results are shown in Fig. 5.11. Due to the system damping including viscous damping and Coulomb damping, the potential energy stored in two springs, denoted by  $u_1$  and  $u_2$ , always decreases to zero, but the primary plate always stays around a zero equilibrium-like position, namely,  $\theta_1 \approx 0$ .



### 5.4.2. Harmonic Excitation

The new switching law outperforms the old switching law under a nonzero initial velocity condition as shown in Fig. 5.10. Whether or not this new switching law works well under a harmonic excitation will be tested here, the results are shown in Fig. 5.12, where subfigure(a) is the zoomed-in picture for subfigure(b), marked by an orange frame. Note, that due to a local magnification, the experimental results are not denoted by lines any more but discrete points as shown in subfigure(a). Here the static deflection is defined as  $\hat{M}_d/k_\theta = 0.05/0.15 = 0.39$  rad. Compared to the system response using the velocity zero-crossing switching law as shown in Fig. 4.20, the system with a new switching law benefits from the position feedback control and keeps at a better zero equilibrium-like position, denoted by black lines  $\theta_1$  in subfigure (b). This reduces the effect of the time delay produced by the used electromagnetic switch on the positioning performance. In the beginning, the simulation and experiment results match well as depicted in subfigure(a). Due to the system stiffness and damping variation in experiment, the difference between the simulation and experiment increases slightly with time as shown in subfigure(b). This can be reasonably accepted.

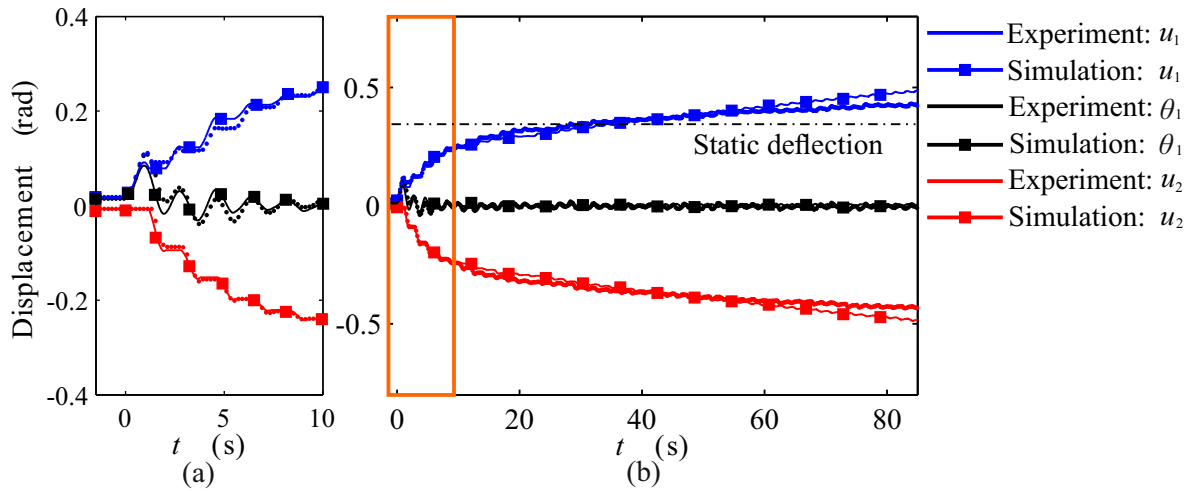


Figure 5.12.: System response for new switching law under a harmonic excitation:  $\hat{M}_d = 0.05$  Nm,  $\eta_d = 3$  and  $\eta_s = 100$ .

### 5.4.3. PID Feedback Controlled Switching Law

In fact, the velocity zero-crossing switching law in Section 2.4 for 4S works as the derivative control (D control) for the displacement of mass  $x_1$  with  $x_{1\text{ref}} = 0$  as shown in Fig. 5.13(a), and new switching law works as the combination of the proportional control (P control) and the derivative control (D control) in Fig. 5.13(b). So a complete PID feedback controlled switching law is further introduced here as depicted in Fig. 5.13(c). Note that  $x_1$  and  $x_{1\text{ref}}$  in a translation case correspond to  $\theta_1$  and  $\theta_{1\text{ref}}$  in a rotation case. As a new switching decision, PID feedback control of the error between

the reference position and the state variable,  $x_{1\text{ref}} - x_1$ , is introduced

$$f(x_1) = K_p(x_{1\text{ref}} - x_1) + K_i \int_0^t (x_{1\text{ref}} - x_1(\tau)) d\tau + K_d \frac{d(x_{1\text{ref}} - x_1)}{dt}. \quad (5.20)$$

Similar to the discretized state variable  $\dot{x}_1$  in Eq. (4.28) and the new switching surface  $s$  in Eq. (5.16),  $f(x_1)$  is also processed discretely and rewritten as

$$f(x_1)_z = \sum_{n=0}^{\infty} f(x_1(nT_s)) [\sigma(t - nT_s) - \sigma(t - (n+1)T_s)], \quad n \in \mathbb{N}, \quad (5.21)$$

or as

$$f(x_1(t, T_s))_z = f(x_1(nT_s)), \quad n \in \mathbb{N}, \quad nT_s \leq t < (n+1)T_s. \quad (5.22)$$

As a result, the switching law for the PID controlled system is given by

$$\mathbf{S}(t) = \begin{cases} [0, 1] & \text{if } f(x_1)_z < 0 \\ [1, 0] & \text{if } f(x_1)_z \geq 0 \end{cases}. \quad (5.23)$$

Considering both the vibration energy harvesting level and positioning demand, a set of the proportional (P), integral (I) and derivative (D) parts of PID control must be chosen carefully in practice. Unlike the PID control used in a linear system, an increase in PID coefficients of the same proportion will not influence the system response, because a zero-crossing decision is applied on the switching system. This will be detailed investigated in future.

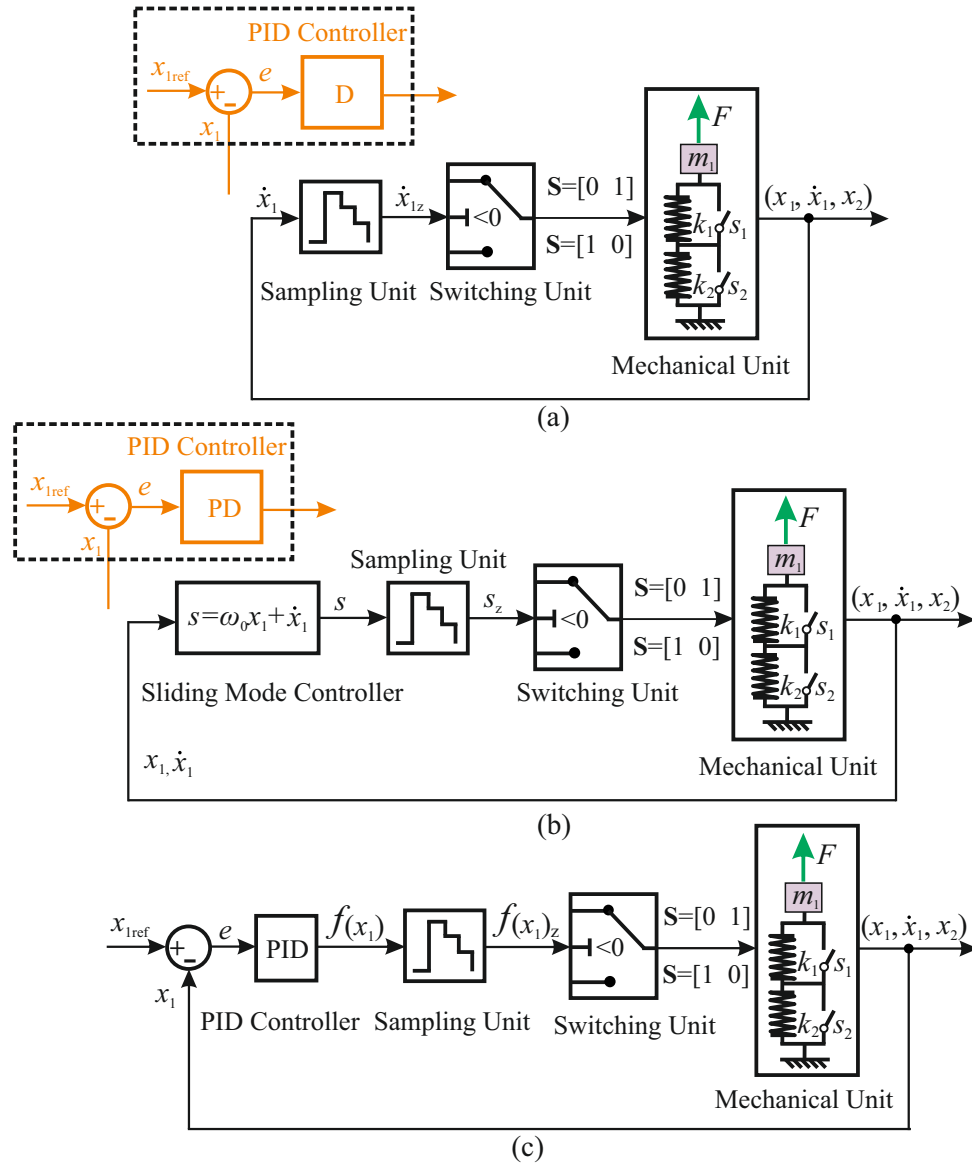


Figure 5.13.: Block diagram for different switching laws. (a) Velocity zero-crossing switching law; (b) Position and velocity switching law; (c) PID feedback controlled switching law.



---

# Shock Isolation with 4S

---

## 6.1. Introduction

Shock isolation has been always of interest in technical applications where the negative effects of a sudden shock excitation on the protected plants, devices or persons need to be avoided. As analyzed in Section 2.2 in a passive or a variable stiffness system there still exists an unavoidable potential energy releasing time phase. Consequently, a protected payload is accelerated and the settling time of system will be extended. As for shock isolation, this will extend the residual vibration duration after shock. This chapter will explore the application of 4S on shock isolation and compare its behavior to two other shock isolation systems. New insights into the shock isolation behavior of a PID controlled 4S are concluded.

## 6.2. Harmonic disturbance isolation using 4S

In order to investigate the vibration isolation performance of 4S, the velocity zero-crossing switching law, according to Eq. (2.38), would be initially tested on 4S under a harmonic base disturbance in this section.

### 6.2.1. Modeling

For vibration isolation, a base excitation is exerted on 4S as shown in Fig. 6.1. Similar to the force excitation case as mentioned in Section 2.3, 4S has two stiffness working states according to the switching law in Eq. (2.36). A compact formulation for the

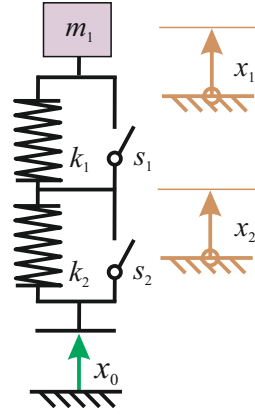


Figure 6.1.: Schematic of 4S under base excitation  $x_0$ .

system dynamics can be expressed by

$$m_1 \ddot{x}_1 + kx_1 = F_p(x_1, x_2, \dot{x}_1, T_s) + kx_0, \quad (6.1)$$

and the displacement of the connection point between two serial elements

$$x_2 = \begin{cases} x_2(t_{sw,i}) - x_0(t_{sw,i}) + x_0 & \text{if } \dot{x}_{1z}(\dot{x}_1, T_s) \geq 0 \\ x_2(t_{sw,i}) - x_1(t_{sw,i}) + x_1 & \text{if } \dot{x}_{1z}(\dot{x}_1, T_s) < 0 \end{cases}, \quad (6.2)$$

and the process force  $F_p$  acting on the mass according to Fig. 2.8(a),

$$F_p(x_1, x_2, \dot{x}_1, T_s) = \begin{cases} k u_2(t_{sw,i}) & \text{if } \dot{x}_{1z}(\dot{x}_1, T_s) \geq 0 \\ k u_1(t_{sw,i}) & \text{if } \dot{x}_{1z}(\dot{x}_1, T_s) < 0 \end{cases}, \quad (6.3)$$

with spring deformations  $u_1$  and  $u_2$  defined by

$$u_1 := x_1 - x_2, \quad u_2 := x_2 - x_0. \quad (6.4)$$

A harmonic base excitation is applied as follows

$$x_0(t) = \hat{x}_0 \sin \Omega t, \quad (6.5)$$

where  $\Omega$  is the excitation frequency and  $\hat{x}_0$  is the excitation amplitude. The related dimensionless parameters  $\eta_d$  and  $\eta_s$  are defined in the force excitation case according to Eq. (2.22) and Eq. (2.51).

## 6.2.2. Numerical Analysis

In order to test vibration isolation performance of 4S, numerical analysis is initially executed in this section. Table 6.1 lists the simulation parameters and Fig. 6.2 shows the results. As shown in Fig. 6.2(a), 4S together with the velocity zero-crossing switching law can realize vibration isolation. At beginning,  $t \in [0, T_0/2]$  s,  $T_0/2 \approx 3.15$  s,  $m_1$  moves in a positive direction and  $\mathbf{S}(0) = [1, 0]$ , where only spring 1 is active, spring 2 is blocked. This can be seen by the deep blue line,  $\dot{x}_1 > 0$ , and the orange line,  $x_1 > 0$ ,

**Table 6.1.**

Simulation parameters for harmonic excitation.

Name	Value	Unit	Name	Value	Unit	Name	Value	Unit
$\hat{x}_0$	1	m	$\eta_d$	10	-	$x_1(0)$	0	m
$m_1$	1	kg	$\eta_s$	1000	-	$\dot{x}_1(0)$	0	m/s
$k$	1	N/m				$x_2(0)$	0	m

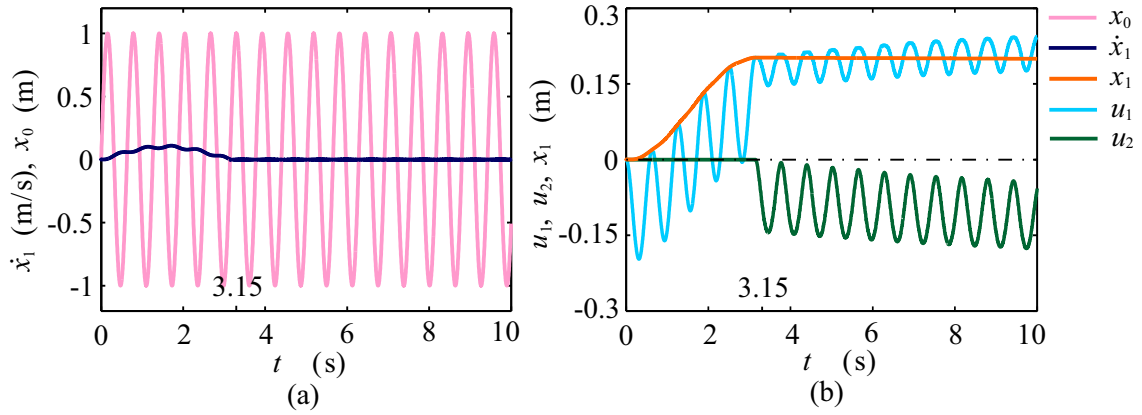


Figure 6.2.: Harmonic disturbance isolation response. (a) Velocity of mass and base excitation; (b) Displacement of mass and deformations of two springs.

respectively. Differing from a desired elongation of spring 1, it is compressed,  $u_1 < 0$ , because the base velocity is higher than that of the mass. Spring 1 oscillates with the subsystems natural period  $T_0$  into an elongation state  $u_1 > 0$ , but spring 2 remains undeformed,  $u_2 = 0$ .

After the first time of the velocity zero-crossing detection,  $t = T_0/2 \approx 3.15$  s, the two springs switches into 4S alternatively, where spring 1 is elongated and spring 2 compressed. Before the occurrence of the stiffness switching, spring 1 has been elongated. Consequently, spring 2 owns a larger oscillating deformation amplitude than spring 1 in the following switching process. This leads to a nonzero pseudo equilibrium position of the mass, depicted by the orange line. Note that it is not a strict equilibrium but a chattering with a low amplitude around an equilibrium position. Additionally, the spring deformations increase and potential energy will be stored in two springs for a long time, which was partly formulated in [124].

## 6.3. Shock isolation for 4S

Section 6.2 shows the vibration isolation capabilities of 4S together with the velocity zero-crossing switching law at a harmonic base disturbance. How to apply effectively 4S for shock isolation will be discussed in the following sections.

### 6.3.1. Shock isolation systems

A shock disturbance via the base can be given by [127]

$$x_0(t) = \begin{cases} \frac{\hat{x}_0}{2} \left( 1 - \cos \frac{2\pi t}{\tau} \right), & 0 \leq t \leq \tau \\ 0, & t > \tau \end{cases}, \quad \Omega = 2\pi/\tau, \quad (6.6)$$

where the shock input has a duration of  $\tau$ , an amplitude of  $\hat{x}_0$  and the circular frequency  $\Omega$ . Its time behavior is shown in Figure 6.3. Combined with Eq. (2.22), the relationship between  $\tau$  and  $T_0$  can be given by

$$\frac{\tau}{T_0} = \frac{\omega_0}{\Omega} = \frac{1}{\eta_d}. \quad (6.7)$$

A Shock Isolation System (SIS) needs a fast response to protect the payload and guar-

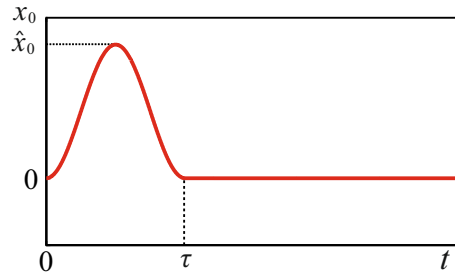


Figure 6.3.: Schematic for shock excitation

antee an accurate repositioning simultaneously. The velocity zero-crossing switching law in Section 6.2, can be interpreted as a derivative feedback control with  $x_{1\text{ref}} = 0$  as mentioned in Section 5.4.3. Such a feedback control law lacks a repositioning of the payload  $m_1$ , as shown in Fig. 6.2(b). This is the reason why a PID feedback control is introduced here. Since 4S is able to harvest vibration energy and then behaves as an actuator, small quantities of potential energy pre-storage,  $u_1(0) \neq 0$ ,  $u_2(0) \neq 0$ , is provided in 4S before shock to react against shock. Its behavior can be classified as a semi-active, energy harvesting shock isolation system and adjusted to the shock excitation Eq. (6.6). With the combination of Eq. (6.4) and Eq. (6.6), the dimensionless potential energy pre-storage parameter  $\gamma$  is introduced here

$$\gamma := u_2(0)/\hat{x}_0 = -u_1(0)/\hat{x}_0 = x_2(0)/\hat{x}_0, \quad (6.8)$$

which denotes the relationship between the potential energy pre-storage and the peak value of the shock  $\hat{x}_0$ .

In order to evaluate the shock isolation performance of 4S, another two shock isolation systems are taken into consideration. In fact, these systems have been already mentioned as shown in Fig. 2.1(a) and Fig. 2.2 in Section 2.2.1. Here a shock disturbance will be exerted on the base of these systems like that in Fig. 6.2. The first one is a passive system with stiffness  $k$  and damping  $d$ , Passive Damped System (PDS). The second one is another semi-active vibration control system: Parallel Stiffness Switch



System (PSSS) with two stiffness  $\Delta k$  and  $k - \Delta k$  in parallel with each other, one damping  $\Delta d$  and one switch  $s$ . For PDS, the dimensionless damping ratio  $D = d/(2\sqrt{km_1})$ , is introduced again. For PSSS, two switching laws are applied in [19]. One is open loop control, where the low stiffness  $k - \Delta k$  is used during shock and the high stiffness  $k - \Delta k + \Delta k = k$  after shock. The open loop control stands for a vibration energy non-dissipation system, where the stored potential energy would be distributed between two springs after shock. The other is closed loop control as expressed by Eq. (2.4). For system variable  $\kappa$ ,  $\kappa = \frac{\Delta k}{k}$ , the stiffness relationship in PSSS can be decided. The closed-loop controlled PSSS is a vibration energy dissipation system. When switch  $s$  is open, the spring  $\Delta k$  will be connected to the damper  $\Delta d$  and the stored potential energy in the spring will be converted into heat by means of the damper as depicted in Fig. 2.2. As for the closed loop controlled PSSS-SIS, the stiffness switching law according to Eq. (2.4) allows a low frequency stiffness switching with a switching period of one fourth of each subsystems natural period compared to 4S-SIS. As for 4S-SIS, both vibration energy harvesting level and repositioning demand need a reasonable set for the proportional, integral and derivative coefficients in practice,  $K_p$ ,  $K_i$ ,  $K_d$ . According to the energy harvesting switching law Eq. (2.36), the derivative part  $K_d$  could be decided firstly and is set 1 here. After a small quantity of potential energy has been stored, 4S works as an actuator. How to track the demand position will further decide the proportional part  $K_p$  and the integral part  $K_i$  depending on the practice experience. All of constant system parameters are listed in Table 6.2. The used simulation parameters for PSSS are cited from [19]. Repositioning of mass  $m_1$

**Table 6.2.**

Simulation parameters for shock isolation with different systems.

Name	Value	Unit	Name	Value	Unit	Name	Value	Unit
$\hat{x}_0$	1	m	$K_p$	1	-	$x_{1\text{ref}}$	0	m
$\tau$	1	s	$K_i$	0.05	-	$x_1(0)$	0	m
$m_1$	1	kg	$K_d$	1	-	$\dot{x}_1(0)$	0	m/s
$\kappa$	0.5	-	$\eta_s$	1000	-			
$\Delta d$	1	Ns/m						

after shock requires the reference position  $x_{1\text{ref}} = 0$ , which enables the payload  $m_1$  keep at a zero initial position. The systems have the following design parameters, PDS-SIS:  $(\eta_d, D)$ ; PSSS-SIS:  $(\eta_d)$ ; 4S-SIS:  $(\eta_d, \gamma)$ . These parameters will be varied for system behavior analysis. Note that the variation of  $\eta_d$  at a constant shock duration  $\tau$  results in the variation of the circular natural frequency  $\omega_0$  and the corresponding stiffness  $k$  in all systems. The damping ratio  $D$  takes the values of 0 and 1, describing a passive undamped and damped system, respectively.

### 6.3.2. Shock isolation using 4S without potential energy pre-storage

In this section the shock isolation, residual vibration suppression and repositioning performances of 4S-SIS without potential energy pre-storage are investigated and compared to PDS-SIS and PSSS-SIS. The design parameters of the three systems,  $\eta_d$ ,  $\gamma$  and

$D$  are listed in Table 6.3. Without potential energy pre-storage in 4S-SIS, i.e.  $\gamma = 0$ ,

**Table 6.3.**  
Design parameters for  
different SISs.

Name	Value	Unit
$\eta_d$	4, 1, 0.5	-
$\gamma$	0	-
$D$	0, 1	-

the initial spring deformation is zero,  $u_1 = u_2 = 0$ , according to Eq. (6.8). Thus, the initial conditions are  $x_1(0) = x_2(0) = 0$ . For PDS-SIS and PSSS-SIS, the initial conditions are the same,  $x_1(0) = 0$ . In these cases, 4S-SIS has a high dimensionless sampling frequency  $\eta_s \gg \eta_d$ , e.g.  $\eta_s = 1000$  as listed in Table 6.2. The simulation results are shown in Fig. 6.4. The subfigure pairs 6.4[(a), (b)], 6.4[(c), (d)] and 6.4[(e), (f)] describe the payload displacement  $x_1$  of the three SISs and the spring deformations  $u_1$ ,  $u_2$  of 4S-SIS at supercritical excitation  $\eta_d = 4$ , resonant excitation  $\eta_d = 1$  and subcritical excitation  $\eta_d = 0.5$ , respectively. All of horizontal axes stand for the time  $t$  and the left-hand side vertical axes denote the payload displacement  $x_1$ , which is scaled to the peak value of shock  $\hat{x}_0$ . The right-hand side vertical axes represent the spring deformations of 4S-SIS. If  $x_1/\hat{x}_0 < 1$ , shock isolation happens; or else,  $x_1/\hat{x}_0 > 1$  means shock amplification, which should be avoided in a SIS. The payload displacement response plots 6.4(a), (c), (e) are divided in two time phases, the shock phase (SP)  $t \in [0, 1]$  s and the residual vibration phase (RVP)  $t \in [1, 5]$  s.

As shown in Fig. 6.4(a), shock isolation happens in the three SISs only under a supercritical shock excitation. At a resonant and subcritical excitation in Fig. 6.4(c), (d), there exist shock amplification phenomena. In all cases, Fig. 6.4(a), (c) and (e), PDS-SIS with a critical damping,  $D = 1$ , shows the best performance. 4S-SIS owns a comparable behavior to the closed-loop controlled PSSS-SIS in SP in all cases. However, 4S-SIS shows a faster vibration reduction in the residual vibration phase than the closed-loop controlled PSSS-SIS. The open-loop controlled PSSS-SIS has a better shock isolation performance at a supercritical excitation due to a lower stiffness, but lacks a residual vibration reduction and repositioning ability since it only switches to a higher stiffness after shock. Consequently, no vibration energy dissipation occurs in the open-loop controlled PSSS-SIS and the stored potential energy is only divided in two springs after shock. This is obviously shown in Fig. 6.4(e). From Fig. 6.4(b), (d) and (f), it is found that at beginning the spring  $k_2$ , is locked,  $u_2 = 0$  until the payload  $m_1$  reaches a velocity reversal for the first time. In the time phase the spring,  $k_1$ , is firstly compressed before reaching its elongation state, because the velocity of base is larger than that of the payload. At the final stage of the residual vibration phase both springs have almost the same amount of deformations, but one is compressed and the other elongated according to the aforementioned switching law.

It is concluded that 4S-SIS outperforms PSSS-SIS in the residual vibration reduction but does not show an obvious advantage for shock isolation against the other SISs. To improve the full performance of 4S-SIS a potential energy pre-storage is introduced into 4S-SIS to react against shock just from the beginning when shock input comes.

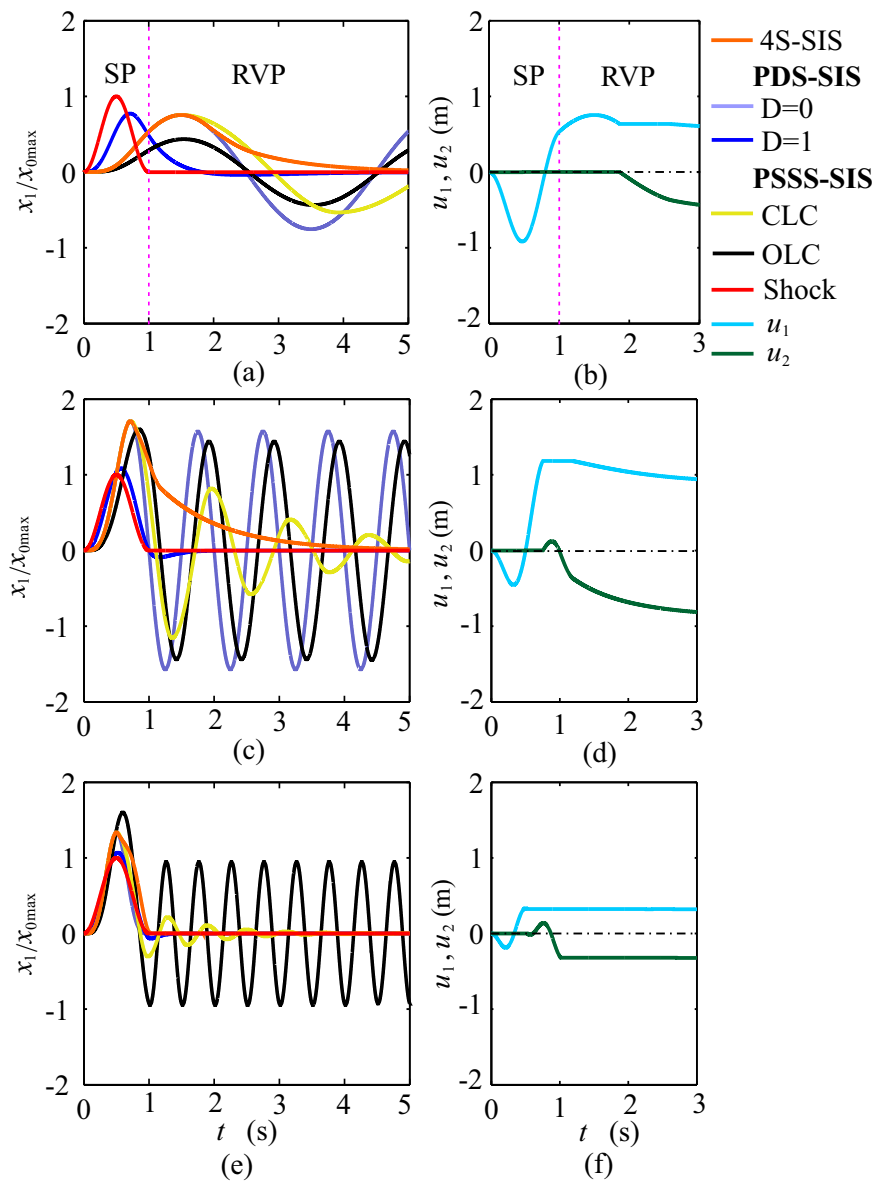


Figure 6.4.: Shock response of different shock isolation systems and deformations of two springs of 4S. SP: Shock Phase; RVP: Residual Vibration Phase; CLC: Closed Loop Control; OLC: Open Loop Control. (a), (c) and (e) stand for the displacement response of different shock isolation systems and (b), (d) and (f) for the deformations of two springs ((a),(b):  $\eta_d = 4$ ; (c),(d):  $\eta_d = 1$ ; (e),(f):  $\eta_d = 0.5$ ).

### 6.3.3. Shock isolation using 4S with potential energy pre-storage

As shown in Fig. 6.2, 4S is able to dominate the system response like an actuator if enough potential energy is stored in two spring. To enable 4S-SIS work as an actuator and react against shock excitation strongly, a specified amount of potential energy pre-storage,  $\gamma \neq 0$ . As an example,  $\gamma = -0.5$  is set here. All other simulation parameters are the same as that in Section 6.3.2. Therefore, the initial conditions  $x_1(0) = 0$ ,  $x_2(0) = -0.5$ ,  $\dot{x}_1(0) = 0$  are given for 4S-SIS and  $x_1(0) = 0$ ,  $\dot{x}_1(0) = 0$  for PDS-SIS and PSSS-SIS. Fig. 6.5 shows the simulation results. From Fig. 6.5(a), (c) and (e), it is obviously found that 4S-SIS outperforms the other SISs in terms of shock isolation, no matter if it suffers from a supercritical, a resonant or a subcritical shock excitation. After shock, the critical PDS-SIS,  $D = 1$ , shows a better residual vibration reduction under the resonant and the subcritical excitation, but 4S-SIS also goes back to the initial zero position progressively, the repositioning performance is improved largely compared to that in Section 6.3.2. As shown in Fig. 6.5(b), (d) and (f), a potential energy pre-storage enables 4S-SIS react against shock more initiatively and makes the final stored potential energy level in different stiffness systems almost equivalent, not like 4S-SIS without potential energy pre-storage in Fig. 6.4(b), (d) and (f).

In order to evaluate whether 4S-SIS with potential energy pre-storage can isolate shock in the low frequency region, namely,  $\omega_0 > \Omega$  or  $T_0 < \tau$  or  $\eta_d < 1$ , shock response spectra analysis [128] for 4S-SIS, PDS-SIS and PSSS-SIS is also done. The results are shown in Fig. 6.6. For the spectra analysis, the maximum displacement response during shock is required,

$$x_{1S,\max} = \max \{|x_1(t)|\} , \quad 0 \leq t \leq \max\{\tau, T_0\} = \tau \cdot \max\{1, \eta_d\} , \quad (6.9)$$

where  $t$  is the time. Then shock isolation criterion:  $\frac{x_{1S,\max}}{\hat{x}_0}$ , is defined by the ratio of  $x_{1S,\max}$  to the maximum input peak value  $\hat{x}_0$  in Eq. (6.6). From Fig. 6.6, a critical PDS-SIS shows a low maximum displacement response near resonance, namely,  $\eta_d = 1$ , but it does not still enable shock isolation at a low frequency region obviously. The potential energy pre-storage in 4S-SIS realizes shock isolation in the whole frequency region. As aforementioned before, this comes at the price of a high dimensionless sampling frequency  $\eta_s$ , here  $\eta_s = 1000$ .

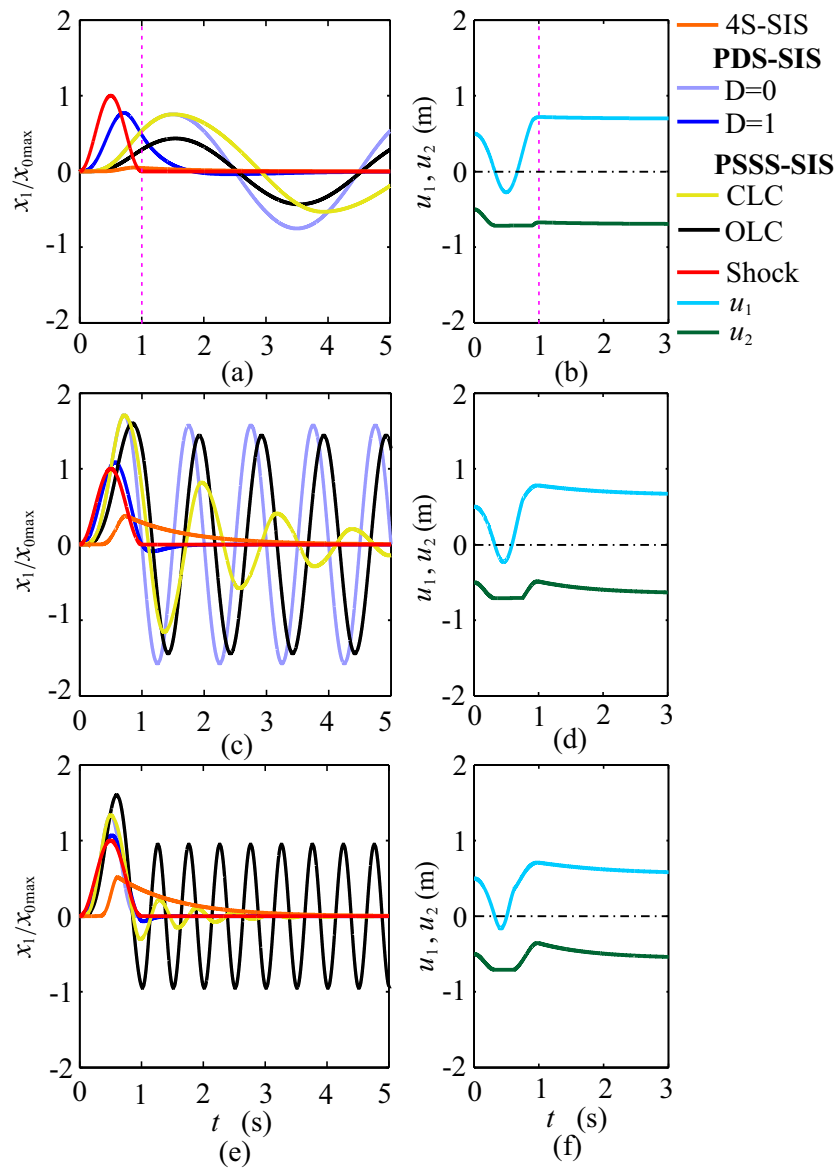


Figure 6.5.: Shock response of different shock isolation systems for different  $\eta_d$  and deformations of two springs of 4S. SP: Shock Phase; RVP: Residual Vibration Phase; CLC: Closed Loop Control; OLC: Open Loop Control. (a), (c) and (e) stand for the displacement response of different shock isolation systems and (b), (d) and (f) for the deformations of the two springs of 4S ((a),(b):  $\eta_d = 4$ ; (c),(d):  $\eta_d = 1$ ; (e),(f):  $\eta_d = 0.5$ ).

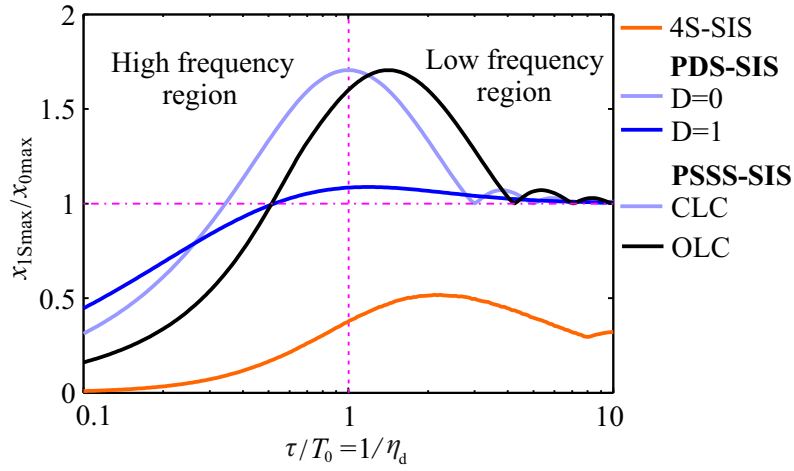


Figure 6.6.: Shock response spectra analysis for different SISs. CLC: Closed Loop Control; OLC: Open Loop Control.

## 6.4. Shock isolation performance analysis of 4S

In the last section, a shock isolation example is analyzed and shows that 4S performs well. However, this superiority relies on the systems parameters, dimensionless disturbance frequency  $\eta_d$ , dimensionless sampling frequency  $\eta_s$  and dimensionless potential energy pre-storage  $\gamma$ . This section will address their effects on the performance of 4S.

### 6.4.1. Time domain analysis

The dimensionless sampling frequency  $\eta_s = T_0/T_s$ , according to Eq. (2.51), plays a role on the stiffness switching decision as mentioned in Section 2.4. Similarly, this also happens in a PID feedback controlled 4S.

In order to concisely formulate the shock isolation performance of 4S under different dimensionless sampling frequencies  $\eta_s$ , the displacement response at a supercritical shock excitation as an example is done in Fig. 6.7, where  $\eta_d = 2\pi$ ,  $\gamma = -0.5$  and the other simulation parameters are listed in Table 6.2. In SP there exists a minimum sampling frequency for the shock isolation criterion  $\frac{x_{1S,max}}{\hat{x}_0}$  at  $\eta_s = 50$ , whereas in the residual vibration phase an increasing sampling frequency improves vibration suppression, because a larger sampling frequency enables a lower stiffness switching decision error as depicted in Fig. 2.7, of course, here vertical axis stands for  $f(x_1, T_{s,i})_z$  according to Eq. (5.21). Because each subsystem,  $m_1-k_1$  or  $m_1-k_2$ , is a conservative system, the oscillation after shock is composed of a forced vibration term due to chattering and a free undamped vibration term.

From Fig. 6.8, it is found that  $\frac{x_{1S,max}}{\hat{x}_0}$  decreases with the increase of the dimensionless potential energy pre-storage  $\gamma$ , since more potential energy enables 4S react against shock more initiatively.

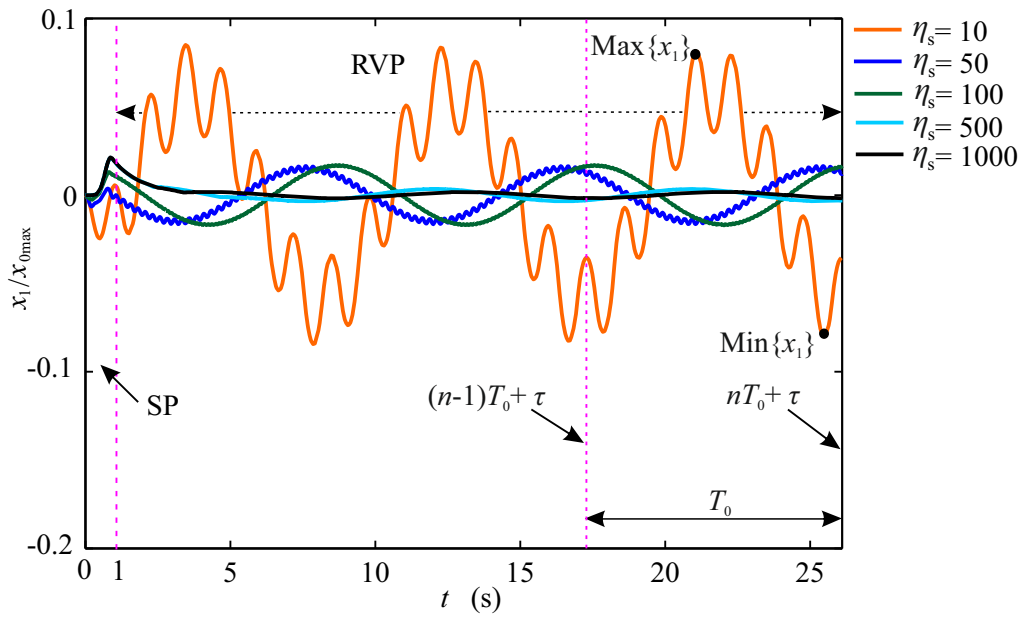


Figure 6.7.: Shock response of 4S for different dimensionless sampling frequencies under  $\gamma = -0.5$  and  $\eta_d = 2\pi$ . SP: Shock Phase; RVP: Residual Vibration Phase.

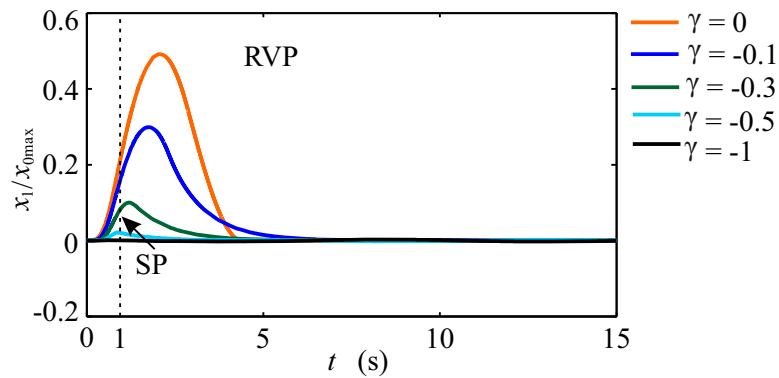


Figure 6.8.: Shock response of 4S for different dimensionless potential energy pre-storage  $\gamma$  under  $\eta_s = 1000$  and  $\eta_d = 2\pi$ . SP: Shock Phase; RVP: Residual Vibration Phase.

### 6.4.2. Multi-dimension parameters performance analysis of 4S

Apart from the observation of the shock isolation performance analysis during shock, in order to characterize the residual vibration suppression performance, the maximum displacement response  $x_{1R,\max}$  after shock is defined as

$$x_{1R,\max} = \frac{1}{2} (\max \{x_1(t)\} - \min \{x_1(t)\}) , \quad (n-1)T_0 + \tau \leq t \leq nT_0 + \tau , \quad n \in \mathbb{N} , \quad (6.10)$$

where  $t$  is the simulation time,  $0 \leq t \leq nT_0 + \tau$ ,  $n$  is a fixed number. As an example, the parameters in Eq. (6.10) are marked in Fig. 6.7 for  $n = 3$ . Similar to the shock isolation criterion  $\frac{x_{1S,\max}}{\hat{x}_0}$ , the residual vibration suppression criterion  $\frac{x_{1R,\max}}{\hat{x}_0}$ , is defined here. Following are the effects of the system parameters  $\eta_d, \eta_s, \gamma$  on the criteria  $\frac{x_{1S,\max}}{\hat{x}_0}$  and  $\frac{x_{1R,\max}}{\hat{x}_0}$  examined and shown in Fig. 6.9 - Fig. 6.11, where all of subfigures (a) show the shock isolation performance during shock and (b) show the residual vibration suppression performance after shock. Depending on the simulation experience,  $n = 10$  is chosen for the analysis to ensure a steady state system response for the residual vibration phase.

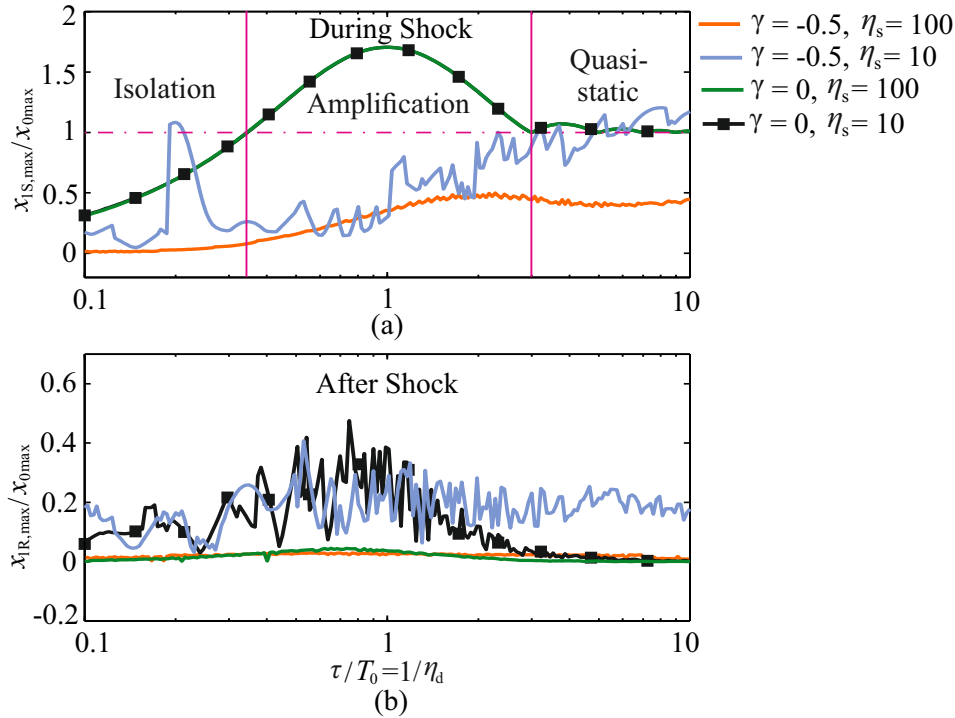


Figure 6.9.: Shock response of 4S for different natural periods  $T_0$  with respect to  $\eta_d$ .

Fig. 6.9 shows the performance of 4S for different dimensionless natural periods  $\tau/T_0 = 1/\eta_d$ . Without potential energy pre-storage,  $\gamma = 0$ , 4S owns the same shock isolation frequency region, although different dimensionless sampling frequencies,  $\eta_s$ , are applied, denoted by red and orange lines. On the contrary, only if a small quantity of potential energy pre-storage is used, 4S has a large isolation frequency region regardless of different dimensionless sampling frequencies, shown by blue and orange lines. A larger dimensionless sampling frequency enables a lower stiffness switching decision



error. Consequently, a much smoother shock response spectra and a lower residual vibration response can be obtained as shown in Fig. 6.9(b).

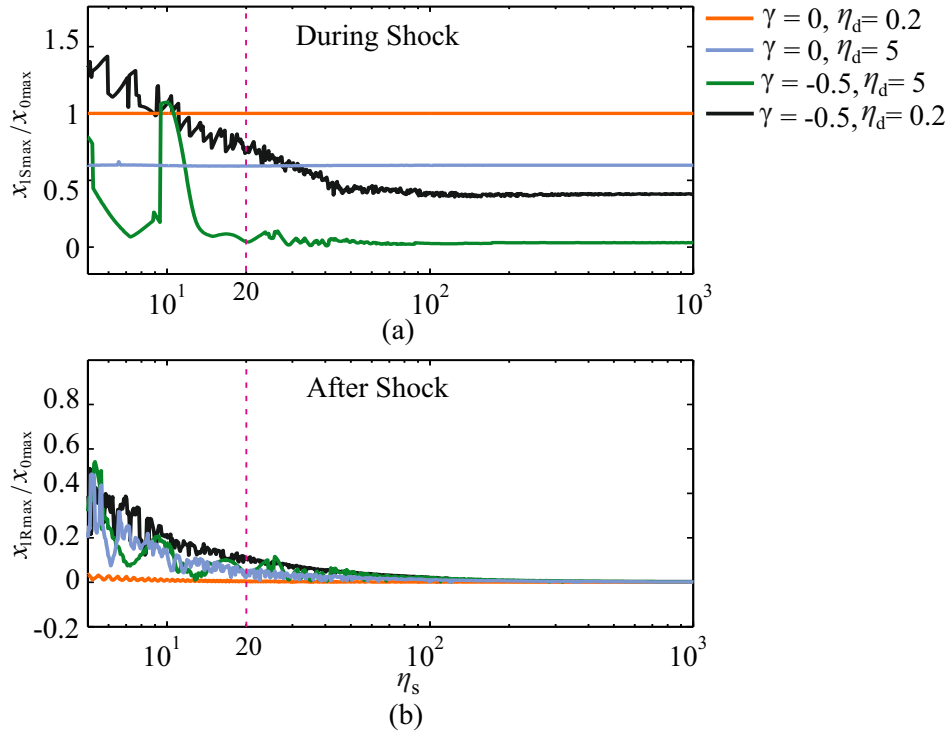


Figure 6.10.: Shock response of 4S for different dimensionless sampling frequencies  $\eta_s$ .

Fig. 6.10 shows the performance of 4S under different dimensionless sampling frequencies  $\eta_s$ . From Fig. 6.10(a), if potential energy pre-storage is provided,  $\gamma \neq 0$ , denoted by black and orange lines, a higher sampling frequency can lead to a smoother shock response spectra. If not, orange and blue lines, there exists almost no effects of sampling frequency on the performance. Of course, a variation from a subcritical excitation  $\eta_d = 0.2$  (orange) to a supercritical excitation  $\eta_d = 5$  (blue), meaning the stiffness decrease of 4S, realizes a lower shock response. Fig. 6.10(b) shows whether 4S owns potential energy pre-storage or not,  $\frac{x_{1R,max}}{\hat{x}_0}$  would be clearly influenced by the dimensionless sampling frequency of 4S. A higher dimensionless sampling frequency enables a lower residual vibration response. In fact, only if  $\eta_s \geq 20$  marked by pink dotted line in Fig. 6.10, 4S outperforms its counterparts by shock isolation performance as shown in Fig. 6.4 and Fig. 6.5.

Figure 6.11 depicts the effect of potential energy pre-storage on the performance. Before discussing the plots, it is revisited that a decreasing dimensionless sampling frequency,  $\eta_s$ , would results in an increasing stiffness switching decision error according to Eq. (5.23) and Fig. 2.7. Finally this will affect the system response strongly. Fig. 6.11(a) shows that at a sufficient high dimensionless sampling frequency, here  $\eta_s = 100$ , an increase in potential energy pre-storage improves isolation behavior until potential energy over pre-storage makes a shock amplification happen under both subcritical and supercritical excitation,  $\eta_d = 0.2$  and  $\eta_d = 5$ . For a lower dimensionless sampling frequency, here  $\eta_s = 10$ , an increase in  $|\gamma|$  deteriorates the isolation performance,  $\frac{x_{1S,max}}{\hat{x}_0}$ . Fig. 6.11(b) obviously shows that with a sufficient high dimensionless

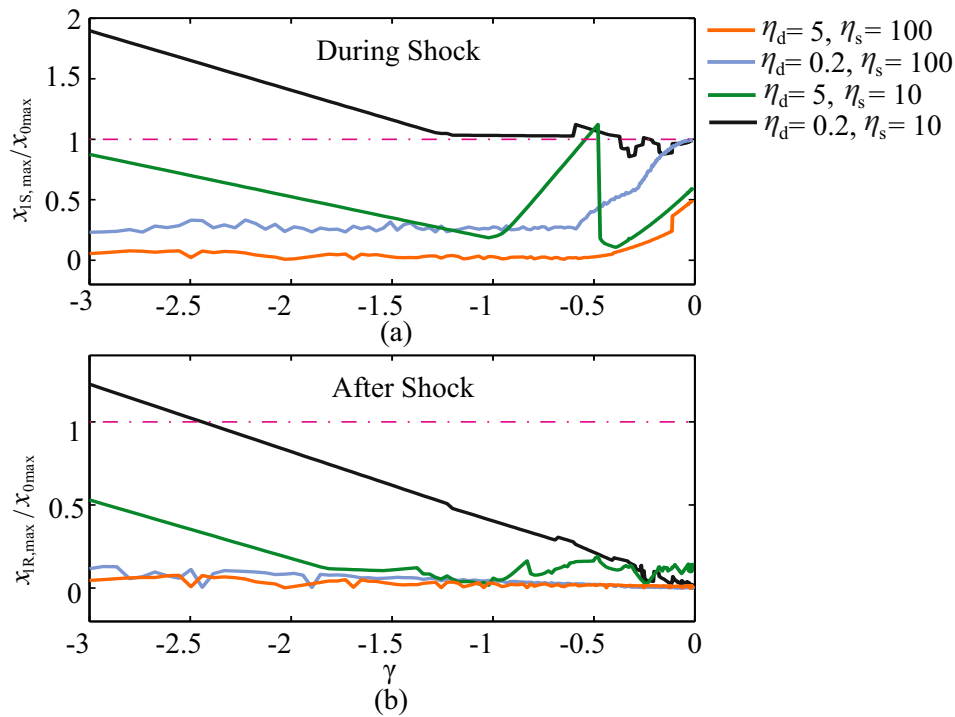


Figure 6.11.: Shock response of 4S for different potential energy pre-storage  $\gamma$ .

sampling frequency, the residual vibration suppression performance can be guaranteed, even at a high potential energy pre-storage. In a word, the dimensionless sampling frequency shall be over a threshold value and a reasonable amount of potential energy pre-storage should be considered before 4S is taken into practice.

At present, vibration isolation or shock isolation under a base excitation has not yet been experimentally considered. This will be further investigated in future.

---

# Summary and Future Work

---

An investigation of a novel semi-active vibration control strategy with Serial-Stiffness-Switch-System (4S) based on vibration energy harvesting has been presented in this thesis. This chapter gives overall conclusions of the investigation and puts forward recommendations of future work.

### 7.1. Summary

Vibration control is a classical theme and has been widely studied. Passive, active, semi-active and hybrid vibration control systems have appeared in the past decades. In these systems, system stiffness plays an important role on the system response such as settling time and working frequency ranges of the system. So, variable stiffness vibration control systems are of high interest. Variable stiffness devices and variable stiffness switching laws are reviewed. In most of the above mentioned variable stiffness systems, during a vibration reduction process there still exist unavoidable time instants, where elastic elements release potential energy, and drive a payload again. This is an intrinsic property of the elastic element and results in an oscillation in the system to some extent. In order to further reduce this adverse effect of the elastic element on vibration control, a novel semi-active vibration control with a Serial-Stiffness-Switch-System (4S) has been proposed in this thesis.

Firstly, 4S in open loop control under a harmonic disturbance is analyzed. The switching system oscillates based on the superposition of free, forced disturbance and chattering response and no vibration reduction occurs. An equivalent stiffness and natural frequency are mathematically derived and numerically validated through spectrum analysis. In order to achieve vibration reduction, a velocity zero-crossing switching law is introduced. It has been numerically proven that this switching law allows 4S

to harvest vibration energy and temporarily store in two springs, one of which is compressed and the other elongated. As a result, 4S can work as an actuator to react against an external disturbance and outperforms its passive counterparts. However, this happens at the cost of a high sampling frequency.

Following is dynamics analysis for 4S in closed loop control. The steady state response is analytically solved based on the decomposition of process force. Accordingly, vibration energy harvesting limitation is theoretically given and numerically validated.

This vibration control strategy has been also experimentally validated with a rotational test rig. This test rig has an easy achievement for a required low natural frequency and a low settling time actuator. Two ring-arranged electromagnet-plates and a armature-shaft structure works as two mechanical switches. Validation of the velocity zero-crossing switching law using the test rig gives good results. 4S is able to harvest vibration energy and achieve vibration reduction under a harmonic disturbance.

In order to improve system response, a new switching law is further proposed by means of phase plane. This switching law is also experimentally validated under a nonzero initial velocity and a harmonic disturbance. The results show that new switching law enables a lower settling time and a better positioning performance of 4S.

Apart from a force disturbance acting on a payload, a harmonic base and a shock disturbance are also considered. Compared to its counterparts, a passive or a semi-active switching system, 4S with a potential energy pre-storage shows a perfect shock isolation performance by the maximal displacement response reduction during shock, residual vibration suppression after shock, and an obvious increase of shock isolation regions.

## 7.2. Future Work

This thesis has given an insight into the use of a novel semi-active vibration control based on vibration energy harvesting. However, there are some aspects found during the investigation that might be worthy of further study as mentioned below.

- For the sake of simplicity, a switching delay occurring between two springs, is not considered in model. The switching delay causes two springs to be simultaneously open and then some potential energy would be released. This will affect system response. For an experimental model, a friction-based switching is also neglected. These two aspects should be further studied.
- A position PID feedback controlled switching law is put forward, but not deeply studied. How PID coefficients affect vibration energy harvesting and vibration reduction performance should be further investigated.
- Shock isolation has been numerically investigated but not experimentally validated. An experimental test rig suffering a shock input should be developed.

---

## Bibliography

---

- [1] David A. Bies and Colin H. Hansen. *Engineering Noise Control: Theory and Practice*. Taylor & Francis Group, 3rd edition, 2003.
- [2] Daniel J. Inman. *Engineering Vibration*. Prentice-Hall International, Inc., international edition, 1994.
- [3] M. R. Jolly and M. A. Norris. Passive, adaptive and active tuned vibration absorbers — a survey. *Journal of Vibration and Acoustics: Transactions of the ASME*, 117:234–242, 1995.
- [4] G. Hima Bindu and A. Siva kumar. A review on the performance of a vibration absorber in an active suspension system. *International Journal of Engineering Technology and Sciences*, 2:18–24, 2014.
- [5] Tarek Edrees Saaed, George Nikolakopoulos, Jan Erik Jonasson, and Hans Hedlund. A state-of-the-art review of structural control systems. *Journal of Vibration and Control*, 21(5):919–937, 2016.
- [6] Cyril M. Harris and Allan G. Piersol. *Harris Shock and Vibration Handbook*. McGRAW-HILL, 5th edition, 2002.
- [7] Yuyou Liu. *Semi-active Damping Control for Vibration Isolation of Base Disturbances*. PhD thesis, Institute of Sound and Vibration Research, University of Southampton, 2004.
- [8] R. A. Ibrahim. Recent advances in nonlinear passive vibration isolators. *Journal of Sound and Vibration*, 314:371–452, 2008.
- [9] G. W. Housner, L. A. Bergman, T. K. Caughey, and A. G. Chassiakos. Structural control: Past, present, and future. *Journal of Engineering Mechanics*, 123(9): 897–971, 1998.
- [10] S. G. Luca, F. Chira, and V. O. Rosca. Passive, active and semi-active control systems in civil engineering. *Bulletin of the Polytechnic Institute of Jassy: Construction. Architecture Section*, 3-4:23–31, 2005.
- [11] Andre Preumont. *Vibration Control of Active Structures*. Springer, 3rd edition, 2011.

- [12] Ugur Aridogan and Ipek Basdogan. A review of active vibration and noise suppression of plate-like structures with piezoelectric transducers. *Journal of Intelligent Material Systems and Structures*, 26:1455–1476, 2015.
- [13] Y. P. Xiong, J. T. Xing, W. G. Priceb, and X. P. Wang. Hybrid active and passive control of vibratory power flow in flexible isolation system. *Shock and Vibration*, 7(2000):139–148, 2000.
- [14] S. Mohammadi, S. Hatam, and A. Khodayari. Modeling of a hybrid semi-active/passive vibration control technique. *Journal of Vibration and Control*, 21(1):21–28, 2015.
- [15] I. U. Khan, D. W., and N. D. Sims. Improving the vibration suppression capabilities of a magneto-rheological damper using hybrid active and semi-active control. *Smart Structures and Systems*, 25:1–15, 2016.
- [16] X. Z. Zhang, X. Y. Wang, W. H. Li, and K Kostidis. Variable stiffness and damping mr isolator. In *11th Conference on Electrorheological Fluids and Magnetorheological Suspensions, Journal of Physics: Conference Series*, volume 149, pages 1–5, 2009.
- [17] Chuan Yang, Xiaowei Yuan, Jie Wu, and Besheng Yang. The research of passive vibration isolation system with broad frequency field. *Journal of Vibration and Control*, 19(9):1348–1356, 2011.
- [18] J. E. Bobrow. High performance damping with a semi-active spring. In *ASME Design Technical Conferences*, Sacramento, CA, 1997. paper DETC97/VIB-3826.
- [19] D. F. Ledezma-Ramirez, N. S. Ferguson, and M. J. Brennan. Shock isolation using an isolator with switchable stiffness. *Journal of Sound and Vibration*, 330: 868 – 882, 2011.
- [20] J. Q. Sun, M. R. Jolly, and M. A. Norris. Passive, adaptive and active tuned vibration absorbers: A survey. *Journal of Vibration and Acoustic*, 117:234–242, 1995.
- [21] M. L. C. de Laat, H. H. Perez Garza, J. L. Herder, and M. K. Ghatkesar. A review on in situ stiffness adjustment methods in mems. *Journal of Micromechanics and Microengineering*, 26:1–21, 2016.
- [22] Khalid Alblalaih, Peter Kinnell, Simon Lawes, Dorian Desgaches, and Richard Leach. Performance assessment of a new variable stiffness probing system for micro-cmms. *Sensors*, 16(492):1–18, 2016.
- [23] Sebastian Wolf, Giorgio Grioli, Oliver Eiberger, Werner Friedl, Markus Grebenstein, Hannes Hoppner, Etienne Burdet, Darwin G. Caldwell, and Raffaella Carloni. Variable stiffness actuators: Review on design and components. *IEEE/ASME Transactions on Mechatronics*, 21(5):2418–2430, 2016.
- [24] E. C. Lee, C. Y. Nian, and Y. S. Tang. Design of a dynamic vibration absorber against vibrations in turning operations. *Journal of Materials Processing Technology*, 108(3):278–285, 2017.

- [25] T. Kobori, M. Takahashi, T. Nasu, N. Niwa, and K. Ogasawara. Seismic response controlled structure with active variable stiffness system. *Earthquake Engineering and Structural Dynamics*, 22:25–41, 1993.
- [26] M. R. Tabeshpour, A. A. Golafshanib, and M. Monzavib. Seismic performance of a variable stiffness system. *Asian Journal of Civil Engineering (Building and Housing)*, 12(3):375–393, 2010.
- [27] J. Onoda, T. Endo, H. Tamaoki, and N. Watanabe. Vibration suppression by variable-stiffness members. *AIAA Journal*, 29(6):977 – 983, 1991.
- [28] C. Yong, D.G. Zimcik, V.K. Wickramasinghe, and F. Nitzsche. Development of the smart spring for active vibration control of helicopter blades. *Journal of Intelligent Material Systems and Structures*, 15:37 – 47, 2004.
- [29] I. Youn and A. Hac. Semi-active suspensions with adaptive capability. *Journal of Sound and Vibration*, 180:475–492, 1995.
- [30] H. P. Du, W. H. Li, and N. Zhang. Semi-active variable stiffness vibration control of vehicle seat suspension using an mr elastomer isolator. *Smart Materials and Structures*, 20:1 – 10, 2011.
- [31] M. Trikande, N. Karve, R. R, V. Jagirdar, and R. Vasudevan. Semi-active vibration control of an 8x8 armored wheeled platform. *Journal of Vibration and Control*, pages 1–20, 2016.
- [32] Michael F. Winthrop. *Engineering Tools for Variable Stiffness Vibration Suppression and Isolation*. PhD thesis, Air Force Institute of Technology, Ohio, USA, 2004.
- [33] Sanjay Sahasrabudhe and Satish Nagarajaiah. Effectiveness of variable stiffness systems in base-isolated bridges subjected to near-fault earthquakes: An experimental and analytical study. *Journal of Intelligent Material Systems and Structures*, 16:743–756, 2005.
- [34] N. W. Hagood and A. von Flotow. Damping of structural vibrations with piezoelectric materials and passive electrical networks. *Journal of Sound and Vibration*, 146(2):243–268, 1991.
- [35] L. R. Corr and W. W. Clark. Similarities between variable stiffness springs and piezoceramic switching shunts. *AIAA Journal*, 44(11):2797–2800, 2006.
- [36] G. Lesieutre. Vibration damping and control using shunted piezoelectric materials. *Shock and Vibration Digest*, 30(3):187–195, 1998.
- [37] C. Richard, D. Guyomar, D. Audigier, and G. Ching. Semi-passive damping using continuous switching of piezoelectric devices. *SPIE Conference on Passive Damping and Isolation*, 3672:104–111, 1999.
- [38] K. A. Cunefare. State-switched absorber for vibration control of point-excited beams. *Journal of Intelligent Material Systems and Structures*, 13:97–105, 2002.
- [39] W.W. Clark. Vibration control with state-switched piezoelectric materials. *Journal of Intelligent Material Systems and Structures*, 11:263–271, 2000.

- [40] Ismail Ladipo, Asan G.A. Muthalif, Alif Rozaima, and Ahmad Asyraf. Design and development of an active mass damper for broadband vibration control. In *IEEE: 4th International Conference on Mechatronics (ICOM)*, pages 1–4, 2011.
- [41] V. Balamurugan and S. Narayanan. Finite element formulation and active vibration control study on beams using smart constrained layer damping(sclD) treatment. *Journal of Sound and Vibration*, 249(2):227–250, 2002.
- [42] Feng-Ming Li, Kikuo Kishimoto, Yue-Sheng Wang, Zhao-Bo Chen, and Wen-Hu Huang. Vibration control of beams with active constrained layer damping. *Smart Structures and Systems*, 17:1–10, 2008.
- [43] A. Baz and J. Ro. Vibration control of plates with active constrained layer damping. *Smart Materials and Structures*, 5:272–280, 1995.
- [44] C. Liang and C. A. Rogers. Design of shape memory alloy springs with applications in vibration control. *Journal of Intelligent Material Systems and Structures*, 8:314–322, 1997.
- [45] E. Rustighi, M. J. Brennan, and B. R. Mace. A shape memory alloy adaptive tuned vibration absorber: design and implementation. *Smart Materials and Structures*, 14:19–28, 2005.
- [46] Jaakko Heinonen, Ismo Vessonen, Paul Klinge, and Tomi Lindroos. Semi-active vibration control based on shape memory alloy actuators — analysis experimental testing. *Journal of Structural Mechanics*, 40(1):23–28, 2007.
- [47] K. Williams, G. Chiu, and R. Bernhard. Adaptive-passive absorbers using shape memory alloys. *Journal of Sound and Vibration*, 249(5):835–848, 2002.
- [48] Chun-Ying Lee, Chien-Chang Chen, Tze-Hung Yang, and Chih-Jer Lin. Structural vibration control using a tunable hybrid shape memory material vibration absorber. *Journal of Intelligent Material Systems and Structures*, 23(15):1725–1734, 2012.
- [49] Chun-Ying Lee and Chung-An Pai. Design and implementation of tunable multi-degree-of-freedom vibration absorber made of hybrid shape memory helical springs. *Journal of Intelligent Material Systems and Structures*, 27(8):1047–1060, 2016.
- [50] J. D. Carlson and M. R. Jolly. Mr fluid, foam and elastomer devices. *Mechanics*, 10(5):55–69, 2000.
- [51] Yancheng Li, Jianchun Li, Weihua Li, and Haiping Du. A state-of-the-art review on magnetorheological elastomer devices. *Smart Materials and Structures*, 23: 1–24, 2014.
- [52] Huaxia Deng, Xinglong Gong, and Lianhua Wang. Development of an adaptive tuned vibration absorber with magnetorheological elastomer. *Smart Materials and Structures*, 15:111–116, 2006.
- [53] H. X. Deng and X. L. Gong. Adaptive tuned vibration absorber based on magnetorheological elastomer. *Journal of Intelligent Material Systems and Structures*, 18:1205–1210, 2007.



- [54] Shuaishuai Sun, Huaxia Deng, Jian Yang, Weihua Li, Haiping Du, Gursel Alici, and Masami Nakano. An adaptive tuned vibration absorber based on multilayered mr elastomers. *Smart Materials and Structures*, 24:1–14, 2015.
- [55] G. J. Liao, X. L. Gong, S. H. Xuan, C. J. Kang, and L. H. Zong. Development of a real-time tunable stiffness and damping vibration isolator based on magnetorheological elastomer. *Journal of Intelligent Material Systems and Structures*, 23(1):25–33, 2012.
- [56] Yancheng Li, Jianchun Li, Tongfei Tian, and Weihua Li. A highly adjustable magnetorheological elastomer base isolator for applications of real-time adaptive control. *Smart Structures and Systems*, 22:1–18, 2013.
- [57] Weihua Li, Xianzhou Zhang, and Haiping Du. Development and simulation evaluation of a magnetorheological elastomer isolator for seat vibration control. *Journal of Intelligent Material Systems and Structures*, 23(9):1041–1048, 2012.
- [58] Mingming Li, Jiheng Li, Xiaoqian Bao, Yangyang Liu, Jiquan Wang, Yalong Zhao, and Xuexu Gao. Variable stiffness fe82ga13.5al4.5 spring based on magnetoelastic effect. *Applied Physics Letters*, 110:1–4, 2017.
- [59] J. J. Scheidler, V. M. Asnani, and M. J. Dapino. Dynamically tuned magnetostrictive spring with electrically controlled stiffness. *Smart Materials and Structures*, 25:1 – 10, 2016.
- [60] G. P. McKnight and W. Barvosa-Carter. Variable stiffness structure. US 7550189 B1, 2009.
- [61] Y. Choi, A.F. Sprecher, and H. Conrad. Vibration characteristics of a composite beam containing an electrorheological fluid. *Journal of Intelligent Material Systems and Structures*, 1:91 – 104, 1990.
- [62] Vasudevan Rajamohan, Ramin Sedaghati, and Subhash Rakheja. Vibration analysis of a multi-layer beam containing magnetorheological fluid. *Smart Structures and Systems*, 1:1–12, 2009.
- [63] Farhan Gandhi and Sang-Guk Kang. Beams with controllable flexural stiffness. *Smart Structures and Systems*, 16:1179–1184, 2007.
- [64] Gabriel Murray and Farhan Gandhi. Multi-layered controllable stiffness beams for morphing: energy, actuation force, and material strain considerations. *Smart Structures and Systems*, 1:1–11, 2009.
- [65] P. I. Walsh and J. S. Lamancusa. A variable stiffness vibration absorber for minimization of transient vibration. *Journal of Sound and Vibration*, 158(2): 195–211, 1992.
- [66] P. Bonello an M. J. Brennan and S. J. Elliott. The design of an adaptive tuned vibration absorber with a variable shape stiffness element. Report, Institute of Sound and Vibration Research, University of Southampton, 2004.
- [67] M. J. Brennan. Some recent developments in adaptive tuned vibration absorbers/neutralisers. *Shock and Vibrations*, 13:531–543, 2006.

- [68] Philip Bonello. *Adaptive Tuned Vibration Absorbers: Design Principles, Concepts and Physical Implementation*. InTech, 2011.
- [69] Simon Hill, Scott Snyder, and Ben Cazzolato. An adaptive vibration absorber. In *Acoustics 2002 — Innovation in Acoustics and Vibration, Annual Conference of the Australian Acoustical Society*, 12 2002.
- [70] P. Bonello and K. H. Groves. Vibration control using a beam-like adaptive tuned vibration absorber with an actuator-incorporated mass element. *Journal of Mechanical Engineering Science*, 223:1555–1567, 2009.
- [71] Reza Mirsanei, Aidin Hajikhani, Behzad Peykari, and Jahanbakhsh Hamedi. Developing a new design for adaptive tuned dynamic vibration absorber (atdva) based on smart slider-crank mechanism to control of undesirable vibrations. *International Journal of Mechanical Engineering and Mechatronics*, 1(1):80–87, 2012.
- [72] Zhenbang Xu, Xinglong Gong, and Xianmin Chen. Development of a mechanical semi-active vibration absorber. *Advances in Vibration Engineering*, 10(3):229–238, 2011.
- [73] Satish Nagarajaiah. Structural vibration damper with continuously variable stiffness. US 6098969, 2000.
- [74] Nadathur Varadarajan, Satish Nagarajaiah, and M.ASCE. Wind response control of building with variable stiffness tuned mass damper using empirical mode decomposition hilbert transform. *Journal of Engineering Mechanics*, 130(4):451–458, 2004.
- [75] Satish Nagarajaiah and Sanjay Sahasrabudhe. Seismic response control of smart sliding isolated buildings using variable stiffness systems: an experimental and numerical study. *Earthquake Engineering and Structural Dynamics*, 35:177–197, 2006.
- [76] Satish Nagarajaiah, M. ASCE, and E. Sonmez. Structures with semiactive variable stiffness single/multiple tuned mass dampers. *Journal of Structural Engineering*, 133(1):67–77, 2007.
- [77] Amir Fateh, Farzad Hejazi, Mohd Saleh Jaafar, and Azlan Bin Adnan b Izian Abd. Karim. Design of a variable stiffness bracing system: Mathematical modeling, fabrication, and dynamic analysis. *Soil Dynamics and Earthquake Engineering*, pages 87–101, 2016.
- [78] K. Nagaya, A. Kurusu, S. Ikai, and Y. Shi. Vibration control of a structure by using a tunable absorber and an optimal vibration absorber under auto-tuning control. *Journal of Sound and Vibration*, 228(4):773–792, 1999.
- [79] M. H. Rafieipour, A. K. Ghorbani-Tanha, M. Rahimian, , and R. Mohammadi-Ghazi. A novel semi-active tmd with folding variable stiffness spring. *Earthquake Engineering and Engineering Vibration*, 13:509–518, 2014.
- [80] James A. Aardema and Macomb Mich. Variable stiffness spring suspension. US 4832321, 1989.

- [81] Arun Ramaratnam and Nader Jalili. A switched stiffness approach for structural vibration control: theory and real-time implementation. *Journal of Sound and Vibration*, 291:258–274, 2006.
- [82] Toshihiro Irie, Kiyoshi Shingu, Keita Kitamura, and Yoshihiro Takagi. Response control of variable stiffness structure using electromagnetic clutch. *Journal of Advanced Computational Intelligence and Intelligent Informatics*, 7(2):101–107, 2003.
- [83] Toshihiro Irie and Kiyoshi Shingu. Vibration control of variable rigidity frame structure by magnetic clutch. *Journal of Computational Science and Technology*, 2(3):393–400, 2008.
- [84] Y. Liu, H. Mathsuhsa, H. Utsuno, and J.G. Park. Variable damping and stiffness vibration control with magnetorheological fluid dampers for two degree-of-freedom system. *JSME International Journal Series C*, 49:156 – 162, 2006.
- [85] Yanqing Liu, Hiroshi Matsuhisa, and Hideo Utsuno. Semi-active vibration isolation system with variable stiffness and damping control. *Journal of Sound and Vibration*, 313:16–28, 2008.
- [86] S. S. Sun, X. Tang, W. H. Li, and H. P. Du. Advanced vehicle suspension with variable stiffness and damping mr damper. In *IEEE: International Conference on Mechatronics*, pages 444–448, 2017.
- [87] C. Greiner-Petter, A. S. Tan, and T. Sattel. A semi-active magnetorheological fluid mechanism with variable stiffness and damping. *Smart Materials and Structures*, 23:1–10, 2014.
- [88] Martin Silge, Christoph Greiner-Petter, and Thomas Sattel. A concept for vehicle suspension systems with variable mechanical impedance based on magnetoand electrorheological fluid actuators. In *Actuator 2014, MESSE BREMEN*, pages 1–4, 2014.
- [89] L. M. Jugulkar, S. Singh, and S. M. Sawant. Analysis of suspension with variable stiffness and variable damping force for automotive applications. *Advances in Mechanical Engineering*, 8(5):1–19, 2016.
- [90] T. Kobori and S. Kamagata. Active variable stiffness control: active seismic response control. *Proceedings U.S.-Italy-Japan Workshop/Symposium on Structural Control and Intelligent Systems*, pages 140–153, 1992.
- [91] Khiem Thai, Faryar Jabbari, and James E. Bobrow. Structural control via semi-active and hybrid control. In *Proceedings of the American Control Conference*, pages 6–10, 1997.
- [92] James E. Bobrow, Faryar Jabbari, and Khiem Thai. A new approach to shock isolation and vibration suppression using a resettable actuator. *Transactions of the ASME*, 122:570–573, 2000.
- [93] J. Leavitt, F. Jabbari, and J. E. Bobrow. Optimal control and performance of variable stiffness devices for structural control. In *2005 American Control Conference*, pages 2499–2504, 2005.

- [94] John Leavitt, James E. Bobrow, and Faryar Jabbari. Design of a 20,000 pound variable stiffness actuator for structural vibration attenuation. *Shock and Vibration*, 15:687–696, 2008.
- [95] Jay Chung Chen. Response of large space structures with stiffness control. *Journal of Spacecraft*, 21:463–467, 1984.
- [96] J. L. Fanson, J. C. Chen, and T. K. Caughey. Response of large space structures with stiffness control. In *Proceedings of the Workshop on Identification and Control*, number 2, pages 351–364, 1985.
- [97] Ho-Kyeong Jeong, Jae-Hung Han, Se-Hyun Youn, and Juho Lee. Frequency tunable vibration and shock isolator using shape memory alloy wire actuator. *Journal of Intelligent Material Systems and Structures*, 25(7):908–919, 2014.
- [98] Ho-Kyeong Jeong, Juho Lee, Jae-Hung Han, and N. M. Wereley. Design of frequency-tunable mesh washer isolators using shape memory alloy actuators. *Journal of Intelligent Material Systems and Structures*, 27(9):1265–1280, 2016.
- [99] Mojtaba Azadi, Saeed Behzadipour, and Garry Faulkner. Antagonistic variable stiffness elements. *Mechanism and Machine Theory*, 44(9):1746–1758, 2009.
- [100] Mojtaba Azadi, Saeed Behzadipour, and Simon Guest. A new variable stiffness spring using a prestressed mechanism. In *Proceedings of the ASME 2010 International Design Engineering Technical Conferences and Computers and Information in Engineering Conference*, pages 1–7, 2010.
- [101] Mojtaba Azadi, Saeed Behzadipour, and Garry Faulkner. Performance analysis of a semi-active mount made by a new variable stiffness spring. *Journal of Sound and Vibration*, 330:2733–2746, 2011.
- [102] Yusuke Suzuki and Naoto Abe. Variable stiffness system for semi-active vibration control by frequency. In *SICE Annual Conference 2013*, pages 923–928, Nagoya University, Nagoya, Japan, 2013.
- [103] J. Onoda, T. Sano, and K. Kamiyama. Active, passive and semiactive vibration suppression by stiffness variation. *AIAA Journal*, 30(12):2922 – 2929, 1992.
- [104] Arun Ramaratnam, Nader Jalili, and Darren M. Dawson. Semi-active vibration control using piezoelectric-based switched stiffness. In *Proceeding of the 2004 American Control Conference*, pages 5461–5466, Boston, Massachusetts, 2004.
- [105] G. Leitmann and E. Reithmeier. Semi-active control of a vibrating system by means of electrorheological fluids. *Dynamics and Control*, 3:7 – 33, 1993.
- [106] G. Leitmann. Semiactive control for vibration attenuation. *Journal of Intelligent Material Systems and Structures*, 5:841 – 846, 1994.
- [107] J. N. Yang, Z. Li, and J. C. Wu. Control of seismic-excited building using active variable stiffness systems. In *Proceedings of the American Control Conference*, pages 1083–1088, 06 1994.
- [108] James E Bobrow, Faryar Jabbari, and Kiem Thai. An active truss element and control law for vibration suppression. *Smart Materials and Structures*, 4:264–269, 1995.

- [109] K. Thai, F. Jabbari, and J. E. Bobrow. Vibration suppression through parametric control: A general framework. In *Proceedings of 1995 IMECE (International Mechanical Engineering Congress and Exposition)*, San Francisco, CA, 1995. ASME.
- [110] K. Thai. *Parametric methods for vibration suppression*. PhD thesis, University of California, Irvine, 1997.
- [111] J. N. Yang, J.H. Kim, and A. K. Agrawal. Resetting semi-active stiffness damper for seismic response control. *Journal of Structure Engineering*, 126(12):1427–33, 2000.
- [112] J. N. Yang, J. Bobrow, F. Jabbari, J. Leavitt, C. P. Cheng, and P. Y. Lin. Full-scale experimental verification of resettable semi-active stiffness dampers. *Earthquake Engineering and Structure Dynamics*, 36:1255–1273, 2007.
- [113] D. Karnopp, M.J. Crossby, and R.A. Harwood. Vibration control using semi-active force generators. *ASME Journal of Engineering for Industry*, 96:619–626, 1974.
- [114] K. A. Cunefare, S. D. Rosa, N. Sadegh, and G. Larson. State-switched absorber for semi-active structural control. *Journal of Intelligent Material Systems and Structures*, 11:300–310, 2000.
- [115] Mark Horner Holdhusen. *The State-switched Absorber Used for Vibration Control of Continuous Systems*. PhD thesis, Georgia Institute of Technology, 02 2005.
- [116] Y. Liu, H. Matsuhisa, H. Utsuno, and J.G. Park. Vibration isolation by a variable stiffness and damping system. *JSME International Journal Series C*, 48:305 – 310, 2005.
- [117] S. Opie and W. Yim. Design and control of a real-time variable stiffness vibration isolator. In *IEEE/ASME International Conference on Advanced Intelligent Mechatronics*, pages 380–385, 2009.
- [118] L. R. Corr and W. W. Clark. Energy dissipation analysis of piezoceramic semi-active vibration control. *Journal of Intelligent Material Systems and Structures*, 12:729–736, 2002.
- [119] A. Badel, G. Sebald, D. Guyomar, M. Lallart, E. Lefeuvre, C. Richard, and J. Qiu. Piezoelectric vibration control by synchronized switching on adaptive voltage sources: towards wideband semi-active damping. *Journal of Acoustic Society American*, 119(5):2815–2825, 2006.
- [120] E. Lefeuvre, A. Badel, L. Petit, C. Richard, and D. Guyomar. Semi-passive piezoelectric structural damping by synchronized switching on voltage sources. *Journal of Intelligent Material Systems and Structures*, 17:653–660, 2006.
- [121] D. Guyomar and C. Richard, C. Gehin, and D. Audigier, editors. *Proceedings of the 12th IEEE International Symposium on Applications of Ferroelectrics*, volume 2, 2001.

- 
- [122] Lallart M, Lefeuvre E, Richard C, and Guyomar D. Self-powered circuit for broadband, multimodal piezoelectric vibration control. *Sensors Actuators A*, 143:377–382, 2008.
- [123] Yu-Yin Chen, Dejan Vasic, Francois Costa, Chih-Kung Lee, and Wen-Jong Wu. Self-powered semi-passive piezoelectric structural damping based on zero-velocity crossing detection. *Smart Materials and Structures*, 22:1–12, 2013.
- [124] Chaoqing Min, Martin Dahlman, and Thomas Sattel. A concept for semi-active vibration control with a serial-stiffness-switch system. *Journal of Sound and Vibration*, 405:234–250, 2017. doi: doi.org/10.1016/j.jsv.2017.06.007.
- [125] V. I. Utkin. Survey paper: Variable structure systems with sliding mode. *IEEE Transactions on Automatic Control*, 22(2):212–222, 1977.
- [126] J. Y. Hung, W. B. Gao, and J. C. Hung. Variable structure control: A survey. *IEEE Transactions on Industrial Electronics*, 40(1):2–22, 1993.
- [127] C. Harris and C. Crede. *Shock and Vibration Handbook, Vol 1: Basic Theory and Measurements*. New York: McGraw-Hill, 1996.
- [128] C. Harris and C. Crede. *Shock and Vibration Handbook, Vol 1: Basic Theory and Measurements*. New York: McGraw-Hill, 1996.
- [129] Vadim Utkin, Juergen Guldner, and Jingxin Shi. *Sliding Mode Control in Electro-Mechanical Systems*. CRC Press, Taylor & Francis Group, second edition, 2009.
- [130] B. Bandyopadhyay, S. Janardhanan, and S.K. Spurgeon. *Advances in Sliding Mode Control: Concept, Theory and Implementation*. Springer, 2013.
- [131] Raymond A. DeCarlo, S.H. Zak, and Sergey V. Drakunov. *Control System Advanced Methods*. CRC Press, Taylor & Francis Group, 2011.

---

## Vibration Energy Limit Analysis

---

### A.1. Solution for Integration Coefficients

The high frequency term  $x_{11Fp,chat,p}(t)$  will be split into two time spans as expressed in

$$x_{11Fp,chat,p}(t) = K_1 \cos[\omega_0(t - t_{sw,2j})] + K_2 \sin[\omega_0(t - t_{sw,2j})] + u_{2s} , \quad (A.1)$$

$$x_{12Fp,chat,p}(t) = K_3 \cos[\omega_0(t - t_{sw,2j+1})] + K_4 \sin[\omega_0(t - t_{sw,2j+1})] + u_{1s} , \quad (A.2)$$

where  $u_{1s} = -u_{2s}$  and the transition conditions for the switching between two springs are given by

$$x_{11Fp,chat,p}(t_{sw,2j}) = x_{12Fp,chat,p}(t_{sw,2j+2}) , \quad x_{11Fp,chat,p}(t_{sw,2j+1}) = x_{12Fp,chat,p}(t_{sw,2j+1}) , \quad (A.3)$$

and

$$\dot{x}_{11Fp,chat,p}(t_{sw,2j}) = \dot{x}_{12Fp,chat,p}(t_{sw,2j+2}) , \quad \dot{x}_{11Fp,chat,p}(t_{sw,2j+1}) = \dot{x}_{12Fp,chat,p}(t_{sw,2j+1}) . \quad (A.4)$$

As a result, four equations are obtained as

$$K_1 \cos(\omega_0 T_s) + K_2 \sin(\omega_0 T_s) + u_{2s} = K_3 + u_{1s} , \quad (A.5)$$

$$K_1 + u_{2s} = K_3 \cos(\omega_0 T_s) + K_4 \sin(\omega_0 T_s) + u_{1s} , \quad (A.6)$$

$$-K_1 \sin(\omega_0 T_s) + K_2 \cos(\omega_0 T_s) = K_4 , \quad (A.7)$$

$$-K_3 \sin(\omega_0 T_s) + K_4 \cos(\omega_0 T_s) = K_2 , \quad (A.8)$$

Solving the above equation groups gives the integration coefficients  $K_1, K_2, K_3, K_4$ .



---

## Setup Construction

---

### B.1. Diameter and Thickness of Armature

Two designs for the armature are shown as shown in Fig. 4.4 and Fig. 4.4. Magnetic flux  $\Phi$  through the cross section and the inside of armature for two designs can be given by

$$\Phi = B \cdot ab = B \cdot 2(a + b) \cdot d_{1\min} , \quad (\text{B.1})$$

and

$$\Phi = B \cdot ab = B \cdot (a + 2b) \cdot d_{2\min} . \quad (\text{B.2})$$

So, the minimal thickness of armature  $d_{1\min}$  and  $d_{2\min}$  can be determined by

$$d_{1\min} \approx \frac{ab}{2(a + b)} , \quad d_{2\min} \approx \frac{ab}{a + 2b} , \quad (\text{B.3})$$

where  $a$  and  $b$  are the two sides of the working area of U-magnet. The volume of armature is given by

$$V_a = A_a d , \quad (\text{B.4})$$

where  $A_a$  is the area of armature,  $A_a = \pi(R^2 - r^2)$  and  $d$  is the thickness. The area of armature for Fig. 4.4 is given by

$$A_{a1} = \pi(X^2 + 2Xr) + \pi(a^2 + 2a(X + r)) , \quad (\text{B.5})$$

and for Fig. 4.5,

$$A_{a2} = \pi(X^2 + 2Xr) , \quad (\text{B.6})$$

where  $X = 2b + c$ . So the volume of the armature  $V_{a1}$  for Fig. 4.4 is given by

$$V_{a1} = A_{a1} d_{1\min} , \quad (\text{B.7})$$

and the volume of the armature  $V_{a2}$  for Fig. 4.5 is

$$V_{a2} = A_{a2}d_{2\min} . \quad (\text{B.8})$$

The ratio of  $V_{a1}$  to  $V_{a2}$  is written by

$$\frac{V_{a1}}{V_{a2}} = \frac{X^2 + 2Xr + 2a(X + r) + a^2}{X^2 + 2Xr} \cdot \frac{a + 2b}{2(a + b)} . \quad (\text{B.9})$$

The geometry parameters of U-magnet cores are informed from the production company Wasserner and the outside parameter of a spiral spring,  $V_{a1}/V_{a2} = 1.275 > 1$ , so the second design is more reasonable.

## B.2. Switching Current Measurement of Mechanical Switch

Fig. B.1 shows the voltage and current applied to the used two electromagnets. Due to a chattering voltage signal produced by a switching power electronics, a mean voltage is required to improve a readability as denoted by magenta and cyan lines,  $U_{em1}$  and  $U_{em2}$ . At beginning,  $i_{em1}$  (red line) increases from 0 to the maximum, a high positive voltage signal is needed. After  $i_{em1}$  reaches the maximum, a medium mean voltage is applied. When electromagnet 2 is powered off, the switching power electronics outputs a low level signal (-1), and a correspondingly negative voltage will be applied to the electromagnet. Consequently, the current  $i_{em2}$  (blue line) quickly decreases to 0. Meanwhile, the switching power electronics also outputs a zero level signal and the applied voltage remains zero as well. A reverse switching state of the mechanical switch is shown in Fig. B.1(b).

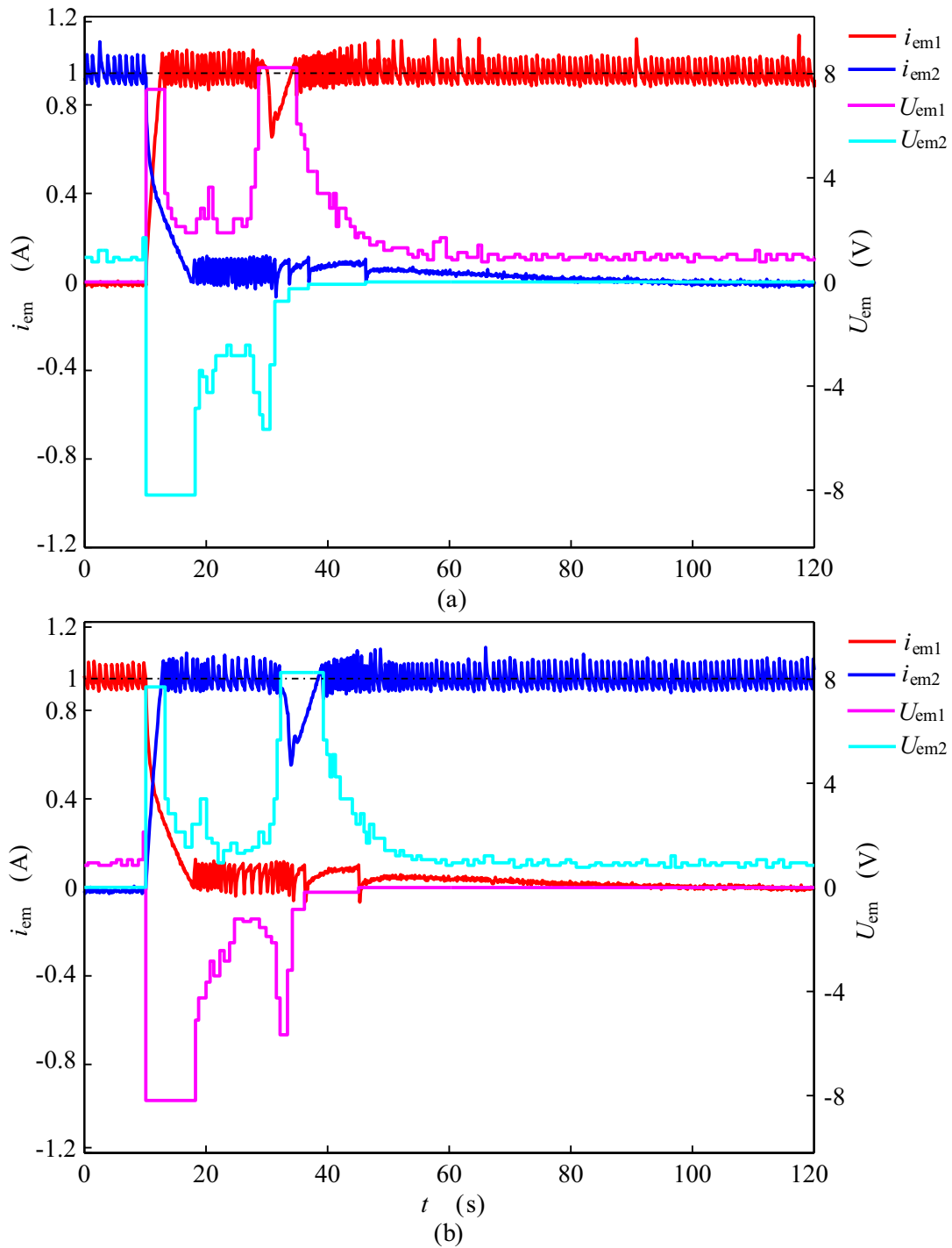


Figure B.1.: Switching current measurement of the used two electromagnets. (a) On state of electromagnet 1 and off state of electromagnet 2; (b) On state of electromagnet 2 and off state of electromagnet 1.

---

## Sliding Mode Control

---

### C.1. Theory Basis

Sliding mode control, a particular class of variable structure system control firstly introduced by Emelyanov in 1970 [129], has now become a mature technique for the design of robust controllers widely applied in the engineering areas including nonlinear, uncertain and time-delayed systems [130].

In fact, sliding mode control is a high frequency switching feedback control. This switching control law is able to move the system state trajectory onto a demand surface in the state space. Afterwards, the state trajectory will be always maintained on this surface. If the state trajectory is above or below the surface, the switching feedback control will force it to fall or rise and finally, the system state trajectory can only slides along this surface for all subsequent time instants. The surface is called sliding mode surface, defining the rule for proper switching and restricting the system state trajectory. The resulting motion of the state trajectory, passing through sliding surface from above to below or vice versa, is named sliding mode motion [131]. This can be interpreted as follows. Provided that a general control system is given by

$$\dot{\mathbf{x}} = f(\mathbf{x}, u, t), \quad \mathbf{x} \in \mathbf{R}^n, \quad u \in R, \quad t \in R^+, \quad (\text{C.1})$$

where for the sack of simplicity a single input control  $u$  is taken into consideration and it is the function of state variables  $\mathbf{x}$ , namely,  $u(\mathbf{x})$ . There exists a prespecified sliding surface  $s$ ,  $s = s(\mathbf{x}) = s(x_1, x_2, \dots, x_m) = 0$ ,  $m \leq n$  and sliding mode controller is given by

$$u(\mathbf{x}) = \begin{cases} u^+(\mathbf{x}) & \text{if } s(\mathbf{x}) \geq 0 \\ u^-(\mathbf{x}) & \text{if } s(\mathbf{x}) < 0 \end{cases} . \quad (\text{C.2})$$

Based on the control strategy in Eq. (C.2) the system state trajectory can not only reach the desired surface  $s = 0$  but also always stay on it. This leads to the following necessary condition,

$$\lim_{s \rightarrow 0^+} \dot{s} \leq 0, \quad \wedge \quad \lim_{s \rightarrow 0^-} \dot{s} \geq 0, \quad (\text{C.3})$$

or a compact formulation

$$\lim_{s \rightarrow 0} s\dot{s} \leq 0. \quad (\text{C.4})$$

In order to understand the principle well, it is also graphically illustrated in Fig. C.1. The sliding mode surface  $s = 0$  divides the state space into two parts,  $s > 0$  and  $s < 0$ . The curve between the point  $(\mathbf{x}_0, t_0)$  and  $(\mathbf{x}_1, t_1)$  shows that the state trajectory reaches the state space point  $(\mathbf{x}_1, t_1)$  on the prespecified sliding surface  $s = 0$  from the

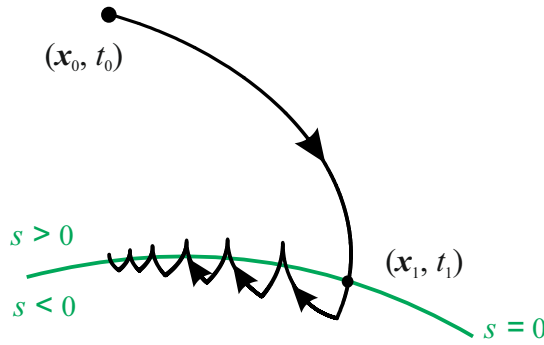


Figure C.1.: State trajectory representation for sliding mode control

initial state  $(\mathbf{x}_0, t_0)$  under a proper switching law according to Eq. (C.2). In sliding mode motion area denoted by saw-tooth-alike lines, if  $s > 0$ , the state trajectory is above the sliding surface, the feedback control  $u^+$  results in a negative changing rate  $\dot{s}$  as expressed in Eq. (C.3), namely, forces the state trajectory to drop until below the sliding surface. If  $s < 0$ , the state trajectory will be driven by the control  $u^-$  above the sliding surface.

So a sliding mode control design consists of two steps. The first step is to decide a sliding mode surface  $s$ , so that the system state trajectory limited to the surface has the wished dynamics. The second step is to choose a switched control  $u$ , which will move the system state to the sliding surface and maintain it on the surface for the subsequent time instants.

# Erklärung

Ich versichere, dass ich die vorliegende Arbeit ohne unzulässige Hilfe Dritter und ohne Benutzung anderer als der angegebenen Hilfsmittel angefertigt habe. Die aus anderen Quellen direkt oder indirekt übernommenen Daten und Konzepte sind unter Angabe der Quelle gekennzeichnet.

Bei der Auswahl und Auswertung folgenden Materials haben mir die nachstehend aufgeführten Personen in der jeweils beschriebenen Weise unentgeltlich geholfen:

1. Herr Martin Dahlmann hat fachlich und inhaltlich mitgearbeitet zu den Veröffentlichungen 1 und 2.

Weitere Personen waren an der inhaltlich-materiellen Erstellung der vorliegenden Arbeit nicht beteiligt. Insbesondere habe ich hierfür nicht die entgeltliche Hilfe von Vermittlungs- bzw. Beratungsdiensten (Promotionsberater oder anderer Personen) in Anspruch genommen. Niemand hat von mir unmittelbar oder mittelbar geldwerte Leistungen für Arbeiten erhalten, die im Zusammenhang mit dem Inhalt der vorgelegten Dissertation stehen.

Die Arbeit wurde bisher weder im In- noch im Ausland in gleicher oder ähnlicher Form einer Prüfungsbehörde vorgelegt.

Ich bin darauf hingewiesen worden, dass die Unrichtigkeit der vorstehenden Erklärung als Täuschungsversuch bewertet wird und gemäß § 7 Abs. 10 der Promotionsordnung den Abbruch des Promotionsverfahrens zur Folge hat.

Ilmenau, den September 18, 2018